EFFECTS OF DIELECTRIC RELAXATION ON DIRECTOR DYNAMICS IN UNIAXIAL NEMATIC LIQUID CRYSTALS

A dissertation submitted to Kent State University in partial fulfillment of the requirements for the Degree of Doctor of Philosophy

By

Mingxia Gu

May 2009

Dissertation written by

Mingxia Gu

B.S., Beijing Normal University, 2001

Ph.D. Kent State University, 2009

Approved by

Oleg D. Lavrentovich, Chair, Doctoral Dissertation Committee

Sergij V. Shiyanovskii, Members, Doctoral Dissertation Committee

Philips J. Bos

Deng –Ke Yang

Samuel Sprunt

Accepted by

Oleg D. Lavrentovich, Director, Chemical Physics Interdisciplinary Program

John R.D. Stalvey, Dean, College of Arts and Sciences

TABLE OF CONTENTS

LIST OF FIGURES

ACKNOWLEDGMENTS

I am grateful to my advisor, Dr. Oleg D. Lavrentovich. His expertise and vision in science have always been the inspiration and motivation during my graduate research. I would not be able to complete this work without his support and guidance.

I want to thank my co-advisor, Dr. Sergij V. Shiyanovskii. His solid theoretical knowledge always enlightens the discussions which lead to many fruitful results.

I would also like to thank all other CPIP faculty members for teaching me the fascinating liquid crystal world. Special thanks go to LCI administrative staff for all their kindness and help.

I am indebted to all my colleagues and friends at LCI for the fruitful interactions during these years.

Finally I want to express my great gratitude to my parents, my beautiful wife, Yining Lin and her parents. Thank you for your love and for always being there for me. This work is dedicated to you all.

Chapter 1

INTRODUCTION

As the name suggests, liquid crystals (LCs) are a special class of materials. The main feature of a LC is a long-range orientational order of building units that might be individual molecules or their aggregates, and a complete or partial absence of positional order. As a result, the LC possesses properties intermediate between those featured by isotropic liquids and conventional solid crystals [1-3]. The LCs are comprised of anisometric molecules, typically rod-like or disk-like. The long-range orientational order in LCs might be of different types. The simplest is a uniaxial orientational order, pertinent to the so-called nematic LC (NLC). In the NLCs formed by rod-like molecules, their long axes arrange themselves predominantly parallel to each other. The direction of the preferred orientation is called the director. There is one spatial direction, specified by a unit vector called the director $\hat{\mathbf{n}}$, $\hat{\mathbf{n}}^2 = 1$. The uniaxial NLC is centrosymmetric: $\hat{\mathbf{n}}$ and $-\hat{\mathbf{n}}$ are indistinguishable and the director is simultaneously the optic axis of the material. The director describes only the preferred direction of the molecules, but it does not indicate the degree of orientational order of the mesophase. The order parameter, *S*, which is defined as the

second order of the distribution function of molecules in the Legendre polynomial series, provides a measure of the long range orientational order [3]

$$S = \frac{1}{2}\left\langle 3\cos^2\theta - 1 \right\rangle \qquad (1.1)$$

Where θ is the angle between the long axis of the molecule and the director, and the average is taken over the entire ensemble. For perfect crystals, $S = 1$ and $S = 0$ for isotropic phase, and for NLC.

Since the NLC is a medium with anisotropic physical properties, externally applied electromagnetic fields can reorient the director and thus alter the optical appearance of the sample. The prevailing mechanism of the LC-electric field coupling, that is at the heart of modern display applications, is dielectric anisotropy of the LC. The effect of field-induced director reorientation is known as Frederiks effect [3].

In the classic physics of liquid crystals, dielectric response is described as instantaneous: it is assumed that the electric displacement at the moment of time t is determined solely by the electric field at the very same moment *t*. However, the reorientation of polarization takes finite time to reach equilibrium, which is known as the dielectric relaxation. For many LC materials, this finite dielectric relaxation time is in the range of 0.01-1 ms, which is close to the currently achieved switching times (a few ms) of the NLC-based devices and which certainly exceeds the desired times of switching. Therefore, the assumption of "instantaneous" response is not valid anymore, i.e. the electric displacement depends not only on the current field but also the prehistory. To account for the finite rate of dielectric relaxation, a model of field-induced reorientation should explicitly take into account the frequency dependence of the components of the dielectric permittivities tensor [4].

The ultimate goal of this research is to develop better physical understanding of the time-dependent dielectric response of NLCs, when the switching time is short and thus the electric displacement depends not only on the present value of the electric field and the state of director, but also on their past values.

In this thesis, we develop a generalized model that accounts for processes of dielectric relaxation pertinent to both parallel and perpendicular components of dielectric permittivity [5]. This model allows us to extend the earlier description by Yin et al [4] of dielectric relaxation effects in the parallel component of permittivity and in a relatively limited class of "proper" dual frequency NLCs, to nearly all NLC systems, including cyanobiphenyls. Cyanobiphenyls are the most widely used nematic compounds in electro-optic research and applications; their dielectric relaxation time is in the range of nanoseconds. The proposed model was tested and confirmed experimentally by using NLC materials with different types and different characteristic times of dielectric relaxation. We also demonstrated a new physical effect associated with the finite rate of dielectric relaxation, namely, an existence of contribution to the dielectric torque that is linear in the current electric field and is thus sensitive to the polarity of the applied field [6]. We proposed various approaches to the optimization of the voltage pulse profiles to shorten the overall response time of the NLC electrooptical cell. Finally, we studied the dynamics of polar and nonpolar order parameters during the nematic-isotropic phase transition induced by an external electric field [7].

The content of this thesis is covered by the following publications:

1. "Fast switching optical modulator based on Dual Frequency Nematic Cell", Ye Yin, Mingxia Gu, Andrii B. Golovin, Sergij V. Shiyanovskii, Oleg D. Lavrentovich; Mol. Cryst. Liq. Cryst. **421**, 133 (2004).
2. "Directed vertical alignment liquid crystal display with fast switching", Mingxia Gu, Ivan I. Smalyukh, and Oleg D. Lavrentovich, Appl. Phys. Lett. **88**, 061110 (2006).
3. "Effects of dielectric relaxation on the director dynamics of uniaxial nematic liquid crystals", Mingxia Gu, Ye Yin, Sergij V. Shiyanovskii, and Oleg D. Lavrentovich, Phys. Rev. E **76**, 061702 (2007).
4. "Polarity-dependent dielectric torque in nematic liquid crystals", Mingxia Gu, Sergij V. Shiyanovskii, and Oleg D. Lavrentovich, Phys. Rev. Lett., **100**, 237801 (2008).
5. "Polar and non-polar orderings in the electrically induced isotropic-nematic phase transition", Mingxia Gu, Sergij V. Shiyanovskii, and Oleg D. Lavrentovich, Phys. Rev. E **78**, 040702(R) (2008).

1.1 Organization of this dissertation

In Chapter 1, we outline fundamental concepts of NLCs, providing a general background for our work. These topics include the director dynamics under external electric fields and the associated optics, dielectric relaxations in the NLCs and the isotropic-nematic phase transition induced by an external electric field.

In Chapter 2, we discuss how the director dynamics is affected by the dielectric relaxations in different NLCs. We present a general model that accounts for multiple processes of dielectric relaxation of both the parallel and perpendicular components of the dielectric tensor. We experimentally compare this new model with previously proposed ones (in which only one relaxation process was considered) and show that ours describes the NLC director dynamics more accurately. We also experimentally demonstrate for the first time that, in the NLCs with negative dielectric anisotropy, a larger torque was observed due to the larger value of $|\Delta\varepsilon|$ at high frequency due to dielectric relaxation; therefore this larger torque accelerates the director reorientation.

In Chapter 3, we demonstrate that the dielectric torque contains a part which is sensitive to the polarity of the present applied electric field. By properly choosing the duration and the polarity of the voltage pulse, one can construct a driving waveform which optimizes the dielectric torque to accelerate the director relaxation from the field-on state to the field-off state thus shortening the switch-off time.

In Chapter 4, we discuss how to design optimized voltage pulses that avoid detrimental dielectric relaxation effects; this optimization is based on the model presented in Chapter 2. This new scheme improves the switching efficiency: it increases the director reorientation rate in the desired direction.

In Chapter 5, we studied the dynamics of the electrically induced isotropic-nematic phase transition. In this study we show how both the polar and non-polar orderings develop during the electrically induced I-N phase transition.

In Chapter 6, we present our conclusions and outline potential future research subjects for the dielectrically dispersive NLCs.

1.2 Electrooptic phenomena in nematic liquid crystals

Nematic liquid crystals (NLCs) are characterized by a long-range orientational order, but there is no long-range positional order of the molecules. Figure 1.1 shows the classic sandwich type NLC cell, where the NLC is placed between two substrates, for two typical surface anchoring conditions: (a) planar orientation, with the director parallel to a particular axis in the plane of the substrates and (b) homeotropic orientation with the director perpendicular to the substrate; the substrates are separated by a distance d . The discussions below focus on these two types of orientations.

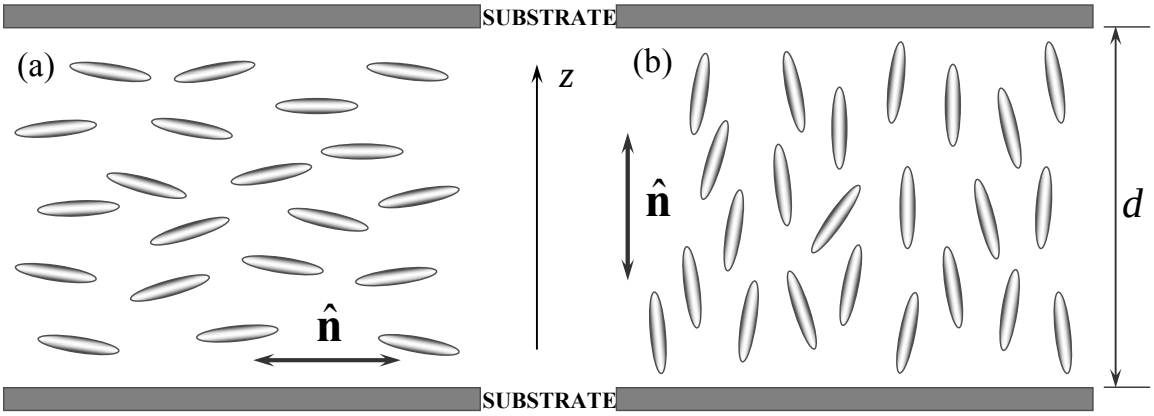

Figure 1.1. Cells filled with NLCs, (a) planar orientation; (b) homeotropic orientation. The z-axis is defined as normal to the substrate.

In the field free state, the NLC director orientation is determined by the minimization of the free energy density [2], which is described by the Oseen-Frank elastic free energy density:

$$f = \frac{1}{2}K_{11}\left(\nabla \cdot \hat{\mathbf{n}}\right)^2 + \frac{1}{2}K_{22}\left(\hat{\mathbf{n}} \cdot \nabla \times \hat{\mathbf{n}}\right)^2 + \frac{1}{2}K_{33}\left(\hat{\mathbf{n}} \times \nabla \times \hat{\mathbf{n}}\right)^2, \tag{1.2}$$

where K_{11}, K_{22} and K_{33} are the splay, twist and bend elastic constants respectively, also known as the Frank elastic constants [8]. In case where the deformation involves only the polar angle θ between the director $\hat{\mathbf{n}}$ and the normal to the substrates can describe the orientation of director; in this case, the free energy density can be simplified as $f = \frac{1}{2}K\left(\frac{\partial\theta}{\partial z}\right)^2$ under the one-elastic constant approximation $K_{11} = K_{22} = K_{33} = K$. When the NLC is subject to an external electric field, the director reorients under the dielectric torque $\mathbf{M}_d$ to minimize the dielectric contribution to the elastic free energy Eq. (1.2). The dynamics of this orientation process is governed by the Ericksen-Leslie equation [9, 10]:

$$\mathbf{M}_d + \mathbf{M}_v + \mathbf{M}_e = 0, \tag{1.3}$$

where $\mathbf{M}_v$ and $\mathbf{M}_e$ are the viscous and elastic torques, respectively.

The optical properties are closely associated with the profile of the director orientation, particularly the mechanism by which polarized light propagates through the NLC slab. For example, when a monochromatic linearly polarized light beam impinges onto the NLC layer normally, the beam will propagate differently depending on the angle between the polarization of the input light and director. In a typical scenario where this angle is neither 0^o or 90^o, the beam is split into two waves

due to the birefringent nature of the NLC: an ordinary-wave (o-wave) with polarization perpendicular to $\hat{\mathbf{n}}$ and an extraordinary-wave (e-wave) with polarization parallel to $\hat{\mathbf{n}}$. The two waves experience different refractive indices in the NLC layer: $n_o = \sqrt{\varepsilon_\perp'}$ for the ordinary wave and an effective refractive index

$$n_{eff} = \frac{n_o n_e}{\sqrt{n_o^2 \cos^2 \vartheta + n_e^2 \sin^2 \vartheta}}, \tag{1.4}$$

for the extraordinary wave. $n_{eff}(\vartheta)$ depends on the angle ϑ between $\hat{\mathbf{n}}$ and the light propagation wave vector $\mathbf{k}$ [11]; $n_e = \sqrt{\varepsilon_{\square}'}$ is the extraordinary refractive index. $\varepsilon_\perp'$ and $\varepsilon_\parallel'$ are the dielectric permittivities at optical frequencies. The director profile is usually not homogenous along the z-axis, i.e. ϑ depends on z, thus n_{eff} is a function of z, i.e. $n_{eff}(z)$.

When the light propagates through the slab, there is an optical phase shift ΔL between the o-wave and e-wave because of the refractive indices difference,

$$\Delta L = \int_0^d \left[n_{eff}(z) - n_o \right] dz \tag{1.5}$$

Combining Eq. (1.4) and (1.5), we know that ΔL depends on the director orientation. This dependence enables us to control the value of ΔL by reorienting the director with an applied electric field. This is also known as electrically controlled birefringence (ECB), and is the working principle of many modern LC devices. In a standard ECB setup, incident light passes through a pair of crossed polarizers, separated by a classic sandwiched cell with transparent electrodes (typically indium tin oxide (ITO)) on both sides and NLCs filled in-between. The incident light with a

wavelength of λ becomes linearly polarized after the first polarizer and propagates through the NLC cell. The birefringent NLC introduces a phase shift between the o-wave and e-wave, and the light leaving the cell is normalized by a second polarizer. The transmitted light intensity of the exit light after the second polarizer is [3, 11]:

$$I = I_0 \sin 2\phi \sin^2 \frac{\pi \Delta L}{\lambda}, \tag{1.6}$$

where I_0 is the incident light intensity, ϕ is the angle between the direction of the incident light's polarization and the projection of the director orientation at $z = 0$ onto the substrate plane.

Equation (1.6) is valid only for the case of normal incidence; however it is also very important to calculate the transmitted light intensity resulting from oblique incidence, such as determining the off-axis viewing angle performance of a LC device. In the following calculation, we ignore the reflection difference between *s*-polarization and *p*-polarization beams.

Consider a beam passing through air and into a LC cell with an oblique angle of incidence θ_i. The boundary condition requires that the tangential component of the $\mathbf{k}$-vector remain constant at the interface, for both o-wave and e-wave.

$$k_{o//} = k_{e//} = k \sin \theta_i . \tag{1.7}$$

The Fresnel equation for a uniaxial medium is [11]:

$$\left(N^2 - \varepsilon_\perp\right)\left[\varepsilon_{//} N_z^2 + \varepsilon_\perp \left(N_x^2 + N_y^2\right) - \varepsilon_{//}\varepsilon_\perp\right] = 0, \tag{1.8}$$

where $N = kc/\omega$ is the refractive index of a given wave in a given medium, c is the speed of light in vacuum, and ω is the angular frequency. According to Eq. (1.8), for the o-wave and e-wave in this configuration:

$$N^2 = N_x^2 + N_z^2 \quad (N_y^2 = 0), \tag{1.9}$$

$$N_x^2 + N_z^2 = \varepsilon_\perp = n_o^2, \tag{1.10}$$

$$N_x^2 / n_e^2 + N_z^2 / n_o^2 = 1. \tag{1.11}$$

On the other hand, N can be expressed in terms of the wave vector k:

$$\begin{aligned} N_{xo} &= N_{xe} = k \sin\theta c / \omega \\ N_{zo} &= k_{zo} c / \omega \\ N_{ze} &= k_{ze} c / \omega \end{aligned} \quad . \tag{1.12}$$

Using Eq. (1.12), we can solve Eq. (1.10) and (1.11) to find the *z*-axis component of the o-wave and e-wave vectors:

$$k_{zo} = \frac{2\pi}{\lambda}\left(n_o^2 - \sin^2\theta_i\right)^{\frac{1}{2}}, \tag{1.13}$$

$$k_{ze} = \frac{2\pi n_o^2}{\lambda}\left(1 - \frac{\sin^2\theta_i}{n_e^2}\right)^{\frac{1}{2}}. \tag{1.14}$$

Therefore the total phase shift ΔL is:

$$\Delta L = \left(k_{ze} - k_{zo}\right) d = \frac{2\pi n_o d}{\lambda}\left[\left(1 - \frac{\sin^2\theta_i}{n_e^2}\right)^{\frac{1}{2}} - \left(1 - \frac{\sin^2\theta_i}{n_o^2}\right)^{\frac{1}{2}}\right]. \tag{1.15}$$

By combining Eqs. (1.15) and (1.6), we can calculate the intensity of transmitted light for the case of oblique incidence case. In Chapter 5, we use Eqs. (1.15) and (1.6) to determine the birefringence of the electrically induced nematic phase.

1.3 Dielectric relaxations in nematic liquid crystals

When an external electric field is applied to NLCs, the director reorients under the action of the dielectric torque, whose density is [3]: $\mathbf{M}(t) = \mathbf{D}(t) \times \mathbf{E}(t)$, where $\mathbf{E}(t)$ and $\mathbf{D}(t)$ are the electric field and electric displacement at the moment of time t, respectively. From the superposition rule in the classic electrodynamics [12],

$$\mathbf{D}(t) = \varepsilon_0 \mathbf{E}(t) + \int_{-\infty}^{t} \mathbf{P}(t,\ t')dt' = \varepsilon_0 \mathbf{E}(t) + \varepsilon_0 \int_{-\infty}^{t} \boldsymbol{\alpha}(t,\ t')\mathbf{E}(t')dt' \tag{1.16}$$

where $\mathbf{P}(t,\ t')$ is the polarization component, which describes the contribution of the past electric field $\mathbf{E}(t')$ to the current electric displacement $\mathbf{D}(t)$; $\boldsymbol{\alpha}(t,\ t')$ is called a decay function or step response function. For a medium in which the dielectric properties do not change with time, $\boldsymbol{\alpha}(t,\ t')$ can be represented as the function of the time difference $t - t'$, i.e.,

$$\boldsymbol{\alpha}(t,\ t') = \boldsymbol{\alpha}(t - t') \tag{1.17}$$

Eq. (1.17) ensures that a harmonic electric field $E(t) = E_\omega e^{-i\omega t}$ will lead to a harmonic electric displacement $\mathbf{D}(t)$ with the same frequency ω.

$$\mathbf{D}(t) = \varepsilon_0 \left(\mathbf{I} + \int_0^\infty \boldsymbol{\alpha}(t - t') e^{i\omega(t-t')} d(t - t') \right) \mathbf{E}_\omega e^{i\omega t} = \mathbf{D}_\omega e^{i\omega t}, \tag{1.18}$$

where $\mathbf{D}_\omega$ is the dielectric response equation in the frequency domain:

$$\mathbf{D}(\omega) = \varepsilon_0 \boldsymbol{\varepsilon}(\omega) \mathbf{E}_\omega, \tag{1.19}$$

and we define a frequency dependent dielectric permittivity tensor $\boldsymbol{\varepsilon}(\omega)$:

$$\boldsymbol{\varepsilon}(\omega) = \mathbf{I} + \int_0^\infty \boldsymbol{\alpha}(t - t') e^{i\omega(t-t')} d(t - t'). \tag{1.20}$$

In order to understand the dielectric response of material under an electric field, it is necessary to know the behavior of $\boldsymbol{\varepsilon}(\omega)$.

There are different relaxation modes contributing to the dielectric permittivity tensor $\boldsymbol{\varepsilon}$. The three major contributions are as follows: 1) electronic polarization which is caused by the electron cloud displacement induced by an electric field; 2) molecular polarization which is attributed to the atom re-positioning; 3) orientational polarization due to the reorientation of the dipole moment, which is determined by the competition between the electric field strength and the thermal entropy. All these three polarizations contribute to $\boldsymbol{\varepsilon}$ within a certain limited frequency of the electric field, above which the contributions disappear.

The characteristic relaxation times of these three sources are very different; they can be estimated by Planck's equation $\tau = \dfrac{h}{2\pi \mathrm{E}}$, where E is the energy of the process and $h = 6.63\times10^{-34}\,\mathrm{J\cdot s}$ is the Planck constant. For electronic polarization, the electronic excitation energy is $\mathrm{E} \approx 1\,\mathrm{eV} = 1.602\times10^{-19}\,\mathrm{J}$, thus its characteristic time is $\tau_e \approx 10^{-16}\,\mathrm{s}$; while the molecular polarization is related to intra-molecular vibration with $\mathrm{E} \approx 10^{-4}\,\mathrm{eV} = 1.602\times10^{-23}\,\mathrm{J}$, so $\tau_m \approx 10^{-12}\,\mathrm{s}$. The fastest time of electric field change achieved in this work is in the order of $10^{-8}\,\mathrm{s}$, thus both electronic and molecular polarizations dynamics can be considered as instantaneous processes. The contributions from electronic and molecular polarizations to $\boldsymbol{\varepsilon}$ shall obey:

$$\int_{-\infty}^{t} \boldsymbol{\alpha}_k(t-t')\mathbf{E}(t')dt' = \mathbf{E}(t)\int_{-\infty}^{t} \bar{\boldsymbol{\alpha}}_k(t-t')dt', \qquad (1.21)$$

therefore, they can be considered as frequency independent, and the electric displacement $\mathbf{D}(t)$ only depends on the current electric field $\mathbf{E}(t)$.

The orientational polarization is related to the permanent molecular dipole moment reorientation under the electric field. This relaxation is relatively slow, with a characteristic time from 10^{-9} s to 10^{-2} s. This is comparable to the electric field change rate; therefore Eq. (1.21) is no longer valid in this case; consequently, $\boldsymbol{\varepsilon}$ does depend on both the current $\mathbf{E}(t)$ and past fields $\mathbf{E}(t')$, so does the electric displacement $\mathbf{D}(t)$.

In order to understand the effect of different contributions on the dielectric response, one needs to know the corresponding step response function $\boldsymbol{\alpha}_k(t,t')$. There are a few models which have been developed to define the $\boldsymbol{\alpha}(t,t')$ [13]; among them, Debye model is the most widely accepted one [14]. In the Debye model, $\boldsymbol{\alpha}(t,t')$ is assumed to decay exponentially with a relaxation time constant τ,

$$\alpha\left(t-t'\right)=\bar{\alpha}\exp\left(-\frac{t-t'}{\tau}\right), \tag{1.22}$$

where $\bar{\alpha}$ is a coefficient to be determined later. Combining with Eq. (1.20), we obtain the frequency dependent dielectric permittivity:

$$\varepsilon\left(\omega\right)=1+\frac{\bar{\alpha}\tau}{1-i\omega\tau}. \tag{1.23}$$

From Eq. (1.23), the real part of $\varepsilon\left(\omega\right)$ will decrease from the "static" value $\varepsilon_l=1+\bar{\alpha}\tau$ to $\varepsilon_h=1$ at high frequency $\omega\to\infty$; however ε_h should be higher than 1 because of the contributions from electronic and molecular polarizations. With ε_l and ε_h in Eq. (1.23), the step response function in Debye model is:

$$\alpha(t-t') = \frac{\varepsilon_l - \varepsilon_h}{\tau} \exp\left(-\frac{t-t'}{\tau}\right). \tag{1.24}$$

Combing Eq. (1.24) and (1.20), we obtain the dielectric dispersion properties in the frequency domain:

$$\varepsilon(\omega) = \varepsilon_h + \frac{\varepsilon_l - \varepsilon_h}{1 - i\omega\tau_r}. \tag{1.25}$$

For NLCs, the dielectric properties change with time as the director reorients under the electric field. Therefore Eq. (1.17) is no longer valid, thus dielectric dispersion properties of the NLC cannot be described by the Debye model, except the scenario where the director is constant. A new model to describe the step response function is necessary for NLCs with their dielectric properties changing with time because of director reorientation. The first analysis of the effect of dielectric relaxation on the director dynamics was presented by Yin *et al.* [4], and later Mottram *et al.*[15]. However, these models only consider the single relaxation in the parallel component of the dielectric permittivity. In practice, NLCs show multiple relaxations in both parallel ($\varepsilon_{\parallel}$) and perpendicular ($\varepsilon_{\perp}$) permittivities,

$$\varepsilon_\eta(\omega) = \varepsilon_{h\eta} + \sum_{j=1}^{N} \frac{\varepsilon_{mj\eta} - \varepsilon_{m(j+1)\eta}}{1 - i\omega\tau_{j\eta}}, \ \eta = \parallel, \perp \tag{1.26}$$

where $\varepsilon_{m1,\eta} = \varepsilon_{l,\eta}$ and $\varepsilon_{m(N+1),\eta} = \varepsilon_{h,\eta}$; the parallel and perpendicular symbols represent the components parallel and perpendicular to the director. When the Debye model considers multiple relaxations, it accounts for the dielectric relaxation process and describes the electric displacement and the dielectric permittivity, and thus the dielectric torque, which are essential to understand the director dynamics. We will

present a general model to take account of multiple relaxations with the details in Chapter 2.

To understand the effects of dielectric relaxation on the director dynamics, we need to know the dielectric dispersion properties of the NLCs. These can usually be obtained experimentally by using the capacitance method. A typical setup is shown in Figure 1.2, where a thermally stabilized NLC cell in a hot stage is connected to an impedance analyzer that transmits data to a computer. The electrodes with a well defined area A can be made of indium tin oxide (ITO), aluminum or gold; aluminum or gold are preferred for high frequency (> 500 KHz) measurements due to their high conductivity with respect to ITO. The alignment layer promotes the desired director orientation to measure the corresponding dielectric permittivities, for example, to measure the parallel permittivity $\varepsilon_{\parallel}$, homeotropic polyimide such as SE-7511L and SE-1211L from Nissan, JAL-659 from Japan Synthetic Rubbing is used; planar polyimide such as rubbed PI-2555 from Dupont is used to measure $\varepsilon_{\perp}$.

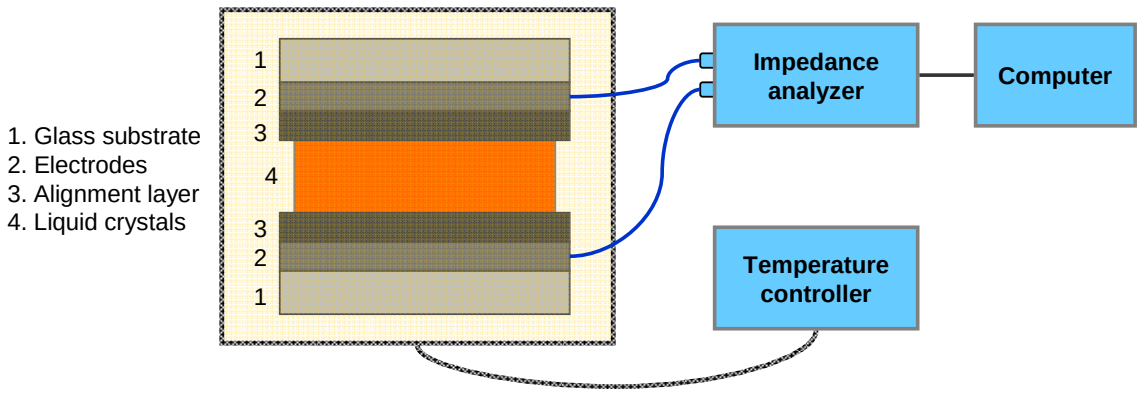

Figure 1.2. Illustration of the capacitance method to measure the dielectric dispersion properties of NLCs.

The impedance analyzer collects frequency dependent impedance data of the cell, $Z(f) = Z_r - iZ_i$, where Z_r and Z_i are the real and imaginary impedances respectively. From classic electric theory, we know,

$$Z(f) = \frac{1}{i\omega C(f)}, \tag{1.27}$$

where ω is the angular frequency, C is the capacitance of the cell, and

$$C(f) = \varepsilon_0 \varepsilon(f) \frac{A}{d}, \ \varepsilon(f) = \varepsilon_r(f) - i\varepsilon_i(f). \tag{1.28}$$

Combing Eqs. (1.27) and (1.28), one obtains the dielectric permittivities:

$$\begin{aligned} \varepsilon_r(f) &= \frac{d}{2\pi\varepsilon_0 A} \cdot \frac{-Z_i(f)}{\left[Z_r^2(f) + Z_i^2(f)\right] f} \\ \varepsilon_i(f) &= \frac{d}{2\pi\varepsilon_0 A} \cdot \frac{Z_r(f)}{\left[Z_r^2(f) + Z_i^2(f)\right] f} \end{aligned}. \tag{1.29}$$

With Eq. (1.29), we obtain the frequency dependent dielectric permittivities by measuring impedance as a function of frequency at different temperatures, set by the temperature controller.

Combining knowledge of dielectric dispersion properties, and the Debye model, we will proceed to discuss the effect of the dielectric relaxation on director dynamics in Chapter 2.

1.4 Electric field induced nematic isotropic phase transition

The isotropic-nematic phase transition in LCs can be phenomenologically described by the Landau-de Gennes theory [16]. The free energy density of the system near the phase transition is approximated by a low order polynomial of the scalar order parameter *S*,

$$f_n = f_0 + \frac{1}{2}a\left(T - T^*\right)S^2 - \frac{1}{3}b\left(T\right)S^3 + \frac{1}{4}c\left(T\right)S^4, \tag{1.30}$$

where f_0 is the free energy density in the isotropic phase without an external field; *a*, $b\left(T\right)$ and $c\left(T\right)$ are material parameters, T is the temperature and T^* is the lowest temperature at which the isotropic phase is metastable. In the equilibrium state, we should have:

$$\partial f_n / \partial S = 0 \tag{1.31}$$

For a given temperature *T*, we can solve Eq. (1.31) with Eq. (1.30), the solution is the equilibrium value of *S* corresponding to this specific temperature. When an NLC with a positive dielectric anisotropy is subjected to an external electric field $\mathbf{E}$, a new term must be added into the free energy density [3]

$$f = f_n - \frac{\varepsilon_0 \Delta\varepsilon_m}{3}E^2 S, \tag{1.32}$$

where $\Delta\varepsilon_m$ is the maximum dielectric anisotropy corresponding to $S = 1$. For NLCs with positive dielectric anisotropy, this new term is negative so the applied electric can enhance orientational order. If the NLC is initially in the isotropic phase, $S = 0$, then the applied field may be large enough to trigger a phase transition from the isotropic to nematic phase, where S becomes non-zero. This change is determined by

temperature and the field strength. Lelidis and Durand *et al.* have systematically studied this isotropic to nematic phase transition as induced by an external electric field [17-19]. The temporal profile of S change, i.e. the dynamics of S during the electrically induced phase transition, is considered as the dynamics of the phase transition, which is described by the Landau-Khalatnikov model,

$$\gamma \frac{\partial S}{\partial t} + \frac{\partial f_n}{\partial S} = 0, \tag{1.33}$$

where γ is the effective viscosity coefficient.

In the electrically induced phase transition, the permanent dipole moments interact with the applied field **E**, and their reorientation leads to a polar ordering, which is represented by a macroscopic polarization **P**. In the Landau-Khalatnikov model, the dynamics of polarization is treated as an instantaneous process, therefore the dynamics of the induced phase transition is solely described by the dynamics of nonpolar order parameter *S*. However when the characteristic time of the electric field becomes comparable to that of the polarization dynamics, the temporal evolution of polarization can no longer be considered instantaneous. In this work, Chapter 5, we will present a model to describe the electrically induced phase transition by taking account of both dynamics of the nonpolar order parameter and the macro polarization; the descriptions are based on the Langevin equations.

Chapter 2

EFFECTS OF DIELECTRIC DISPERSION ON THE DIRECTOR DYNAMICS

The anisotropy of dielectric permittivity of liquid crystals (LCs) is one of the most important features of these materials. It leads to the phenomenon of director reorientation in the electric field. The latter, often called the Frederiks effect, is a well-known phenomenon that has numerous electro-optical applications, most notably in LC displays [1, 3, 20, 21]. Until very recently, a theoretical description of the effect has been limited by the assumption that the dielectric response is instantaneous. Namely, it was assumed that the electric displacement **D** at the moment of time t is determined solely by the electric field **E** acting on the LCs at the very same moment t. In other words, the effects of a finite rate of dielectric relaxation have been neglected. Such an approach is certainly valid when the characteristic rise time τ_U of the voltage driving the LC cell is much longer than the time of the dielectric relaxation τ_r. However, modern applications require faster and faster switching times and a number of researchers demonstrated fast switching by decreasing the rise time of the driving voltage, down to the values comparable to the

characteristic dielectric relaxation time, $\tau_U \leq \tau_r$, which is in the range of tens of nanoseconds for materials such as the classic 4-cyano-4′-n-pentyl-biphenyl (5CB) [22], and in the microsecond range for the so-called dual-frequency nematics liquid crystals (DFNLCs) [23]. In the DFNs, the dielectric anisotropy $\Delta\varepsilon = \varepsilon_{\|} - \varepsilon_{\perp}$ is positive at low frequencies f, and negative at high f; the frequency at which $\Delta\varepsilon$ changes sign is called the crossover frequency, f_c. In the regime $\tau_U \leq \tau_r$, the assumption of an instantaneous response is not valid anymore and experimental observations can no longer be explained by the conventional theory of dielectric response [4]. For example, a sharp increase of the applied dc voltage is perceived by the LC as a high-frequency ac excitation that in DFNLCs might lead a curious behavior of $\hat{\mathbf{n}}$ that first reorients away from the direction of $\mathbf{E}$ and then realigns parallel to it, as has been demonstrated both experimentally [4] and theoretically [4, 15].

To describe the "dielectric memory effect" (DME), i.e., dielectrically-induced $\hat{\mathbf{n}}$ reorientation in the regime $\tau_U \leq \tau_r$, we previously developed a model [4] of dielectric response in which the dielectric torque density has been calculated for a nematic LC in which $\varepsilon_{\|}$ experiences just one relaxation with a characteristic time τ_r; $\varepsilon_{\perp}$ was assumed a frequency-independent constant. For $\tau_U >> \tau_r$, the model [4] coincides with the classic theory, in which the director dynamics depends only on the "instantaneous" value of the electric field and the effective $\Delta\varepsilon$ that measures the strength and direction of the dielectric torque is determined by its value at low f. For $\tau_U \leq \tau_r$, however, the model [4] predicts a very different scenario: the dielectric

torque contains, in addition to the standard "instantaneous" contribution, which in this case has an effective $\Delta\varepsilon$ that corresponds to the high f, also a "memory" contribution proportional to the difference in $\varepsilon_{\|}$ values at low and high f's. Not only the "instantaneous" and "memory" terms depend on different values of permittivities, they are even of opposite signs in DFNLCs, enabling the curious effect mentioned above, namely, reorientation of $\hat{\mathbf{n}}$ away from $\mathbf{E}$ and then parallel to $\mathbf{E}$ when the DFNLC is driven by a sharp voltage pulse. A similar model that also considered a single Debye-type relaxation process in the parallel permittivity of a DFNLC, has been proposed by Mottram and Brown later [15].

The single-relaxation assumption of the models [4, 15] is certainly a limitation, as most LCs exhibit multiple processes of relaxation that involve not only $\varepsilon_{\|}$ but also $\varepsilon_{\perp}$ [13]. In this thesis, we generalize the description of the DME [4], by lifting the restriction of a single relaxation process and considering multiple relaxations that might occur in both $\varepsilon_{\|}$ and $\varepsilon_{\perp}$. The generalized model allows us to extend the description from a relatively limited class of proper DFNLCs with $\tau_r \approx 0.01-1\,\text{ms}$, to practically the entire class of nematic LCs which include materials such as cyanobiphenyls, typical compounds used in electro-optical research and applications, with τ_r in the range of nanoseconds. Note that many "regular" LCs with positive dielectric anisotropy, such as cyanobiphenyls, are in fact also DFNLCs, with that difference that f_c is in the MHz region [24-27], rather than in the kHz range. The model also allows us to describe materials with multiple relaxations, as we

demonstrate at the example of mixtures of 5CB and MLC2048. Finally, it allows one to optimize the driving schemes of LC cells to achieve a faster response time.

Below, we start with the theoretical model and then describe the experimental data relevant to different scenarios of dielectric relaxation. Namely, we study 5CB as an example of the material with relaxations in both $\varepsilon_{\parallel}$ and $\varepsilon_{\perp}$; mixtures of 5CB with MLC2048 in which there are multiple relaxations of $\varepsilon_{\parallel}$; finally, a material with $\Delta\varepsilon < 0$ in which the DME leads to a faster response time (as opposed to the case of $\Delta\varepsilon > 0$ in which the DME delays the director reorientation).

2.1 Theory

The LC director reorients in an applied electric field under the action of the dielectric torque, whose density is [3]: $\mathbf{M}(t) = \mathbf{D}(t) \times \mathbf{E}(t)$, where $\mathbf{E}(t)$ and $\mathbf{D}(t)$ are the electric field and electric displacement at the moment of time t, respectively. In the widely accepted standard approach, $\mathbf{D}(t)$ is determined by the instantaneous current electric field, i.e. $\mathbf{D}(t) = \varepsilon_0 \boldsymbol{\varepsilon} \mathbf{E}(t)$, where ε_0 is the vacuum dielectric constant, and $\boldsymbol{\varepsilon}$ is the relative dielectric permittivity tensor. However, when $\tau_U \leq \tau_r$, the dielectric relaxation will affect the director reorientation and can no longer be ignored [4, 15]. Below, we develop a model of dielectric response in the uniaxial nematic LCs by taking into account that both $\varepsilon_{\parallel}$ and $\varepsilon_{\perp}$ might experience multiple relaxations with the increase of f.

Using the superposition rule [12], $\mathbf{D}(t)$ can be written as Eq. (1.16). The step response function $\boldsymbol{\alpha}(t,\ t')$ is also called the decay function, since it vanishes when $t-t'\to\infty$. When the dielectric properties of the medium do not change with time, for example, in solid crystals, $\boldsymbol{\alpha}(t,\ t')$ can be described as a function of time interval $t-t'$, as described by Eq. (1.17). However, Eq. (1.17) is no longer valid for the case where the LC director reorients (it would be valid if $\hat{\mathbf{n}}$ is somehow frozen and does not reorient in the changing electric field). Below we search for the analog of Eq. (1.16) that takes into account the changes in the dielectric permittivity caused by director reorientation.

The dielectric response tensor function $\boldsymbol{\alpha}(t,\ t')$ of the nematic LCs is comprised of different relaxation modes $\boldsymbol{\alpha}_k(t,\ t')$:

$$\boldsymbol{\alpha}(t,\ t')=\sum_k \boldsymbol{\alpha}_k(t,\ t'). \tag{2.1}$$

If the *kth* relaxation process is sufficiently fast as compared to the change of electric field, the electric field and the director field can be considered as constant during the relaxation period, i.e.,

$$\int_{-\infty}^{t}\boldsymbol{\alpha}_k(t,\ t')\mathbf{E}(t')dt'=\mathbf{E}(t)\int_{-\infty}^{t}\bar{\boldsymbol{\alpha}}_k(t,\ t')dt', \tag{2.2}$$

where $\bar{\boldsymbol{\alpha}}_k(t,t')=\boldsymbol{\alpha}_k(t,t')$ for a fixed director orientation $\hat{\mathbf{n}}(t')=\hat{\mathbf{n}}(t)$. We split $\boldsymbol{\alpha}(t,\ t')$ into two terms: a "fast" one, $\boldsymbol{\alpha}_f(t,\ t')$, that includes relaxations which are much faster than the director reorientation and the electric field change (and thus satisfy Eq. (2.2)), and a "slow" one $\boldsymbol{\alpha}_s(t,\ t')$:

$$\boldsymbol{\alpha}(t,\ t')=\boldsymbol{\alpha}_f(t,\ t')+\boldsymbol{\alpha}_s(t,\ t'). \tag{2.3}$$

Note that both fast and slow parts of $\boldsymbol{\alpha}(t,\ t')$ are sums with terms originating from different relaxation processes. Now we can rewrite the electric displacement $\mathbf{D}(t)$ in nematic LC as:

$$\mathbf{D}(t) = \varepsilon_0 \boldsymbol{\varepsilon}_f(t)\mathbf{E}(t) + \varepsilon_0 \int_{-\infty}^{t} \boldsymbol{\alpha}_s(t,\ t')\mathbf{E}(t')dt', \tag{2.4}$$

where the "fast" part $\boldsymbol{\varepsilon}_f$ of the relative dielectric permittivity tensor is defined as:

$$\boldsymbol{\varepsilon}_f(t) = \mathbf{I} + \int_{-\infty}^{t} \boldsymbol{\alpha}_f(t,\ t')dt'. \tag{2.5}$$

In the local frame associated with the director, $\boldsymbol{\varepsilon}_f(t)$ has a stationary diagonal form, thus its time dependence originates from reorientation of the local frame and is determined solely by the current director field $\hat{\mathbf{n}}(t)$:

$$\boldsymbol{\varepsilon}_f(t) = \varepsilon_{f\perp}\mathbf{I} + \left(\varepsilon_{f\parallel} - \varepsilon_{f\perp}\right)\hat{\mathbf{n}}(t) \otimes \hat{\mathbf{n}}(t), \tag{2.6}$$

where $\varepsilon_{f\parallel}$ and $\varepsilon_{f\perp}$ are the components of the dielectric tensor in the diagonal form, and $\otimes$ is the external product of two vectors, the operation result being a tensor with components $[\hat{\mathbf{n}}(t) \otimes \hat{\mathbf{n}}(t)]_{ij} = n_i(t)n_j(t)$.

When $\hat{\mathbf{n}}$ reorients, the polarization parallel to $\hat{\mathbf{n}}$ should be dragged by the director; this is because a high potential barrier arouses when the polarization deviates from the long axis of molecules. This is also true for the rotation of the polarization perpendicular to $\hat{\mathbf{n}}$. It is also assumed that this dragging of polarization shall not affect the reorientation of individual molecules. This assumption is reasonable even when the rotation speed of $\hat{\mathbf{n}}$ is comparable to the relaxation speed of the polarization, because the slow rotation of all molecules should not substantially affect the fast flip-flop of the small number of molecules which are responsible for the dielectric

relaxation. In a local frame $\left[\hat{\mathbf{l}}(t),\ \hat{\mathbf{m}}(t),\ \hat{\mathbf{n}}(t)\right]$, where $\hat{\mathbf{l}}(t)$, $\hat{\mathbf{m}}(t)$ and $\hat{\mathbf{n}}(t)$ represent the three principal axes, rotating with an angular velocity $\Omega(t) = -\dot{\hat{\mathbf{n}}}(t)\times\hat{\mathbf{n}}(t)$, one can write:

$$\dot{\hat{\mathbf{v}}}(t) = \boldsymbol{\Omega}(t)\times\hat{\mathbf{v}}(t) = -\left[\dot{\hat{\mathbf{n}}}(t)\times\hat{\mathbf{n}}(t)\right]\times\hat{\mathbf{v}}(t), \tag{2.7}$$

where $\hat{\mathbf{v}}(t) = \hat{\mathbf{l}}(t)$ or $\hat{\mathbf{m}}(t)$ or $\hat{\mathbf{n}}(t)$. The dielectric relaxation in this frame depends on $\hat{\mathbf{n}}$ rotation and thus we can describe $\boldsymbol{\alpha}_s(t,\ t')$ in the laboratory frame by the diagonal components $\alpha_{\parallel}(t-t')$ along $\hat{\mathbf{n}}$ and $\alpha_{\perp}(t-t')$ perpendicular to $\hat{\mathbf{n}}$, when $\hat{\mathbf{n}}$ is fixed:

$$\boldsymbol{\alpha}_s(t,\ t') = \alpha_{\parallel}(t-t')\hat{\mathbf{n}}(t)\otimes\hat{\mathbf{n}}(t') + \alpha_{\perp}(t-t')\left[\hat{\mathbf{l}}(t)\otimes\hat{\mathbf{l}}(t') + \hat{\mathbf{m}}(t)\otimes\hat{\mathbf{m}}(t')\right]. \tag{2.8}$$

Therefore, we can write the dielectric torque density as:

$$\mathbf{M}(t) = \mathbf{D}(t)\times\mathbf{E}(t) = \varepsilon_0\left\{\left(\varepsilon_{f\parallel} - \varepsilon_{f\perp}\right)\hat{\mathbf{n}}(t)\left[\hat{\mathbf{n}}(t)\cdot\mathbf{E}(t)\right] + \int_{-\infty}^{t}\boldsymbol{\alpha}_s(t,\ t')\mathbf{E}(t')dt'\right\}\times\mathbf{E}(t). \tag{2.9}$$

The integral term in Eq. (2.9), absent in the conventional "instantaneous" dielectric response theory, describes the DME. The dielectric displacement $\mathbf{D}(t)$ depends on the prehistory of the electric field $\mathbf{E}(t')$.

Below, we demonstrate that the DME can also be described within an approach based on the free energy. We introduce the dielectric term $F_E(t)$ in the free energy density of a LC cell under an applied voltage:

$$F_E(t) = -\left\{\frac{1}{2}\left[\varepsilon_0\varepsilon_{f\perp}\mathbf{E}^2(t) + \left(\varepsilon_{f\parallel} - \varepsilon_{f\perp}\right)\left(\mathbf{n}(t)\cdot\mathbf{E}(t)\right)^2\right] + \varepsilon_0\mathbf{E}(t)\int_{-\infty}^{t}\boldsymbol{\alpha}_s(t,t')\mathbf{E}(t')dt'\right\}, \tag{2.10}$$

where the electric field $\mathbf{E}(t) = -\nabla V(t)$ satisfies Maxwell equation $\nabla \times \mathbf{E}(t) = 0$. Variations of Eq. (2.10) allow one to find the distribution of the potential $V(t)$ inside the cell $-\frac{\delta F_E(t)}{\delta V(t)} = \nabla \cdot \mathbf{D}(t) = 0$, and to obtain Eq. (2.9):

$$\mathbf{M}(t) = \sum_{\hat{\mathbf{v}}(t)} \hat{\mathbf{v}}(t) \times \frac{\delta F_E(t)}{\delta \hat{\mathbf{v}}(t)}, \tag{2.11}$$

where $\hat{\mathbf{v}}(t) = \hat{\mathbf{l}}(t)$ or $\hat{\mathbf{m}}(t)$ or $\hat{\mathbf{n}}(t)$. Note that the numerical coefficients for the two terms in Eq. (2.10) are different, equal to "1/2" for the first ("instantaneous") term but to "1" for the second ("memory") term. The coefficient 1/2 enters the standard expression for the dielectric energy when change of the electric field is adiabatically slow and the system has enough time to respond. On the other hand, the coefficient value 1 corresponds to the energy of a permanent dipole in the electric field.

The slow step response functions $\alpha_{\parallel}(t-t')$ and $\alpha_{\perp}(t-t')$ in Eq. (2.8) can be reconstructed from the frequency dispersion of the dielectric tensor. Slow relaxation processes in LCs are caused by reorientation of permanent molecular dipoles and usually obey the classic Debye theory of dielectric relaxation [14], with an exponential decay behavior and a Lorenzian behavior in the frequency domain:

$$\alpha_\eta(t-t') = \sum_i^{p_\eta} \frac{\delta\varepsilon_{i\eta}}{\tau_{i\eta}} \exp\left(-\frac{t-t'}{\tau_{i\eta}}\right), \qquad \eta = \parallel,\ \perp, \tag{2.12}$$

$$\alpha_\eta(\omega) = \sum_i^{p_\eta} \frac{\delta\varepsilon_{i\eta}}{1 - i\omega\tau_{i\eta}}, \qquad \eta = \parallel,\ \perp, \tag{2.13}$$

where $\delta\varepsilon_{i\eta}$ and $\tau_{i\eta}$ are the dielectric "strength" and the relaxation time of the *ith* relaxation of parallel or perpendicular component, respectively; p_η is the number of

slow relaxation processes for the parallel or perpendicular components of permittivity. Note that if the relaxation times of different processes are well separated, then the "strength" $\delta\varepsilon_{i\eta}$ of each of these processes can be defined in practice as the difference in the permittivities at frequencies below and above the characteristic frequency $\sim 1/\tau_{i\eta}$. If the relaxation times are close to each other, the value of $\delta\varepsilon_{i\eta}$ is found from the fitting of the dielectric permittivity dispersion curves. For other, non-Debye types of relaxations, such as Havriliak-Negami, Fuoss-Kirwood, or generalized Cole-Cole types [13], Eqs.(2.8) to (2.11) are still valid, and one only needs to modify Eqs. (2.12) and (2.13).

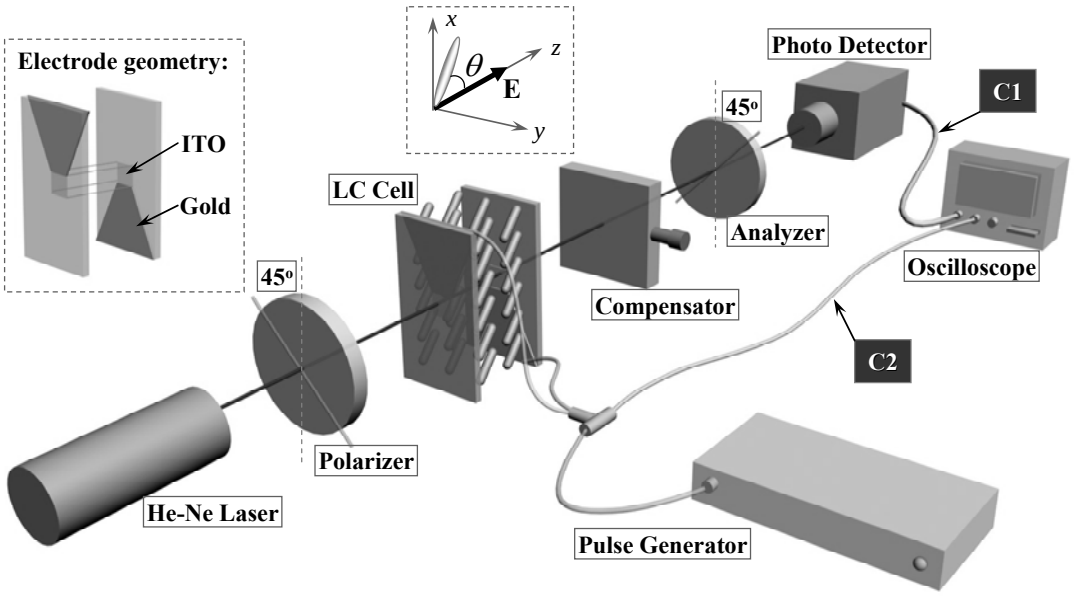

Figure 2.1. Experimental setup for the DME experiment.

To get a better insight into the physics of the DME, and the ways it can be verified experimentally, we consider below a typical case of a homogeneously aligned nematic cell subject to an electric field $\mathbf{E}(t)$ along the *z*-axis that is normal to

the bounding plates, Figure 2.1. Let $\theta(z,\ t)$ be the angle between the director $\hat{\mathbf{n}}(t)$ and the normal of the substrate at the time t, measured at a point z. We assume that $\theta(z,\ t)$ does not depend on the in-plane $x,\ y$ coordinates, and that the director rotates only in the $x-z$ plane (x-axis is the projection of the alignment axis onto the cell substrates). The Erickson-Leslie equation describing the director dynamics in absence of material flow then can be written as [28, 29]:

$$-\gamma_1 \frac{\partial\theta(z,\ t)}{\partial t} = M(t) - \left[K_1 \sin^2\theta(z,\ t) + K_3 \cos^2\theta(z,\ t)\right] \times \frac{\partial^2\theta(z,\ t)}{\partial z^2}, \qquad (2.14)$$

where K_1 and K_3 are the splay and bend elastic constants, respectively; γ_1 is the rotational viscosity coefficient, and the dielectric torque is of the form

$$M(t) = \varepsilon_0 E(t) \left[\begin{array}{l} \left(\varepsilon_{f\parallel} - \varepsilon_{f\perp}\right)\sin\theta(z,\ t)\cos\theta(z,\ t)E(t) + \\ \sin\theta(z,\ t)\int_{-\infty}^{t}\cos\theta(z,\ t')\sum_{i=1}^{p_\parallel}\frac{\delta\varepsilon_{i\parallel}}{\tau_{i\parallel}}\exp\left(-\frac{t-t'}{\tau_{i\parallel}}\right)E(t')dt' - \\ \cos\theta(z,\ t)\int_{-\infty}^{t}\sin\theta(z,\ t')\sum_{j=1}^{p_\perp}\frac{\delta\varepsilon_{j\perp}}{\tau_{j\perp}}\exp\left(-\frac{t-t'}{\tau_{j\perp}}\right)E(t')dt' \end{array} \right]. \qquad (2.15)$$

Equations (2.14) and (2.15) determine the profile of $\theta(z,\ t)$, i.e., the temporal and spatial profile of the director field. Since $\hat{\mathbf{n}}$ is simultaneously the optical axis in the uniaxial nematic LC, its behavior can be traced experimentally by measuring the light intensity transmitted through the cell and a pair of crossed linear polarizers. When the x-axis is at the angle of 45° to the axes of the two polarizers, Figure 2.1, the (normalized) transmitted light intensity

$$I(t) = \sin^2\frac{\Delta\varphi(t)}{2} \qquad (2.16)$$

is determined by the optical phase shift of the nematic cell [11],

$$\Delta\varphi(t) = \frac{2\pi n_o}{\lambda}\int_0^d \left\{ n_e / \left[n_o^2 \sin^2\theta(z,\ t) + n_e^2 \cos^2\theta(z,\ t) \right]^{1/2} - 1 \right\} dz\,, \quad (2.17)$$

where n_o and n_e are the ordinary and extraordinary refractive indices of the LC, respectively; d is the cell gap. Since we are only interested in a short time interval at the beginning of switching where the DME occurs, i.e. in about a few tens of nanoseconds for the case of 5CB and a few tens of microseconds for conventional DFNs, the backflow effect, whose characteristic time is in the range of milliseconds [30, 31], can be ignored, which justifies the form of Eq. (2.14).

Equation (2.15) clearly demonstrates how the relaxation processes will affect the director dynamics. Depending on the rate with which the electric field is changing, any relaxation process would qualify either as "fast" (if its relaxation time is shorter than τ_U) or as "slow". The "fast" contributes to the "instantaneous" torque represented by the first term in Eq. (2.15). The "slow" contributes to one of the two "memory" integrals in Eq. (2.15), associated with either the parallel or the perpendicular component. The instantaneous and memory torques corresponding to different relaxation processes have generally different "strengths" determined by $\left(\varepsilon_{f\parallel} - \varepsilon_{f\perp}\right)$ that might be both positive and negative, and by $\delta\varepsilon_{i\eta}$ that is always positive, but enters Eq. (2.15) with a "+" sign for the parallel component and a "–" sign for the perpendicular component. The balance of all these contributions would define the temporal behavior of $\hat{\mathbf{n}}$, including the situations when the sense of director reorientation reverses with time. In the experimental part, we discuss situations that highlight different contributions to Eq. (2.15).

2.2 Experimental results and discussions

We choose three types of nematic materials (all purchased from E.M. Industries): (A). The classic nematic 5CB in which both $\varepsilon_{\|}$ and $\varepsilon_{\perp}$ experience dielectric relaxation with characteristic times in the range of 1-100 ns [24, 25]. (B). Nematic mixtures of 5CB and MLC2048 in which we observe multiple dielectric relaxations of $\varepsilon_{\|}$. MLC2048 is a conventional DFNLC; although it is by itself a mixture, it shows a single relaxation time and f_c=12 kHz at room temperature [32]. Multiple relaxations in $\varepsilon_{\|}$ of the 5CB-MLC2048 mixtures at different frequencies originate from the relaxations of different molecular components of the mixture. (C) Nematic mixture of MLC7026-100 and MLC2048, in which $\Delta\varepsilon$ is negative for all frequencies and $\varepsilon_{\|}$ experiences a single relaxation.

The cells were constructed by bonding two glass substrates coated with transparent Indium Tin Oxide (ITO) electrodes. In all experimental cells, on top of ITO, we used alignment layers that allow one to maximize the dielectric torque acting on $\hat{\mathbf{n}}$, which implies that $\hat{\mathbf{n}}$ and $\mathbf{E}$ make an angle close to 45^{o}, see for example [23].

(A) The 5CB cells were constructed with the reduced active area of the electrodes, about 500×500 μm^2 (through photolithography patterning). An additional layer of gold is coated as the electric leads to the ITO areas. The purpose of using a small active area and gold coating is to reduce the RC load of the circuit, thus to reduce the delay of the electric field applied to the cell [22]; the estimated delay from the RC load was 0.5 ns. As an alignment layer, we deposited a SiO_x film on top of the

gold and the ITO layers. The actual tilt angle θ_b between $\hat{\mathbf{n}}$ and the *z*-axis was determined to be 51.2° by measuring the phase shift with a Soleil Babinet SB-10 (Optics for Research) optical phase compensator. The cell gap was 4.4 μm as determined by the interference method.

(B) The cells with 5CB-MLC2048 mixtures were assembled with an active area of ITO about 1×1 mm^2. The estimated delay from the RC load was 20 ns, i.e. much lower than the shortest relaxation time ~ 200 ns measured for these mixtures. The alignment layer was a SiO_x film, yielding $\theta_b = 50.2^o$. The cell gap was 3.5 μm.

(C) The cells with MLC7026-100 and MLC2048 mixtures were assembled with a larger active area of about 25×25 mm^2. The delay from the RC load was 0.3 μs which is lower than the typical relaxation times 2 μs of these mixtures. The alignment layer was a mixture of polyimide PI2555 (DuPont) and polyimide JSR659AL (Japan Synthetic Rubber) in proportion 95 wt. % to 5 wt. %, yielding $\theta_b = 20.5^o$. The cell gap was 12.5 μm.

The cells were placed between two crossed polarizers with its *x*-axis making an angle 45° with respect to the transmission axes of the crossed polarizer and analyzer, Figure 2.1. The optical phase compensator SB-10 with a controllable phase delay $\Delta\varphi'$ is inserted between the cell and the analyzer in order to adjust the normalized transmitted light intensity,

$$I(t) = \sin^2\left[\frac{\Delta\varphi(t) + \Delta\varphi'}{2}\right] \tag{2.18}$$

in such a way that in the absence of an electric field, $I(t)$ is about 1/2 of its maximum possible value. For this setting, the sensitivity of the system to the light

intensity change caused by the director reorientation is maximized. We have chosen $\Delta\varphi'$ in such a way that a field-induced (small) reorientation of $\hat{\mathbf{n}}$ *parallel* to $\mathbf{E}$ corresponds to an *increase* of $I(t)$. The intensity of the laser beam (He-Ne laser, 633 nm) that passes through the cell is measured by a TIA-500S-TS photo detector (Terahertz Technologies Inc.) with the response time less than 1 ns. The recorded signal is displayed on a Tektronix TDS 210 digital oscilloscope, which is connected to a computer via IEEE-488 cable for data storage and analysis [IEEE-488 is also commonly known as the General Purpose Interface Bus (GPIB)].

In order to observe the DME in 5CB, the rise time of the voltage τ_U should be comparable to or less than the dielectric relaxation time τ_r of 5CB, which is only a few tens of nanoseconds in the nematic phase [25]. We use a pulse generator HV1000 (Direct Energy Inc.) capable of producing any voltage pulse up to 1000 V. The time evolution $U(t)$ of the pulse front for this generator can be approximated by the exponential function $U(t) = U_0\left[1 - \exp(-\frac{t}{\tau_U})\right]$, where $\tau_U = 6$ ns.

In the nanosecond range, one needs to take a particular care of any factors influencing the data, such as the cell area (see above) and the finite speed of signal propagation. For a typical 50 Ω coaxial electric cable, this speed is ~ 0.8 *c*, where *c* is the speed of light in vacuum; the signal needs roughly 4 ns to propagate by about 1 m. For our experimental set-up, Figure 2.1, we measured the time difference for signal propagation between two arms connecting the nematic cell and the oscilloscope. One arm is comprised of the laser beam propagation between the cell and the photo detector and the electric signal propagation to the oscilloscope through

the cable C1; the second arm is the electrical connection for the applied voltage through the cable C2, Figure 2.1. We determined the time difference between these two arms to be 16 ns. This time difference was used to synchronize the data coming through the two arms.

To observe the DME in DFNLCs and in nematics with negative dielectric anisotropy, in which τ_r is much longer than in 5CB, we used the waveform generator WFG500 (FLC Electronics AB) combined with KH7602M amplifier (Krohn-Hite Corporation). The voltage increase rate was 476 V/μs.

The experiments were performed at the temperature 23 °C and 30 °C for 5CB (at which the dielectric parameters have been determined for a broad range of frequencies [24, 25]). For the rest of materials and mixtures, the experiments were performed at room temperature, close to 23 °C ; the frequency dependencies of permittivities were measured in the laboratory by using the Schlumberger 1260 Impedance/Gain-Phase Analyzer.

(A). 5CB: dielectric relaxations in both $\varepsilon_{\|}$ and $\varepsilon_{\perp}$.

5CB is a material of the so-called "dielectrically-positive" type, which means that at low frequencies (up to the MHz region), $\Delta\varepsilon = \varepsilon_{\|} - \varepsilon_{\perp} > 0$. As demonstrated by Gestblom and Wróbel [26] and Belyaev *et al* [24, 33], both $\varepsilon_{\|}$ and $\varepsilon_{\perp}$ show relaxation with different characteristic times, so that $\Delta\varepsilon$ changes sign from positive to negative and then back to positive as the frequency increases. The $\varepsilon_{\|}$ component shows even two relaxation processes [24], however, the second process has a

relaxation time less than 1 ns and can be neglected in our experiment with $\tau_U \sim 10$ ns. We model the dielectric dispersion curves of 5CB using the Debye approach [14]:

$$\varepsilon_{\parallel}(\omega) = \varepsilon_{h\parallel} + \frac{\varepsilon_{l\parallel} - \varepsilon_{h\parallel}}{1 - i\omega\tau_{\parallel}}, \varepsilon_{\perp}(\omega) = \varepsilon_{h\perp} + \frac{\varepsilon_{l\perp} - \varepsilon_{h\perp}}{1 - i\omega\tau_{\perp}} \tag{2.19}$$

where the subscripts *l* and *h* refer to the low-frequency and high-frequency values of the permittivities, respectively.

The dielectric properties in LCs are temperature-dependent. The literature data for dispersion curves of 5CB are available only for some temperatures (mostly for 30 °C and 23 °C [24-27, 33-35]); although the temperature dependence of the relaxation time are well characterized [36, 37]. We first discuss the dispersion curves, based on Eq. (2.19), at these two temperatures.

For 30 °C, to fit $\varepsilon_{\parallel}(\omega)$, we used $\varepsilon_{l\parallel} = 17.5$ measured by Cummins et al. [34] and $\varepsilon_{h\parallel} = 4.6$ measured by Belyaev *et al.*. [24, 33]. We also used $\tau_{\parallel} = 36$ ns from the experiment by Kreul *et al.* [25]. For $\varepsilon_{\perp}(\omega)$ at 30 °C, we use $\varepsilon_{l\perp} = 7.0$ measured in Ref. [34], and $\varepsilon_{h\perp} = 2.4$ and $\tau_{\perp} = 3.5$ ns from the experiments in Refs. [24, 33].

For 23 °C, to fit $\varepsilon_{\parallel}(\omega)$, we measured $\varepsilon_{l\parallel} = 19.0$ in our laboratory [38] and determined $\varepsilon_{h\parallel} = 5.0$ from the expression $\delta\varepsilon_{\parallel} = \varepsilon_{l\parallel} - \varepsilon_{h\parallel} = 2\varepsilon''_{\max}$, where $\varepsilon''_{\max} \approx 7$ is the maximum of the imaginary part of the parallel dielectric permittivity measured at 23 °C in Refs. [35]. We used $\tau_{\parallel} = 64$ ns from the experiments by Kreul *et al.*[25], which were also performed at 23 °C. For $\varepsilon_{\perp}(\omega)$, we measured $\varepsilon_{l\perp} = 6.5$ and used $\varepsilon_{h\perp} = 2.4$ and $\tau_{\perp} = 3.5$ ns from the experiments in Refs. [24, 33]. The last two values have been measured at 30 °C; however, we do not expect significant temperature

changes for $\varepsilon_{h\perp}$ and $\tau_{\perp}$ because of the barrier-free character of the corresponding relaxation process.

With the parameters above, one can reconstruct the frequency dependencies of dielectric permittivities for 5CB, Eq. (2.19), Figure 2.2. These data closely resemble the experimental finding in Refs. [24-27, 33-35]. Namely, at $f > 9$ MHz for $23\,^{\circ}\mathrm{C}$ and 10 MHz for $30\,^{\circ}\mathrm{C}$, 5CB behaves as a dielectrically *negative* material with $\Delta\varepsilon < 0$, while at even higher frequencies, $f > 32$ MHz for $23\,^{\circ}\mathrm{C}$ and 45 MHz for $30\,^{\circ}\mathrm{C}$, it returns to $\Delta\varepsilon > 0$.

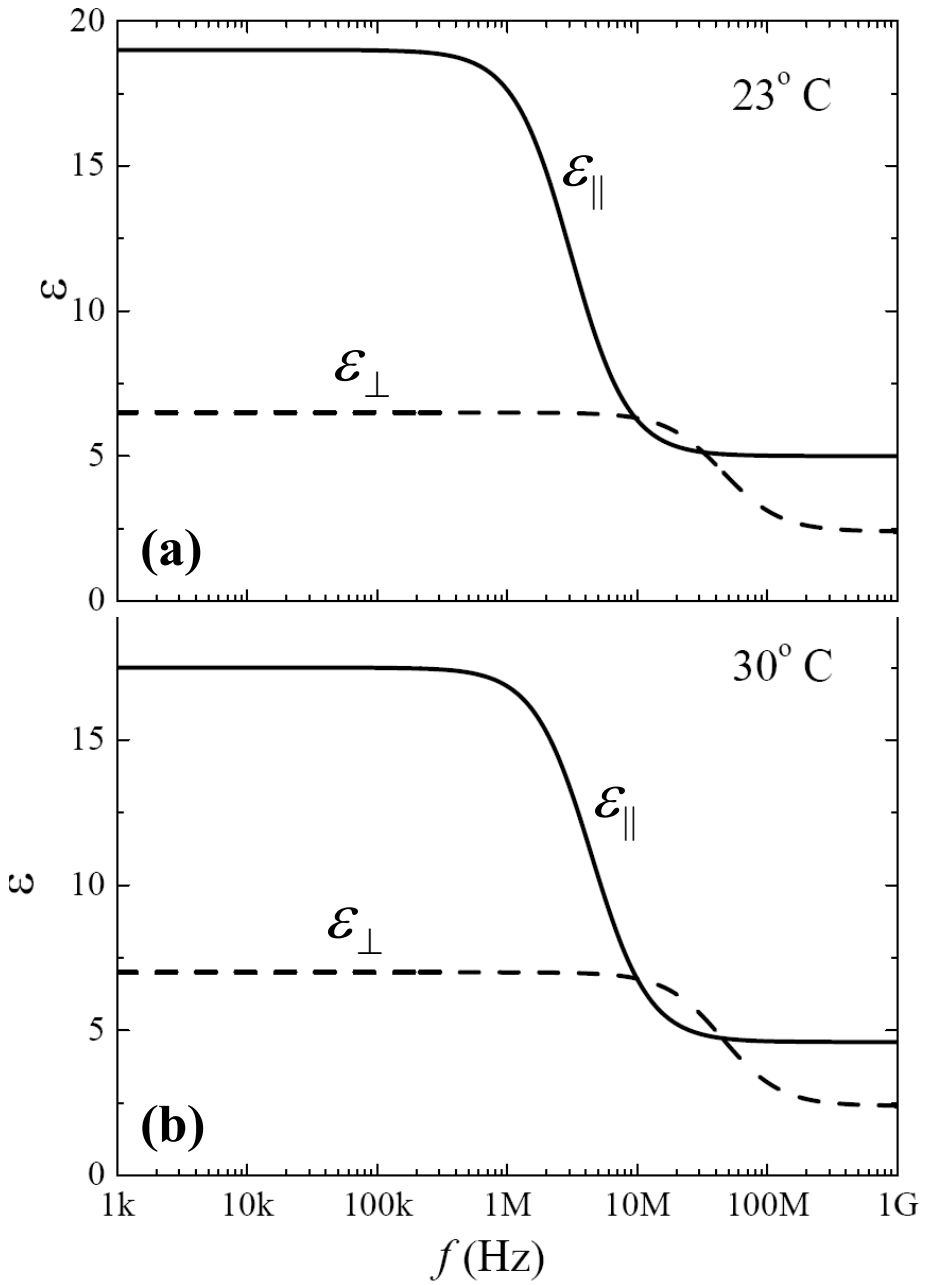

Figure 2.2. Dielectric dispersion curves of 5CB based on the Debye model, Eq. (2.19), with the parameters (a) $\varepsilon_{l\|}=19.0$, $\varepsilon_{h\|}=5.0$ and $\tau_{\|}=64\,\text{ns}$; $\varepsilon_{l\perp}=6.5$, $\varepsilon_{h\perp}=2.4$ and $\tau_{\perp}=3.5\,\text{ns}$ for $23\,^{\circ}\text{C}$; and (b) $\varepsilon_{l\|}=17.5$, $\varepsilon_{h\|}=4.6$ and $\tau_{\|}=36\,\text{ns}$; $\varepsilon_{l\perp}=7$, $\varepsilon_{h\perp}=2.4$ and $\tau_{\perp}=3.5\,\text{ns}$ for $30\,^{\circ}\text{C}$.

With the dielectric dispersion of 5CB modeled in Figure 2.2, we now proceed to the study of the DME, by exploring the director dynamics at the very beginning of a sharp voltage pulse, Figure 2.3. The most interesting feature is that within the first 15 ns of the voltage pulse, the optical signal changes very little, despite a sharp increase of the field. A similar "delay" phenomenon has been observed by Takanashi *et al.* [22] for a similar 5CB cell driven by similar sharp rising pulses. The experiments in both Takanashi *et al.* and our case were designed to reduce the delays in the optical response associated with finite rise time of the equipment used. Namely, in our case all the relevant rise time (in the RC circuit, photo detector and oscilloscope) were each about 1 ns or less; therefore, the "delay" in optical response cannot be attributed to the finite rise time of the experimental set-up. Clark and co-authors [22, 39] came to the same conclusion and suggested that the delay might be caused by the dielectric relaxation. Below we demonstrate that our model above does provide both qualitative and quantitative explanation of the delay as the result of dielectric relaxation.

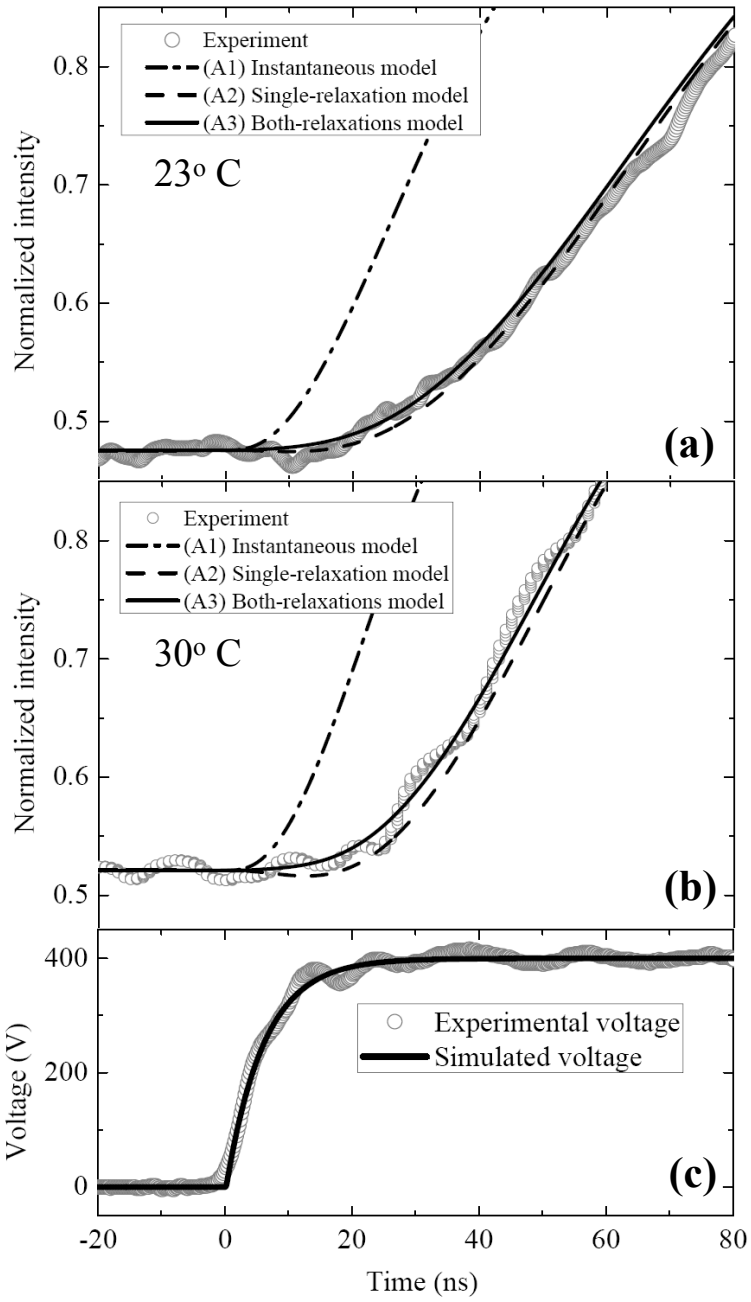

Figure 2.3. Normalized transmitted light intensity of a 5CB cell after a pair of crossed polarizers under an applied voltage versus time: (a) 23 °C and (b) 30 °C; (c) Applied voltage pulse with simulated voltage (solid curve). The circles are the experimental data; the curves represent simulations with different models as indicated by the labels.

To fit the experimental data in Figure 2.3, we used three theoretical models of dielectric response, namely, (i) the standard instantaneous approach, (ii) the single-relaxation model [4] and (iii) the present model in which both $\varepsilon_{\|}$ and $\varepsilon_{\perp}$ relaxations are taken into consideration. The dielectric torque Eq. (2.15) assumes different forms in these three models. Namely, $\varepsilon_{f\eta}$ in Eq. (2.15) should be taken as $\varepsilon_{h\eta}$ and $\delta\varepsilon_{\eta} = \varepsilon_{l\eta} - \varepsilon_{h\eta}$ if one takes into account the relaxation of a corresponding permittivity component and as $\varepsilon_{l\eta}$ if one assumes no relaxation (in this case, obviously, $\delta\varepsilon_{\eta} = 0$). Therefore, the dielectric torque has the following forms in the three models:

(A1) In the standard instantaneous approach, in which we neglect all the dielectric relaxation processes,

$$M_{\mathrm{A1}}(t) = \varepsilon_0\left(\varepsilon_{f\|} - \varepsilon_{f\perp}\right)\sin\theta(z,\,t)\cos\theta(z,\,t)E^2(t), \tag{2.20}$$

where $\varepsilon_{f\|} = 19.0$ and $\varepsilon_{f\perp} = 6.5$ for $23\,^{\circ}\mathrm{C}$; $\varepsilon_{f\|} = 17.5$ and $\varepsilon_{f\perp} = 7.0$ for $30\,^{\circ}\mathrm{C}$ (according to the data for 5CB in Figure 2.2.)

(A2) In the single-relaxation model [4], where only the dielectric relaxation of $\varepsilon_{\|}$ is considered:

$$M_{\mathrm{A2}}(t) = \varepsilon_0 E(t)\sin\theta(z,\,t)\left[\begin{array}{l}\left(\varepsilon_{f\|} - \varepsilon_{f\perp}\right)\cos\theta(z,\,t)E(t) + \\ \int_{-\infty}^{t}\cos\theta(z,t')\dfrac{\delta\varepsilon_{\|}}{\tau_{\|}}\exp\left(-\dfrac{t-t'}{\tau_{\|}}\right)E(t')dt'\end{array}\right], \tag{2.21}$$

where $\delta\varepsilon_{\|} = 14.0$, $\varepsilon_{f\|} = 5.0$ and $\tau_{\|} = 64$ ns; $\varepsilon_{f\perp} = 6.5$ for $23\,^{\circ}\mathrm{C}$; $\delta\varepsilon_{\|} = 12.9$, $\varepsilon_{f\|} = 4.6$ and $\tau_{\|} = 36$ ns; $\varepsilon_{f\perp} = 7.0$ for $30\,^{\circ}\mathrm{C}$ (according to Figure 2.2.)

(A3) In the present model in which both $\varepsilon_{\|}$ and $\varepsilon_{\perp}$ relaxations are taken into consideration:

$$M_{A3}(t)=\varepsilon_0 E(t)\left[\begin{array}{l}\left(\varepsilon_{f\parallel}-\varepsilon_{f\perp}\right)\sin\theta(z,\,t)\cos\theta(z,\,t)E(t)+\\ \sin\theta(z,\,t)\int_{-\infty}^{t}\cos\theta(z,\,t')\frac{\delta\varepsilon_{\parallel}}{\tau_{\parallel}}\exp\left(-\frac{t-t'}{\tau_{\parallel}}\right)E(t')dt'-\\ \cos\theta(z,\,t)\int_{-\infty}^{t}\sin\theta(z,\,t')\frac{\delta\varepsilon_{\perp}}{\tau_{\perp}}\exp\left(-\frac{t-t'}{\tau_{\perp}}\right)E(t')dt'\end{array}\right]. \quad (2.22)$$

where $\delta\varepsilon_{\parallel}=14.0$, $\varepsilon_{f\parallel}=5.0$ and $\tau_{\parallel}=64$ ns; $\delta\varepsilon_{\perp}=4.1$, $\varepsilon_{f\perp}=2.4$ and $\tau_{\perp}=3.5$ ns for 23 °C; $\delta\varepsilon_{\parallel}=12.9$, $\varepsilon_{f\parallel}=4.6$ and $\tau_{\parallel}=36$ ns; $\delta\varepsilon_{\perp}=4.6$, $\varepsilon_{f\perp}=2.4$ and $\tau_{\perp}=3.5$ ns for 30 °C, as in Figure 2.2.

With the known values of the dielectric torque, Eqs. (2.20), (2.21) and (2.22), one can simulate the dynamics of $\hat{\mathbf{n}}$ using Eq. (2.14) and then simulate the behavior of the transmitted light through the cell using Eqs. (2.17) and (2.18). In the Erickson-Leslie equation (2.14), one can neglect the elastic term. The reason is that for high voltages, $\hat{\mathbf{n}}$ reorients practically uniformly in the bulk of the cell, with elastic distortions taking place only within a very thin layer near the substrates. As the used voltage 400 V is about 400 times larger than the Frederiks threshold for 5CB, the thickness of the subsurface layer where $\hat{\mathbf{n}}$ experiences distortions is only $\xi\sim d\sqrt{\Delta\theta}/400\sim 1$ nm; here $\Delta\theta\sim 0.01$ rad (or less) is the angle of $\hat{\mathbf{n}}$ reorientation during the "delay" interval (the estimate follows from the fact that the phase retardation does not change much during this period). Therefore, the elastic contribution in Eq. (2.14) to the transmitted light intensity changes is negligibly small as compared to the dielectric term, as the ratio $\xi/d<10^{-3}$ is very small.

The electric pulse was simulated as $U(t) = U_0\left[1 - \exp\left(-\frac{t}{\tau_U}\right)\right]$, where $\tau_U = 6$ ns, Figure 2.3. In Eq. (2.14), we used the values of rotational viscosity $\gamma_1 = 0.1$ kg m^{-1} s^{-1} at 23 °C and $\gamma_1 = 0.059$ kg m^{-1} s^{-1} at 30 °C, as measured by Wu and Wu [40]. Finally, in the simulations of light transmission, Eqs. (2.17) and (2.18), we used $n_o = 1.52$ and $n_e = 1.70$ for both temperatures, as measured in our laboratory at 633 nm.

The simulated light transmittance in Figure 2.3 clearly demonstrates that the "delay" effect is well described by the dielectric relaxation model. The standard instantaneous approach (A1) predicts no delay (except for the first few nanoseconds when the exponentially growing voltage still remains relatively low). The models (A2) and (A3) of dielectric relaxation both show that the optical response is delayed with respect to the front of electric pulse. The delay is caused by the "wrong" sense of director reorientation at the beginning of electric pulse. The sharp front of the pulse is perceived by the LC as a high-frequency excitation, at which the dielectric anisotropy $\Delta\varepsilon$ is different from the low-frequency values. In particular, the model (A2) which accounts only for the relaxation of $\varepsilon_{\parallel}$, predicts an initial decrease in $I(t)$, as at the high frequency, $\Delta\varepsilon = \varepsilon_{h\parallel} - \varepsilon_{l\perp} < 0$ and $\hat{\mathbf{n}}$ reorients away from the field. After some time, $\hat{\mathbf{n}}$ begins to reorient toward $\mathbf{E}$, as $\Delta\varepsilon > 0$ at the low f. Although the model (A2) explains the apparent delay (as the result of an initially "wrong" direction of reorientation), it slightly overestimates the effect, as it considers $\Delta\varepsilon$ always negative at high f. The model (A3) which accounts for relaxations of both components, is a

bit more accurate, as it is only in the limited frequency region, between the relaxation frequencies for $\varepsilon_{\|}$ and $\varepsilon_{\perp}$, that $\Delta\varepsilon < 0$. At higher f, above the relaxation frequency of $\varepsilon_{\perp}$, $\Delta\varepsilon$ is positive. As a result, the reorientation of $\hat{\mathbf{n}}$ is first *toward* $\mathbf{E}$, then *away* from $\mathbf{E}$ and then *toward* $\mathbf{E}$ again. It appears that the model (A3) is the best suited to fit the experimental data, although the noise of experimental data does not allow one to see clearly an increase in the $I(t)$ curve caused by the initial rotation of $\hat{\mathbf{n}}$ toward $\mathbf{E}$.

Note that the literature data on $\tau_{\|}$ show some scattering. For example, Belyaev *et al.* [24] reported $\tau_{\|} \approx 25$ ns for 30 °C instead of 36 ns in [25] used in our simulations. With $\tau_{\|} \approx 25$ ns, the simulations still produce a delayed response, but the agreement with the experiment is not good and cannot be improved by varying other parameters such as rotational viscosity. We thus consider the values used in the dielectric dispersion model, Eq. (2.19) and Figure 2.2, as the best choice for the characterization of 5CB.

(B). 5CB-MLC2048 mixtures: multiple relaxations in $\varepsilon_{\|}$.

In this section, we explore the director dynamics in the materials with multiple relaxations in $\varepsilon_{\|}$ and little or no relaxation in $\varepsilon_{\perp}$. The experimental system is a mixture of 5CB and MLC2048 that shows the Debye type of dielectric relaxation, as evidenced by fitting the experimental data with the expression

$$\varepsilon_{\|}(\omega) = \varepsilon_{h\|} + \frac{\varepsilon_{l\|} - \varepsilon_{m\|}}{1 - i\omega\tau_1} + \frac{\varepsilon_{m\|} - \varepsilon_{h\|}}{1 - i\omega\tau_2}. \qquad (2.23)$$

Figure 2.4 illustrates an example of the mixture comprised of 7.0 wt. % 5CB and 93.0 wt. % MLC2048, in which the dispersion curves are well fitted by Eq. (2.23) with $\varepsilon_{l\|} = 10.4$, $\varepsilon_{m\|} = 5.3$, $\varepsilon_{h\|} = 3.5$, $\varepsilon_{\perp} = 6.4$, $\tau_1 = 6.0\ \mu s$ and $\tau_2 = 0.23\ \mu s$. The fitting parameters vary with the composition of the mixtures. In Figure 2.5, we present the concentration dependencies for relaxation time τ_1 and τ_2 and for the dielectric relaxation "strength" $\delta\varepsilon_1 = \varepsilon_{l\|} - \varepsilon_{m\|}$ and $\delta\varepsilon_2 = \varepsilon_{m\|} - \varepsilon_{h\|}$.

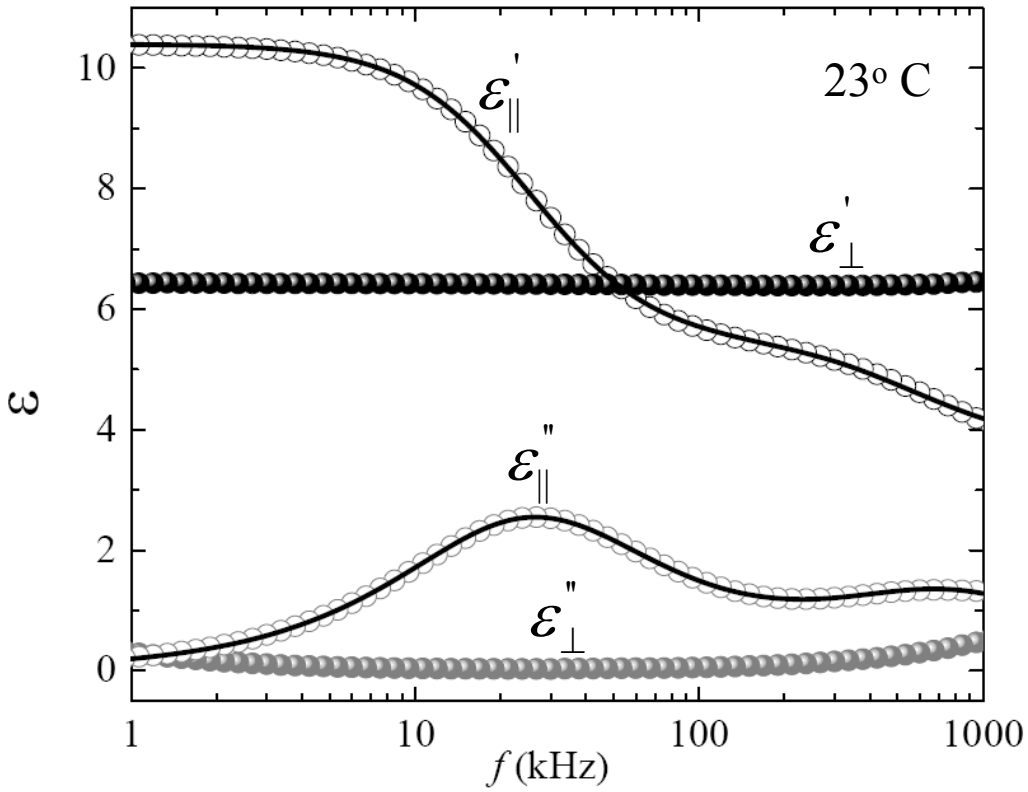

Figure 2.4. Experimental data on dielectric dispersion curves of the mixture with 7.0 wt. % 5CB and 93.0 wt. % MLC2048 for the real components ($\varepsilon_{\|}'$, $\varepsilon_{\perp}'$) and the imaginary components ($\varepsilon_{\|}''$, $\varepsilon_{\perp}''$) at room temperature 23 °C. The solid curves are fitted with Eq. (2.23) with the parameters $\varepsilon_{l\|} = 10.4$, $\varepsilon_{m\|} = 5.3$, $\varepsilon_{h\|} = 3.5$, $\varepsilon_{\perp} = 6.4$, $\tau_1 = 6.0\ \mu s$ and $\tau_2 = 0.23\ \mu s$.

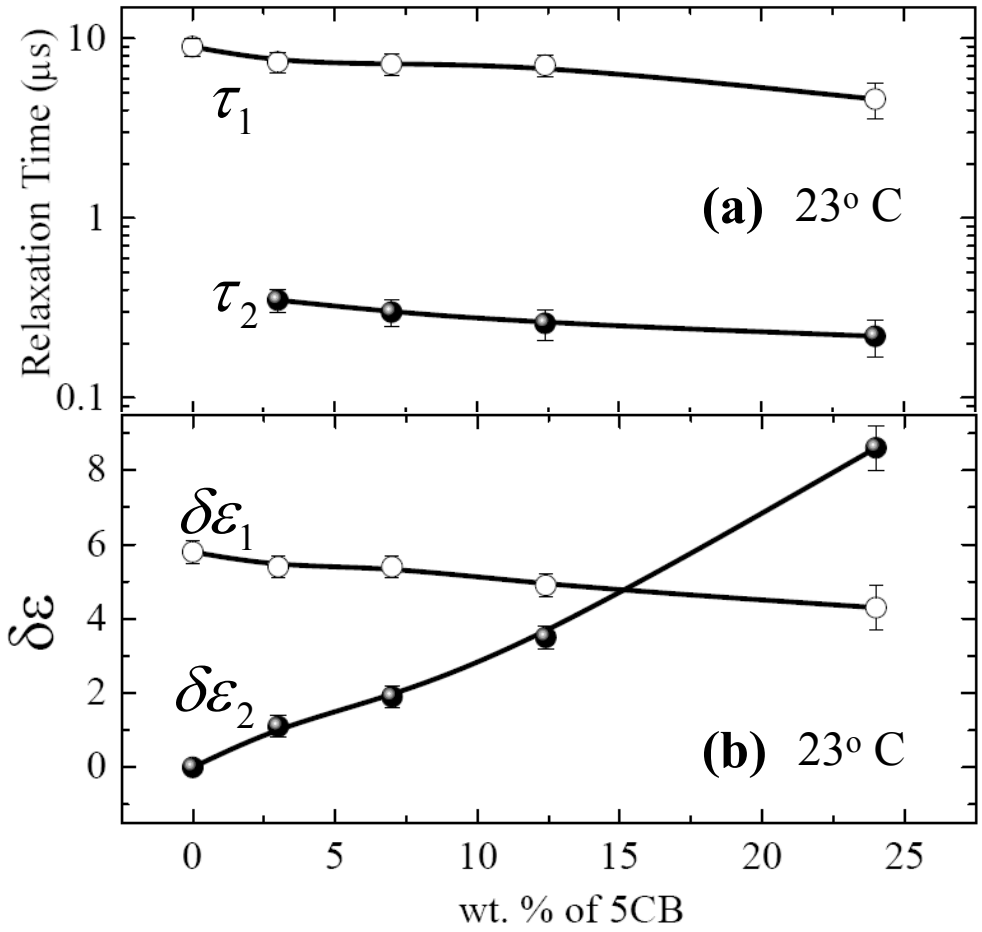

Figure 2.5. The first and second dielectric relaxation times (a) and dielectric strength (b) of the parallel component $\varepsilon_{\parallel}$ of the mixtures versus the weight concentration of the 5CB in MLC2048 at room temperature $23\,^{\circ}\mathrm{C}$.

The results of the DME experiment for the mixture with 7.0 wt. % 5CB and 93.0 wt. % MLC2048 driven by a sharply increasing DC pulse are shown in Figure 2.6. The voltage increases from 0 V to 200 V practically linearly, over $0.42\,\mu\mathrm{s}$. The experimental optical response corresponds to the director reorientation initially *perpendicular* to **E** over the first $\sim 2\,\mu\mathrm{s}$ (i.e., toward the planar state in the geometry

of experiment), followed by its reorientation *towards* **E** at the later times. Physically, the sharp front of pulse is perceived by the mixture as a high-frequency excitation for which the dielectric anisotropy is negative. To fit the data, we again used three models, in which $\varepsilon_{\perp} = 6.4$ remains constant:

(B1) The standard instantaneous approach, in which all the dielectric relaxation processes are neglected,

$$M_{\mathrm{B1}}(t) = \varepsilon_0\left(\varepsilon_{f\|} - \varepsilon_{\perp}\right)\sin\theta(z,\ t)\cos\theta(z,\ t)E^2(t), \tag{2.24}$$

where $\varepsilon_{f\|} = 10.4$ (according to Figure 2.4);

(B2) The single-relaxation model [4], where only one dielectric relaxation of $\varepsilon_{\|}$ is considered:

$$M_{\mathrm{B2}}(t) = \varepsilon_0 E(t)\sin\theta(z,\ t)\left[\begin{array}{l}\left(\varepsilon_{f\|} - \varepsilon_{\perp}\right)\cos\theta(z,\ t)E(t) + \\ \int_{-\infty}^{t}\cos\theta(z,\ t')\dfrac{\delta\varepsilon_1}{\tau_1}\exp\left(-\dfrac{t-t'}{\tau_1}\right)E(t')dt'\end{array}\right], \tag{2.25}$$

with $\delta\varepsilon_1 = 5.1$, $\varepsilon_{f\|} = 5.3$, and $\tau_1 = 6.0\ \mu\mathrm{s}$,.Figure 2.4;

(B3) The present model with both relaxations of $\varepsilon_{\|}$ taken into consideration:

$$M_{\mathrm{B3}}(t) = \varepsilon_0 E(t)\sin\theta(z,\ t)\left\{\begin{array}{l}\left(\varepsilon_{f\|} - \varepsilon_{\perp}\right)\cos\theta(z,\ t)E(t) + \\ \int_{-\infty}^{t}\cos\theta(z,\ t')\left[\dfrac{\delta\varepsilon_1}{\tau_1}\exp\left(-\dfrac{t-t'}{\tau_1}\right) + \dfrac{\delta\varepsilon_2}{\tau_2}\exp\left(-\dfrac{t-t'}{\tau_2}\right)\right]E(t')dt'\end{array}\right\}, \tag{2.26}$$

with $\delta\varepsilon_1 = 5.1$, $\delta\varepsilon_2 = 1.9$, $\tau_1 = 6.0\ \mu\mathrm{s}$ $\tau_2 = 0.23\ \mu\mathrm{s}$, and $\varepsilon_{f\|} = 3.5$, as in Figure 2.4.

In computer simulations of the optical response, we used $n_o = 1.501$, $n_e = 1.718$ in Eq. (2.17), measured in the laboratory; and $\gamma_1 = 0.39\ \mathrm{kg\ m^{-1}\ s^{-1}}$ in Eq. (2.14), as obtained by fitting the experimental data in Figure 2.6.

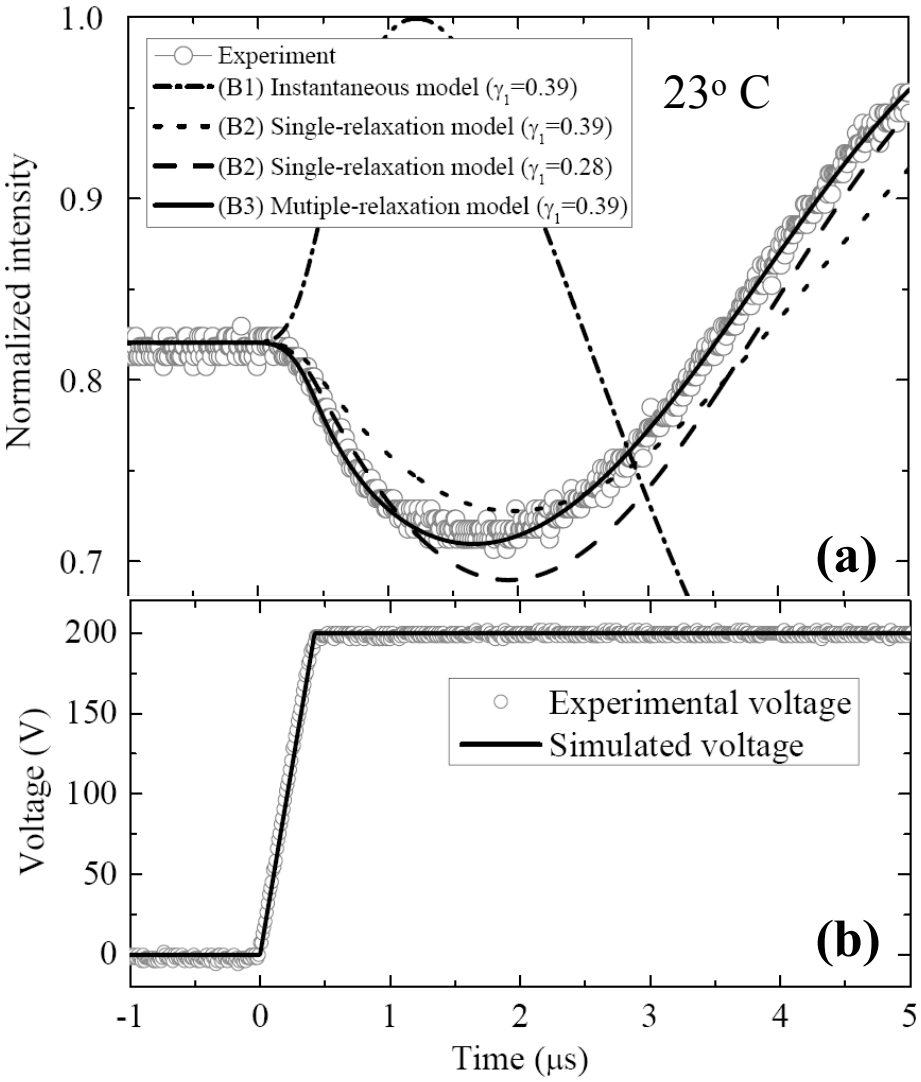

Figure 2.6. Normalized transmitted light intensity (a) and voltage (b) versus time for 7.0 wt. % 5CB + 93.0 wt. % MLC2048 mixture driven by fast-changing square pulses with a characteristic rise time less than 1 μs. The circles are the experimental data; the curves represent simulations with different models as indicated by the labels.

Comparison of the experimental and simulated data in Figure 2.6 demonstrates that the two-relaxation model (B3) fits the experiment very well. The instantaneous model (B1) predicts a wrong direction of reorientation while the single-relaxation model (B2) does predict the initial reorientation of $\hat{\mathbf{n}}$ perpendicular to $\mathbf{E}$ but does not agree with the experimental data in details. One can attempt to modify the parameters of model (B2) to better fit the data. For example, we change the rotational viscosity γ_1 in an attempt to better fit the experiment, dash-curve in Figure 2.6, yet it is not as good as the fitting by the model (B3).

(C). MLC7026-100-MLC2048 mixture: $\Delta\varepsilon < 0$ with a single relaxation in $\varepsilon_{\parallel}$.

So far, we considered the nematic LCs in which the static $\Delta\varepsilon$ is positive and the high-frequency $\Delta\varepsilon$ is smaller or even negative. Because of this, the DME slows down the director reorientation driven by sharp voltage pulses, as the front of pulse is perceived as a high-frequency excitation. In these materials, a faster response time can thus be obtained by taking τ_U *longer* rather than shorter[41]. However, in the case of nematic LCs in which the static $\Delta\varepsilon$ is negative, the DME might lead to faster director reorientation if the high-frequency $\Delta\varepsilon$ is larger (in the absolute value) than its low-frequency counterpart. Since the negative anisotropy materials are of prime importance in the flat panel display industry, forming the basis of the so-called "patterned vertical alignment" technology [42, 43], we conclude this work with a short illustration of the DME in these materials.

We studied a dielectrically-negative mixture obtained by mixing MLC7026-100 and DFN MLC2048, in weight proportion 53.7%: 46.3%. The mixture shows a

relaxation in $\varepsilon_{\parallel}$, Figure 2.7. The data can be fitted with the Debye model, Eq. (2.19), using $\varepsilon_{l\parallel} = 6.0$, $\varepsilon_{h\parallel} = 3.5$ and $\tau_{\parallel} = 2.1\ \mu s$. The relaxation time of the perpendicular component is smaller than 40 ns and thus we consider this component as a constant, $\varepsilon_{\perp} = 6.4$.

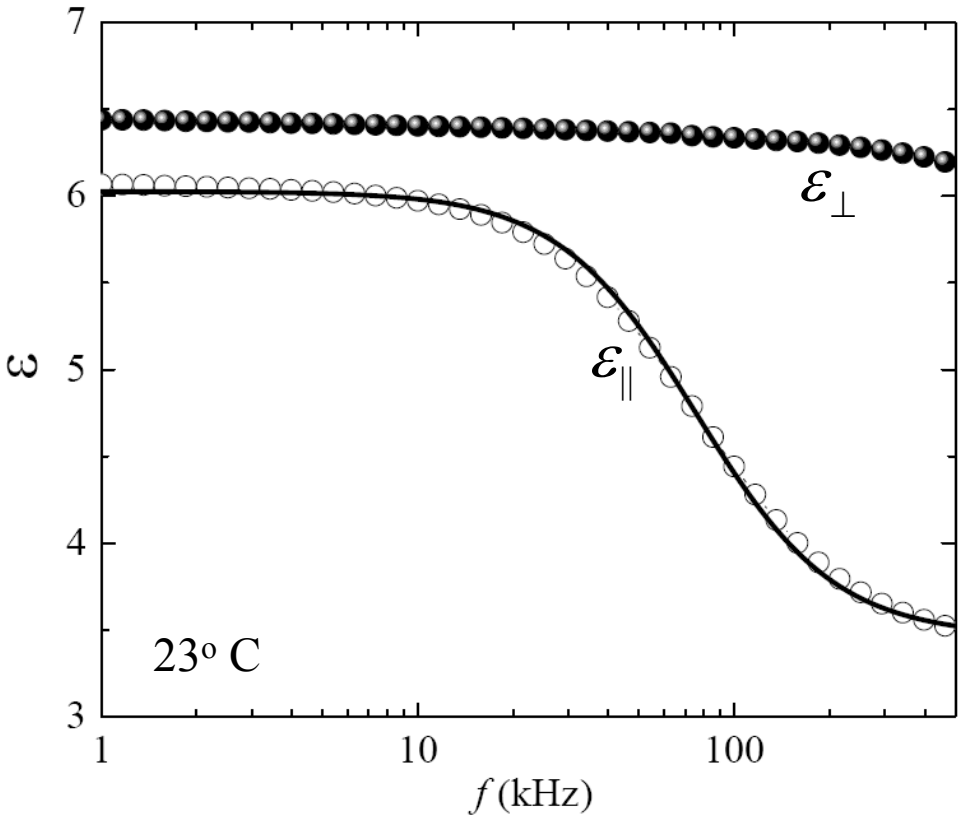

Figure 2.7. Dielectric dispersion curves for the real components ($\varepsilon_{\parallel}$, $\varepsilon_{\perp}$) of the 53.7 wt. % MLC7026-100 + 46.3 wt. % MLC2048 mixture at room temperature 23 °C. The solid curve is fitted with Eq. (2.19) with the parameters $\varepsilon_{h\parallel} = 3.5$, $\varepsilon_{l\parallel} = 6.0$, and $\tau_{\parallel} = 2.1\ \mu s$.

In Figure 2.8, we illustrate the effect of a rectangular pulse with a rise time of $0.5\ \mu s$. The experimental transmitted light intensity change corresponds to the director reorientation away from **E** for the whole driving interval. Physically, the sharp rising front of the pulse is perceived as a high-frequency excitation at which $\Delta\varepsilon$ remains negative but acquires an even larger absolute value as compared to that at the low frequencies. To fit the experiment, we used two models:

(C1) the standard instantaneous approach, in which all the dielectric relaxation processes are neglected,

$$M_{C1}(t) = \varepsilon_0\left(\varepsilon_{f\|} - \varepsilon_\perp\right)\sin\theta(z,\ t)\cos\theta(z,\ t)E^2(t), \tag{2.27}$$

where $\varepsilon_{f\|} = 6.0$, $\varepsilon_\perp = 6.4$, according to Figure 2.7;

(C2) the DME model in which the relaxation of $\varepsilon_\|$ is taken into consideration:

$$M_{C2}(t) = \varepsilon_0 E(t)\sin\theta(z,\ t)\left\{\begin{array}{l}\left(\varepsilon_{f\|} - \varepsilon_\perp\right)\cos\theta(z,\ t)E(t) + \\ \int_{-\infty}^{t}\cos\theta(z,\ t')\frac{\delta\varepsilon}{\tau}\exp\left(-\frac{t-t'}{\tau}\right)E(t')dt'\end{array}\right\}, \tag{2.28}$$

where $\delta\varepsilon = 2.5$, $\varepsilon_{f\|} = 3.5$, $\varepsilon_\perp = 6.4$ and $\tau = 2.1\ \mu s$, according to Figure 2.7.

In the simulations of optical response, we used $n_o = 1.49$ and $n_e = 1.65$ (measured in the laboratory), and $\gamma_1 = 0.15\ \text{kg m}^{-1}\ \text{s}^{-1}$ obtained by fitting the experimental data below.

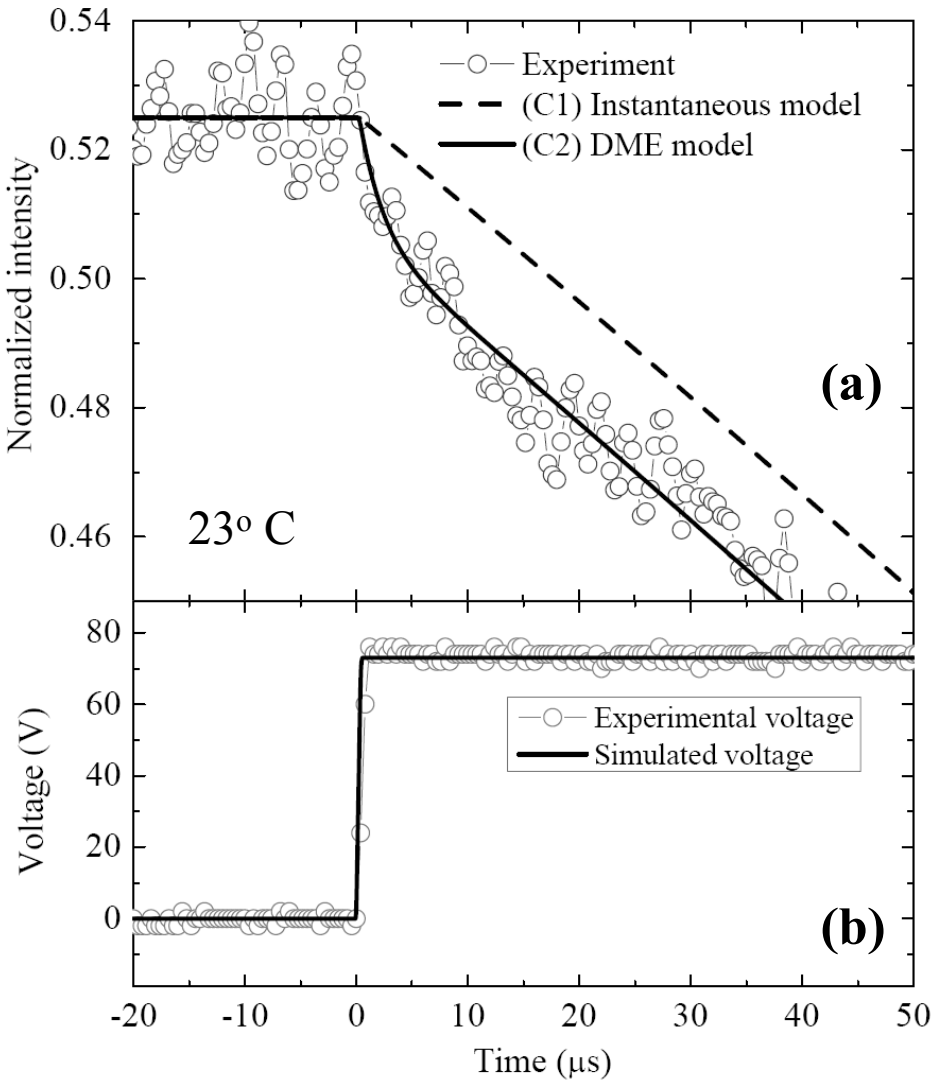

Figure 2.8. Normalized transmitted light intensity (a) and voltage (b) versus time for 53.7 wt. % MLC7026-100 + 46.3 wt. % MLC2048 mixture driven by fast-changing square pulses with a characteristic change time less than 1 μs. The circles are the experimental data; the curves represent simulations with different models as indicated by the labels.

Figure 2.8 demonstrates that the DME model (C2) explains the experimental data well, while the instantaneous model (C1) predicts a slower director reorientation

as compared to the experiment. The accelerated director reorientation seen in the experiment is the result of DME as the absolute value of $\Delta\varepsilon$ increases at higher frequencies and the sharp front of the pulse is perceived by the mixture as such a high-frequency excitation. In what follows, we present other demonstrations of how the DME speeds up the switching of the nematics with $\Delta\varepsilon < 0$.

(a) Sinusoidal versus rectangular modulation of pulses. The cell is driven by AC pulses at 10 kHz, but in the first experiment the voltage is modulated by a sinusoidal curve and in the second experiment it is modulated by a rectangular profile. The RMS value of the voltage was the same in both cases (40 V_{RMS}). The rectangular profile yields more efficient reorientation, Figure 2.9, as the sharp edges of the pulses lead to a larger $|\Delta\varepsilon|$. In contrast, the sinusoidal modulation tests only the low-frequency value of $|\Delta\varepsilon|$ that is only |–0.5| at 10 kHz, smaller than |–2.6| at higher frequencies, see Figure 2.7.

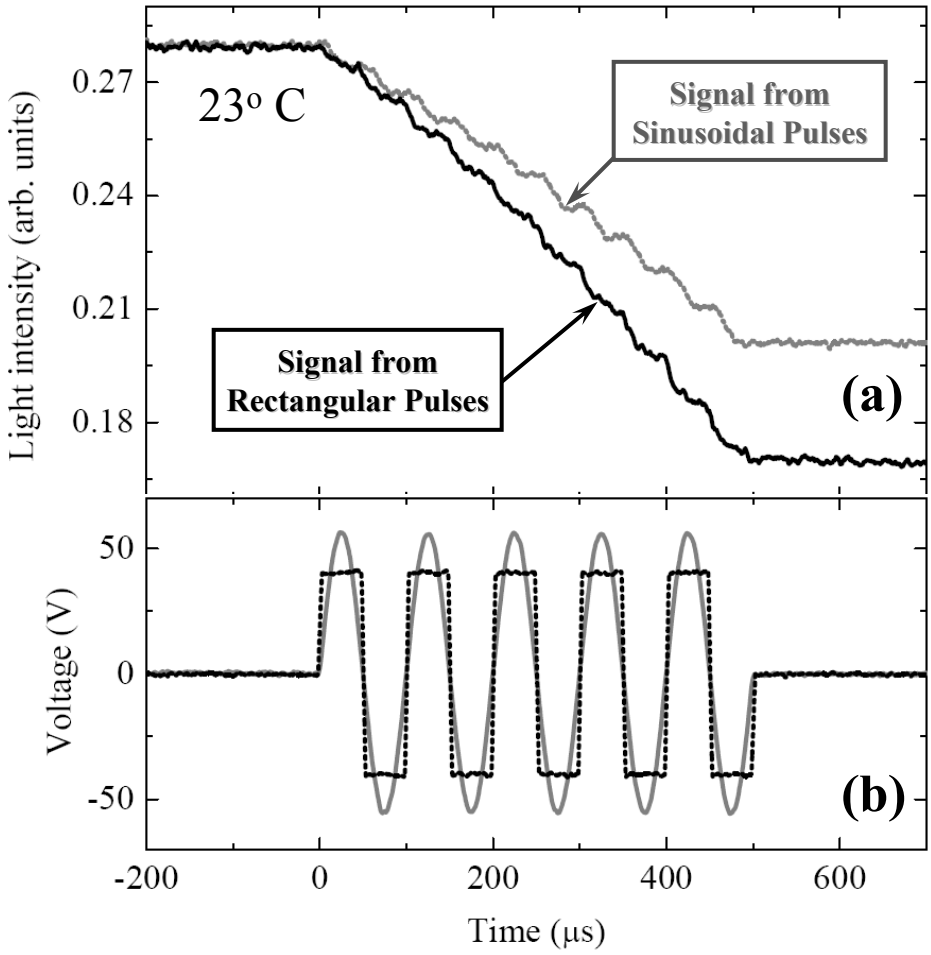

Figure 2.9. The transmitted light intensity curves (a) versus time when the cell filled with the 53.7 wt. % MLC7026-100 + 46.3 wt. % MLC2048 mixture, driven by a rectangular 10 kHz AC pulse with an amplitude of 40 V_{RMS} and a sinusoidal AC pulse in which the frequency is also 10 kHz and the amplitude is 40 V_{RMS} (b), respectively.

(b) Optimizing the driving pulse by increasing the number of sharp fronts. We used two different pulses. One was a single 150 μs duration DC pulse of the same polarity and the other was a signal of the same amplitude and of the same total duration, but with the polarity changed once, effectively corresponding to a higher

frequency. From the point of view of a conventional instantaneous model, the two driving schemes are equivalent; therefore there should be no difference in the response time. The experiment, Figure 2.10, shows that in fact the second pulse yields a faster reorientation. The additional sharp front in the second pulse tests the high-frequency values of $|\Delta\varepsilon|$ which are larger than $|\Delta\varepsilon|$ at low frequencies. Note that the fast switching achieved in the industrial cells with patterned vertical alignment (PVA) by using short rectangular pulses of high amplitude might be the result of not only the large amplitude of these "overshooting" signals but also of their short τ_U [42]. It would be certainly of interest to explore further the optimization of voltage pulses used in PVA mode by incorporating the DME into consideration.

We conclude the discussion with a note that the observed director dynamics in all systems (A), (B), and (C) cannot be attributed to the dielectric heating. The latter decreases the scalar order parameter and thus decreases the birefringence $n_e - n_o$. Therefore, the light intensity changes that might have been caused by heating would be of an opposite sign as compared to the observed DME-triggered changes. In addition, the characteristic rates of dielectric heating are too low ($< 0.1\,^{\circ}\mathrm{C}$/ms) [44] to influence the experimental data reported above in the ns and μs range.

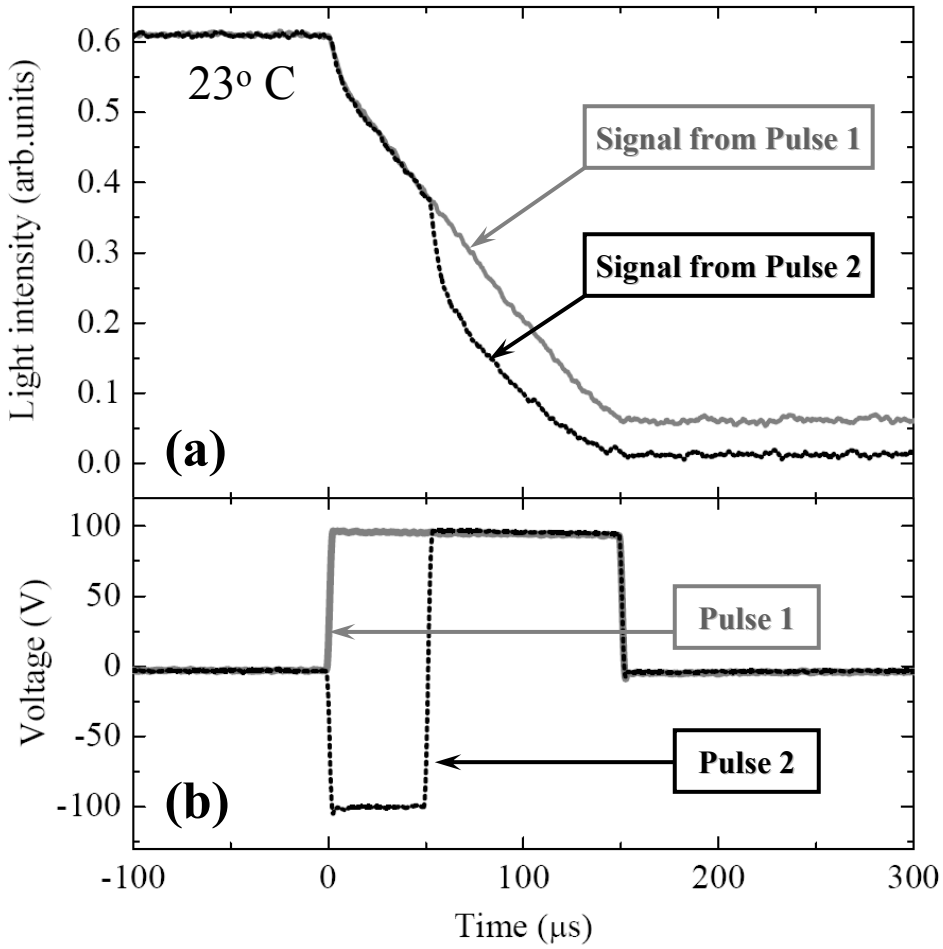

Figure 2.10. The transmitted light intensity curves versus time for the cell filled with the 53.7 wt. % MLC7026-100 + 46.3 wt. % MLC2048 mixture, driven by a DC pulse with a duration of 150 μs and an amplitude of 100 V, and a pulse with a total duration of 150 μs and amplitudes of +/- 100 V, with polarity changed once.

2.3 Summary

We presented a general model to describe the switching dynamics of uniaxial nematic LCs subject to a changing electric field. We demonstrate that when the characteristic time of voltage change is of the order or smaller than the dielectric

relaxation time, the director dynamics cannot be explained by the conventional dielectric response theory, in which the electric displacement is assumed to be an instantaneous function of the applied field. In the proposed model, we take into consideration that both parallel and perpendicular components of the dielectric permittivity tensor might experience relaxation and that there might be several relaxation processes. The dielectric torque density is determined by the entire frequency spectrum of the dielectric tensor $\boldsymbol{\varepsilon}(\omega)$, rather than by a particular value of the dielectric anisotropy $\Delta\varepsilon$ at any given frequency. In addition, the model takes into account that $\hat{\mathbf{n}}$ changes during the switching process.

The essence of the model is represented by Eq. (2.15) which expresses the dielectric torque on the director. Depending on the typical time τ_U with which the electric field is changing, any relaxation process would qualify either as "fast" (if its relaxation time is shorter than τ_U) or as "slow". The fast relaxations contribute to the "instantaneous" torque, the first term in Eq. (2.15). The slow relaxations contribute to one of the two "memory" integrals of Eq. (2.15), associated with either the parallel or the perpendicular component. The balance of "instantaneous" and "memory" contributions define the temporal behavior of the director, which in some cases is totally opposite to an intuitive picture presented by the standard model.

We used a number of different materials to verify and illustrate the applicability of the proposed model. As an example of the potentially "fastest" (with the highest relaxation frequencies) material with molecules carrying permanent dipoles, we used 5CB. We demonstrate that when the applied voltage changes on the scale of nanoseconds, the dielectric response of 5CB cannot be described by the

standard model but can be described by our model in which the dielectric torque is determined by the two spectral dependencies, $\varepsilon_{\parallel}(\omega)$ and $\varepsilon_{\perp}(\omega)$. A peculiar feature of this dependency on the entire spectra of $\varepsilon_{\parallel}(\omega)$ and $\varepsilon_{\perp}(\omega)$ is that the director might experience a "wrong" direction of reorientation, away from the field direction rather than towards it, within the first ~10 ns of the applied pulse. The reason is that the sharp front is perceived by the material as the high-frequency excitation at which $\Delta\varepsilon$ might have a value different from the static value and even be of the opposite sign.

In the second experimental system, a 5CB-MLC2048 mixture, we tested multiple relaxations in $\varepsilon_{\parallel}(\omega)$. Here the "wrong" sense of director reorientation at the beginning of the driving pulse is especially clear as the relaxation time of the mixture is relatively large, 6.0 μs, as compared to the rise time of the voltage we were able to produce in the laboratory. Finally, we presented the third situation, in which $\Delta\varepsilon$ is negative at low frequencies and becomes larger in the absolute value at high frequencies. Here the DME works to speed the switching up rather than to slow it down as in the dielectrically-positive materials such as 5CB.

The model developed in this work should be of interest in the development of fast-switching LC devices, in which the dielectric relaxation time is comparable to the voltage increase time. In the nematic materials with significant dipole moments, the slowest dielectric relaxation usually corresponds to the flip-flop of the longitudinal dipoles. As a result, in the dielectrically-positive materials, DME usually slows down the director response if the applied voltage changes too quickly; therefore, to achieve a faster response, one might need to reduce the rate of voltage changes[41]. In

contrast, in the negative materials, the DME speeds the response up when the voltage changes quickly.

Obviously, the DME effect should be also relevant to the electrooptic switching of other materials, such as smectics and biaxial nematics. The latter might represent an especially interesting subject for further studies, as the biaxial nematics offer a possibility of fast switching when the major director remains fixed and the minor director reorients around the major one.

Chapter 3

POLARITY-DEPENDENT DIELECTRIC TORQUE

We learn from Chapter 2, that the dielectric relaxation could significantly affect the director dynamics, thus it is necessary to investigate the director response speed when the dielectric relaxation is taken account. There are two phases in electric switching of a LC device. The fast "active" phase of "switch-on" is driven by an applied voltage U with the characteristic time $\tau_{on} \approx \gamma_1 d^2 / \left(\varepsilon_0 |\Delta\varepsilon| U^2 \right)$ (here ε_0 is the electric constant, d is the cell thickness, γ_1 is the rotational viscosity, $\Delta\varepsilon = \varepsilon_{\parallel} - \varepsilon_{\perp}$ is the dielectric anisotropy) [3]; τ_{on} can be decreased by increasing U. Director reorientation in the "switch off" phase is a "passive" process driven by relaxation of elastic distortions with switch-off time $\tau_{off} \approx \gamma_1 d^2 / \left(\pi^2 K \right)$ [3] that depends on the NLC properties such as γ_1 and the elastic constant K, but not on the (pre)applied electric field. This consideration is based on a classic picture of a NLC as a medium with no dielectric dispersion and instant dielectric response; the dielectric torque $\mathbf{M}_d = \varepsilon_0 \Delta\varepsilon \left(\mathbf{E} \cdot \hat{\mathbf{n}} \right) \mathbf{E} \times \hat{\mathbf{n}}$ is quadratic in $\mathbf{E}$ and is determined by the present values of $\mathbf{E}$ and $\hat{\mathbf{n}}$ [1]. Frequency dependence of dielectric permittivity changes this picture, as $\mathbf{M}_d$ becomes dependent not only on the present $\mathbf{E}$ and $\hat{\mathbf{n}}$, but also on their past

values [4, 5]. This "dielectric memory effect" (DME) has been studied for so-called dual frequency NLCs in which $\Delta\varepsilon$ changes sign with the frequency f [4, 5, 15]. In this chapter, we demonstrate a very unusual consequence of DME, namely, an existence of a "memory" dielectric torque that is *linear* (rather than quadratic) in the present electric field. The direction of the torque can be controlled by the polarity of electric field, regardless of the sign of $\Delta\varepsilon$. This feature allows one to design a situation when the "switch-off" phase can be accelerated by a properly chosen back edge of the electric pulse and is no longer a "passive" process [6].

3.1 Theory

Due to dielectric relaxation, electric displacement $\mathbf{D}(t)$ and the torque $\mathbf{M}_d(t) = \mathbf{D}(t) \times \mathbf{E}(t)$ depend on both the present $\mathbf{E}(t)$, and the past field $\mathbf{E}(t')$, $-\infty < t' \le t$ [4, 5]. Many NLCs experience only a single relaxation process at $f < 10$ MHz that can be described by the Debye model:

$$\varepsilon_{\parallel}(f) = \varepsilon_{h\parallel} + \frac{\varepsilon_{l\parallel} - \varepsilon_{h\parallel}}{1 - i2\pi f\tau}, \quad \varepsilon_{\perp}(f) = \varepsilon_{\perp} = const, \tag{3.1}$$

where "*l*" and "*h*" refer to the low and high f, τ is the dielectric relaxation time. We focus on two Debye type materials with different (but f independent) signs of $\Delta\varepsilon$ with dielectric relaxation in the kHz region convenient for experimental studies (although the consideration is applicable for other parts of the spectrum). The negative $\Delta\varepsilon < 0$ NLC was obtained by mixing 60.6 wt % MLC-7026-100 (EM Industries) and 39.4 wt % 2F-3333 (Rolic Technologies); the positive $\Delta\varepsilon > 0$ NLC

was a mixture of 20.0 wt % of pentylcyanobiphenyl (5CB, EM Industries) and 80.0 wt % 2F-3333, Figure 3.1. The dielectric permittivities were measured using Schlumberger 1260 impedance/gain-phase analyzer.

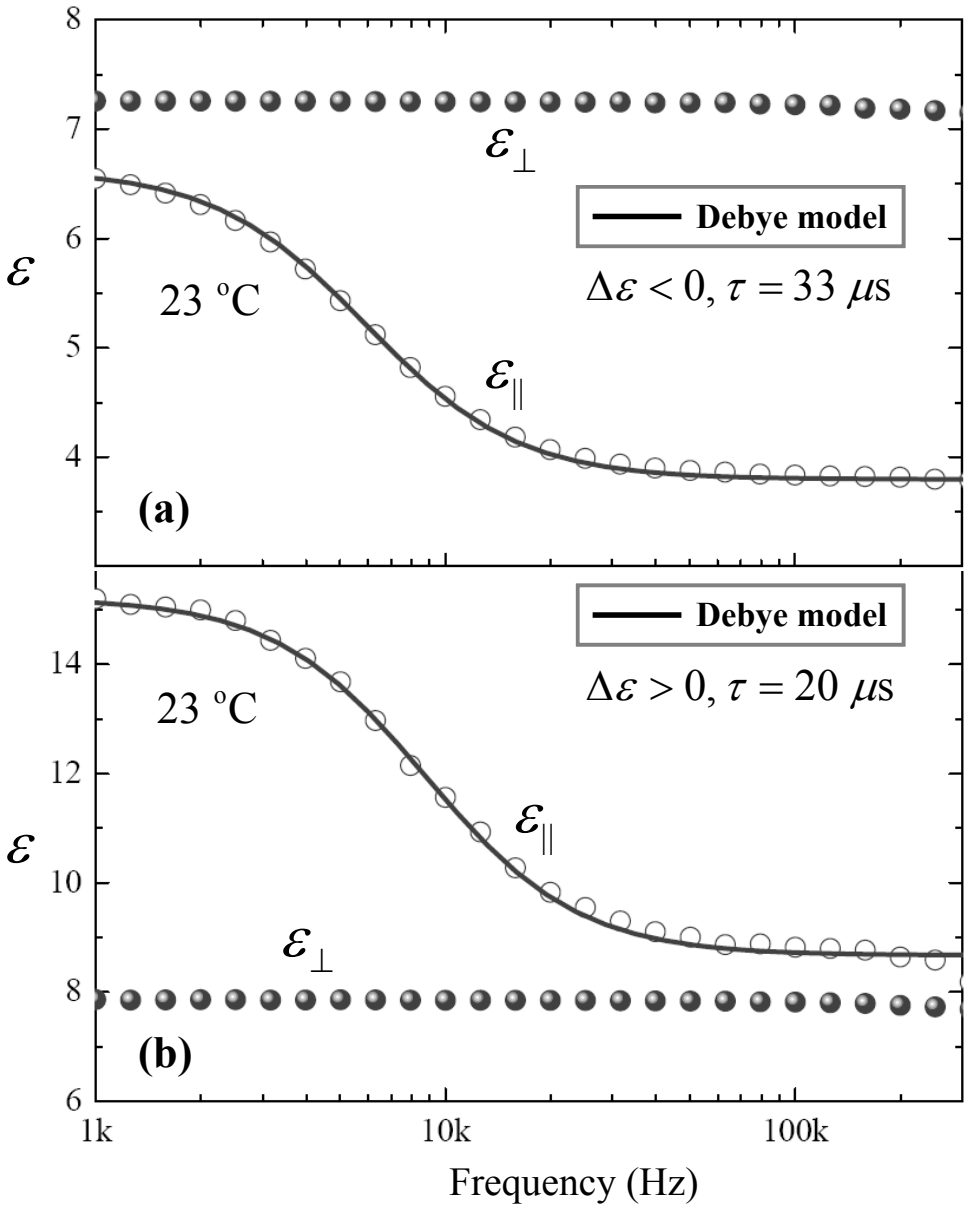

Figure 3.1. The dielectric dispersion curves of two NLCs, with $\Delta\varepsilon < 0$ (a) and $\Delta\varepsilon > 0$ (b). The data for $\varepsilon_{\parallel}$ are fitted by Eq. (3.1) with $\varepsilon_{l\parallel} = 6.60$, $\varepsilon_{h\parallel} = 3.91$, $\varepsilon_{\perp} = 7.31$ and $\tau = 33\ \mu s$ (a); $\varepsilon_{l\parallel} = 15.21$, $\varepsilon_{h\parallel} = 8.67$, $\varepsilon_{\perp} = 7.88$ and $\tau = 20\ \mu s$ (b).

The director dynamics is determined by the balance of the dielectric $\mathbf{M}_d$, viscous $\mathbf{M}_v$, and elastic $\mathbf{M}_e$ torques through the Ericksen-Leslie equation $\mathbf{M}_d + \mathbf{M}_v + \mathbf{M}_e = 0$. For a flat cell with plates along the *x*-*y* plane, $\mathbf{E}(t) = E_z(t)\hat{\mathbf{z}}$, $\hat{\mathbf{n}}(t)$ in the *x*-*z* plane depending only on *z*, the only non-zero components of torques are along the y-axis. The dielectric torque is [4]:

$$M_d(t) = \varepsilon_0 E(t)\sin\theta(t)\left[\Delta\varepsilon_h E(t)\cos\theta(t) + \frac{\varepsilon_{l\|} - \varepsilon_{h\|}}{\tau}\int_{-\infty}^{t}\exp\left(-\frac{t-t'}{\tau}\right)E(t')\cos\theta(t')\,dt'\right] \quad (3.2)$$

where $\theta(t)$ is the angle between $\hat{\mathbf{n}}(t)$ and $\mathbf{E}(t)$. For $\varepsilon_{l\|} = \varepsilon_{h\|} = \varepsilon_{\|}$, Eq. (3.2) recovers the classic "instantaneous" dielectric response theory.

Consider the torque balance in response to a voltage changes over a short time interval between $t = 0$ and $t \sim \tau$. This interval is short enough to assume the changes of $\theta(t)$ small. This allows us to approximate as time independent the following three quantities: (a) M_d with $\theta(z,t) \approx \theta(z, t=0) = \theta_0(z)$ (provided $\theta_0(z) \neq 0, \pi/2$), (b) the elastic torque $M_e(z,t) = M_e(z)$ and (c) the spatial non-uniformity of the electric field, $E_z(z,t) = g(z)U(t)$, where $g(z)$ is a proportionality factor. We neglect the back-flow effect, thus $M_v(t) = \gamma_1 d\theta(t)/dt$. Under these assumptions, the solution of Ericksen-Leslie equation $\gamma_1 d\theta(t)/dt = -M_d - M_e$ that describes the time evolution of the system, is $\theta(t) = \theta_0(z) - \Theta(z)Q + M_e(z)t$, where

$$\Theta(z) = \varepsilon_0\left(\varepsilon_{l\|} - \varepsilon_{h\|}\right)\tau U_0^2 g^2(z)\sin 2\theta_0(z)/\gamma_1 \quad (3.3)$$

and Q is the normalized integrated dielectric torque:

$$Q=\tau^{-1}\int_0^t\left\{\xi\,u^2\left(t'\right)+u\left(t'\right)\left\{u_{mem}\exp\left(-t'/\tau\right)+\tau^{-1}\int_0^{t'}\exp\left[-\left(t'-t''\right)/\tau\right)\right]u\left(t''\right)dt''\right\}\right\}dt'. \tag{3.4}$$

Here $\xi=\left(\varepsilon_{h\|}-\varepsilon_{\perp}\right)/\left(\varepsilon_{l\|}-\varepsilon_{h\|}\right)$, $u\left(t\right)=U\left(t\right)/U_0$ is the normalized voltage with $U_0=U\left(t\to 0^-\right)$ being the voltage that acts just before the "switch-off" moment $t=0$, $u_{mem}=\tau^{-1}\int_{-\infty}^{0}\exp\left(t'/\tau\right)u\left(t'\right)dt'$ is the memory term caused by the "past" field.

To optimize Q, we apply a direct variational method. Integrating Eq. (3.4) with a decaying exponential probe function $u(t)=a\,\mathrm{Exp}\left(-\Gamma t/\tau\right)$, where a and $\Gamma>0$ are two variational parameters, one obtains:

$$Q=\frac{a\left[2u_{mem}\Gamma+a\left(1+\xi+\xi\Gamma\right)\right]}{2\Gamma\left(1+\Gamma\right)}-\frac{a^2\left(1+\xi-\xi\Gamma\right)}{2\Gamma\left(\Gamma-1\right)}\mathrm{e}^{-2\Gamma t/\tau}+\frac{a\left[u_{mem}\left(\Gamma-1\right)+a\right]}{\Gamma^2-1}\mathrm{e}^{-(1+\Gamma)t/\tau}. \tag{3.5}$$

The last expression will be used to fit the data below. It is instructive to qualitatively discuss the basic feature of Eq. (3.5). The first term dominates for large $t>5\tau$ and determines the saturated value of Q. Its extremum $Q_e=u_{mem}^2\left\{\left[\left(1+\xi\right)\xi\right]^{1/2}-\xi-1/2\right\}$ is reached for $\Gamma_e=\left(1+\xi^{-1}\right)^{1/2}$ and $a_e=u_{mem}\left(1-\Gamma_e\right)$. It is easy to see that $Q_e<0$ for the positive NLCs in which $\xi>0$, while $Q_e>0$ for the negative NLCs in which $\xi<-1$. The Q_e is opposite in sign to the dielectric torque in the switch on phase, thus it can accelerate the director relaxation in the switch-off phase.

The theory can be qualitatively explained as follows. Consider first a NLC with $\Delta\varepsilon > 0$ in a planar cell. A positive dc field $E_z > 0$ reorients $\hat{\mathbf{n}}$ towards the z-axis. E_z also induces a dipole moment density $\mathbf{p}$ with the components $p_\perp = \varepsilon_0 (\varepsilon_\perp - 1) E_z \sin\theta$ and $p_{||} = \varepsilon_0 \left(\varepsilon_{h||} - 1\right) E_z \cos\theta + p_{mem}$, perpendicular and parallel to $\hat{\mathbf{n}}$, respectively. Here $p_{mem} \propto u_{mem}$ is the "memory" contribution that saturates to the value $p_{mem} = \varepsilon_0 \left(\varepsilon_{l||} - \varepsilon_{h||}\right) E_z \cos\theta$ after the dc field E_z acted for a sufficiently long time $> \tau$ ($u_{mem} \to 1$). Note that $p_{mem} > 0$ and $E_z > 0$ are of the same sign. When the field is switched off at $t = 0$, $p_{mem} > 0$ does not disappear instantaneously, but decays with a characteristic time τ. If within the interval $0 < t \le \tau$, one applies a new electric pulse of *the opposite polarity*, then this field $E_z < 0$ would interact with the decaying $p_{mem} > 0$ to assist the reorientation towards the planar state, $\theta \to \pi/2$.

In the homeotropic cell with a negative NLC, the field $E_z > 0$ at $t < 0$ also induces $p_{mem} > 0$ (of the same polarity). If within the interval $0 \le t \le \tau$ one applies a new voltage pulse of *the same* polarity, $E_z > 0$, then this field will couple to $p_{mem} > 0$ to assist the director reorientation into the homeotropic state, $\theta \to 0$.

If the NLC were not dispersive, any field-induced polarization would relax instantaneously, $p_{mem} = 0$, $\varepsilon_{l||} = \varepsilon_{h||}$ and $\tau = 0$, and the effect would not be observed. Therefore, the classic theory with an instantaneous dielectric response cannot predict the phenomenon we describe. Below we present experimental verifications of the effect.

3.2 Experimental results and discussions

We used homeotropic and planar (with a small pretilt of $\sim 1^{o}$) cells (EHC Ltd.) composed of glass substrates with indium tin oxide electrodes of area $10\times 10\ \mathrm{mm}^2$; $d = 14.4\ \mu\mathrm{m}$ for the homeotropic cell and $d = 20.6\ \mu\mathrm{m}$ for the planar cell. The field-induced director dynamics was monitored by measuring the He-Ne laser ($\lambda = 633\ \mathrm{nm}$) light transmission $I(t) = A\sin^2(\Phi/2)$ through the cells placed between two crossed polarizers [11]. The phase retardation Φ depends on θ; for small variations of θ, the retardation change is linear in Q, $\Phi - \Phi_0 \approx \rho Q$, where

$$\Phi_0 = \frac{2\pi n_o}{\lambda}\int_0^d \left\{\frac{n_e}{\tilde{n}(z)} - 1\right\} dz\,,\ \rho = \frac{\pi n_o n_e\left(n_e^2 - n_o^2\right)}{\lambda}\int_0^d \frac{\Theta(z)\sin 2\theta_0(z)}{\tilde{n}(z)^3}\,dz\,, \qquad (3.6)$$

and $\tilde{n}(z) = \left[n_e^2\sin^2\theta_0(z) + n_o^2\cos^2\theta_0(z)\right]^{1/2}$. The coefficient A is close to the intensity I_0 of the impinging light for the planar cell when the rubbing direction is at 45^{o} with respect to the polarizers [11]. In the homeotropic cell, $A \approx I_0/2$ because the applied field creates random azimuthal orientation of $\hat{\mathbf{n}}$ with numerous umbilics, 10-100 within the area probed by the beam. The umbilics are pairs of point defects-boojums at the opposite plates, which are caused by degeneracy of the director tilt [45], as confirmed by the Fluorescence Confocal Polarized Microscope (FCPM) [46] image, Figure 3.2 [43]. The umbilics defects randomize the director field in the plane of the cell thus assuring reproducibility of the experiment. The umbilics relax much slower (seconds and minutes [43]) than the duration of our experiments (< 0.5 ms).

We used TIA-500S-TS photodetector (Terahertz Technologies) and Tektronix TDS 210 oscilloscope to measure $I(t)$.

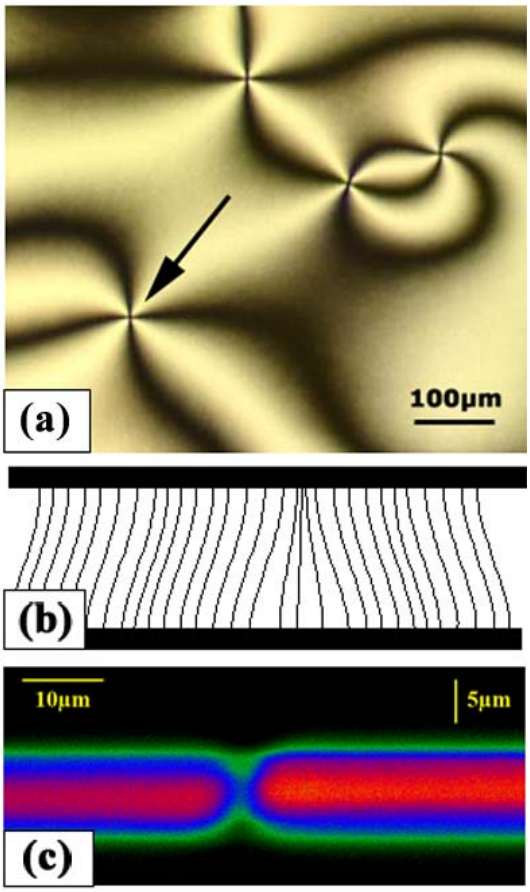

Figure 3.2. Umbilics defects: (a) a polarizing microscope texture, (b) director configuration of a cell with non-rubbed azimuthally-degenerated homeotropic alignment and (c) a FCPM image of the vertical cross-section.

The driving pulses were produced by WFG500 wave-form generator (FLC Electronics); the maximum rate was 240 $V/\mu s$. To test the switch-off dynamics, we used two different profiles for the pulse's back edge: (i) an instantaneous back edge (in practice $\sim 1\,\mu s$ in duration because of the finite voltage change rate); (e) an exponentially decaying back edge $u(t) = a\,\mathrm{Exp}\left(-\Gamma t/\tau\right)$.

To drive the homeotropic cell with a negative NLC, we first apply a square 100 V dc pulse of duration 225 μs, much longer than $\tau = 33\ \mu$s, Figure 3.1(a), so that there is enough time to produce the saturated "memory" dipole moment ($u_{mem} \to 1$). This pulse is switched off by an instantaneous back edge (i) or by three different exponential edges with $\Gamma = 0.45$ and: (e1) positive polarity, $a = 0.5$; (e2) $a = 0.87$; (e3) negative polarity, $a = -0.5$; Figure 3.3. The optical response is different in all four cases. In the case (i), $\hat{\mathbf{n}}$ reorients slowly toward the homeotropic state $\theta \to 0$, as evidenced by the decrease in $I(t)$ in Figure 3.3 inset. The pulse (e1) produces much faster reorientation (r-e1), despite the fact that U decreases less abruptly as in case (i). The shape of the pulse (e1) is close to the optimum, as any departure from the pre-selected $a = 0.5$ and $\Gamma = 0.45$ causes a slower or even a non-monotonous response, as in (e2) case. The linear $\mathbf{E}$-dependence of the "memory" torque is well illustrated by the response to pulses (e1) and (e3) that are identical in amplitude and duration and differ only in polarity: (e1) drives $\hat{\mathbf{n}}$ toward $\theta = 0$ while (e3) continues to drive $\hat{\mathbf{n}}$ toward $\theta = \pi/2$. After a sufficiently long time, the NLC relaxes to the same homeotropic state with $I = 0$ for all pulses, Figure 3.3.

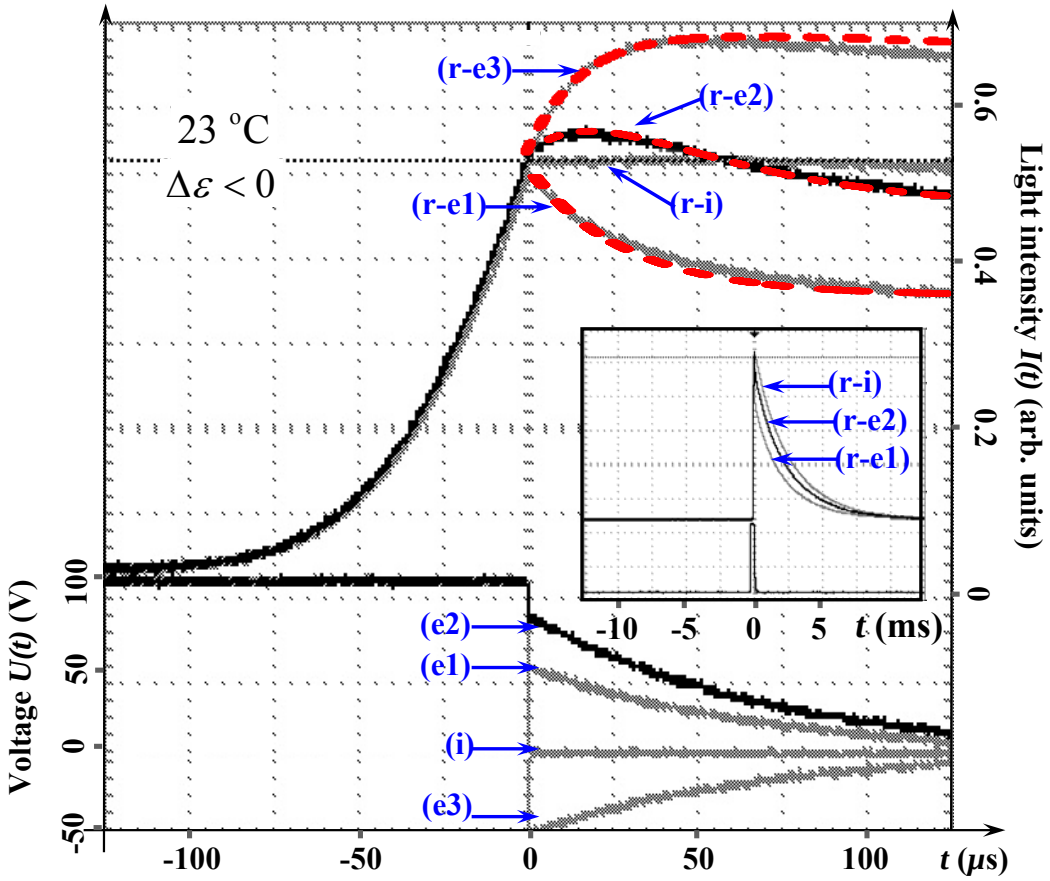

Figure 3.3. Electrooptic response $I(t)$ of a $\Delta\varepsilon < 0$ NLC in a homeotropic cell driven by dc pulses with an instantaneous (i) and exponentially decaying back edges (e1-e3); "r" stands for "response". The dashed lines show $I(t)$ simulated using Eqs. (3.5) and (3.6). The inset shows $I(t)$ over a large time scale.

The different scenarios can be fitted by the model above. To fit the data, we used the approximation $\Phi - \Phi_0 \approx \rho Q(t)$, Eq. (3.6); the only fitting parameter is ρ, as $Q(t)$ is determined by the experimental values of a and Γ, Eq. (3.5). We first fit the response curve (r-e1) using $a = 0.5$, $\tau = 33\ \mu$s and $\Gamma = 0.45$ and find $\rho = 2.33$. With this value of ρ, and with the experimental τ, a and Γ, the model (4)

reproduces the measured curves (r-e2) and (r-e3) very well with no fitting parameters, Figure 3.3.

For the planar cell with the positive NLC, we used a 100 V dc pulse of duration 310 μs, Figure 3.4(a). The back edge was either (i) instantaneous or (e) exponential $u(t) = a\,\mathrm{Exp}\left(-\Gamma t/\tau\right)$, with $a = -1$, $\tau = 20$ μs and two different decaying speeds, $\Gamma = 2$ (e1) and $\Gamma = 0.75$ (e2). A properly timed exponential "tail" (e1) produces the fastest optical response (r-e1). However, all the optical responses curves in Figure 3.4(a) share one common feature that prevents a direct comparison with the theory: a universal (independent of the details of the back edge) decay, with a characteristic time 0.5 ms that is much shorter than the elastic relaxation time, $\tau_{off} \approx 0.4$ s for a typical $\gamma_1 \sim 0.1$ kg m $^{-1}$s^{-1} [11], but is close to the characteristic times of the back-flow effects [47], i.e. coupling of the director reorientation and mass flow [1, 3, 11]. The other possible reason, ionic currents, does not seem plausible, because the 0.5 ms universal decay behavior does not change when we replace the dc pulse with two subsequent pulses of opposite polarities and half duration.

Although we do not know the precise mechanism behind the universal decay and can only tentatively attribute it to the backflow, we have found empirically that this decay can be reduced while preserving the value of phase retardation at which the switch-off starts. This reduction is achieved by modifying the "switch-on" pulse, namely, by applying first a long (180 ms) low amplitude (5 V) ac pulse followed by a shorter dc pulse (120 μs instead of 310 μs, still longer than $\tau = 20$ μs), Figure 3.4(b). Backflow dynamics depends on the combination of NLC viscosities,

$B = \alpha_3 \sin^2\theta - \alpha_2 \cos^2\theta$, where $\alpha_3 / \alpha_2 \sim 10^{-2}$ for typical LC [3]. The ac pulse pretilts $\hat{\mathbf{n}}$ from the planar orientation $\theta \approx \pi/2$, thus stabilizing the sign of B during the action of the dc pulse. In addition, this pretilt reduces the needed angle of director reorientation during the dc pulse, the latter thus can be shorter than in the experiment in Figure 3.4(b), but still long enough to produce p_{mem}. The empirically found regime in Figure 3.4(b) allows us to try to describe the experimental data with the model derived in the backflow-free approximation, Eq. (3.4). The difference in response to pulses (i), (e1) and (e2) in Figure 3.4(b) is very pronounced: (e1) produces a faster reorientation as compared to (i), while pulse (e2) results in a non-monotonous behavior. Moreover, response curves (r-e1) and (r-e2) in Figure 3.4(b) are well fitted with Eq. (3.5) as explained above (in the backflow-free approximation), using the experimental a, $\tau = 20\ \mu$s, and Γ and the single fitting parameter $\rho = 0.496$.

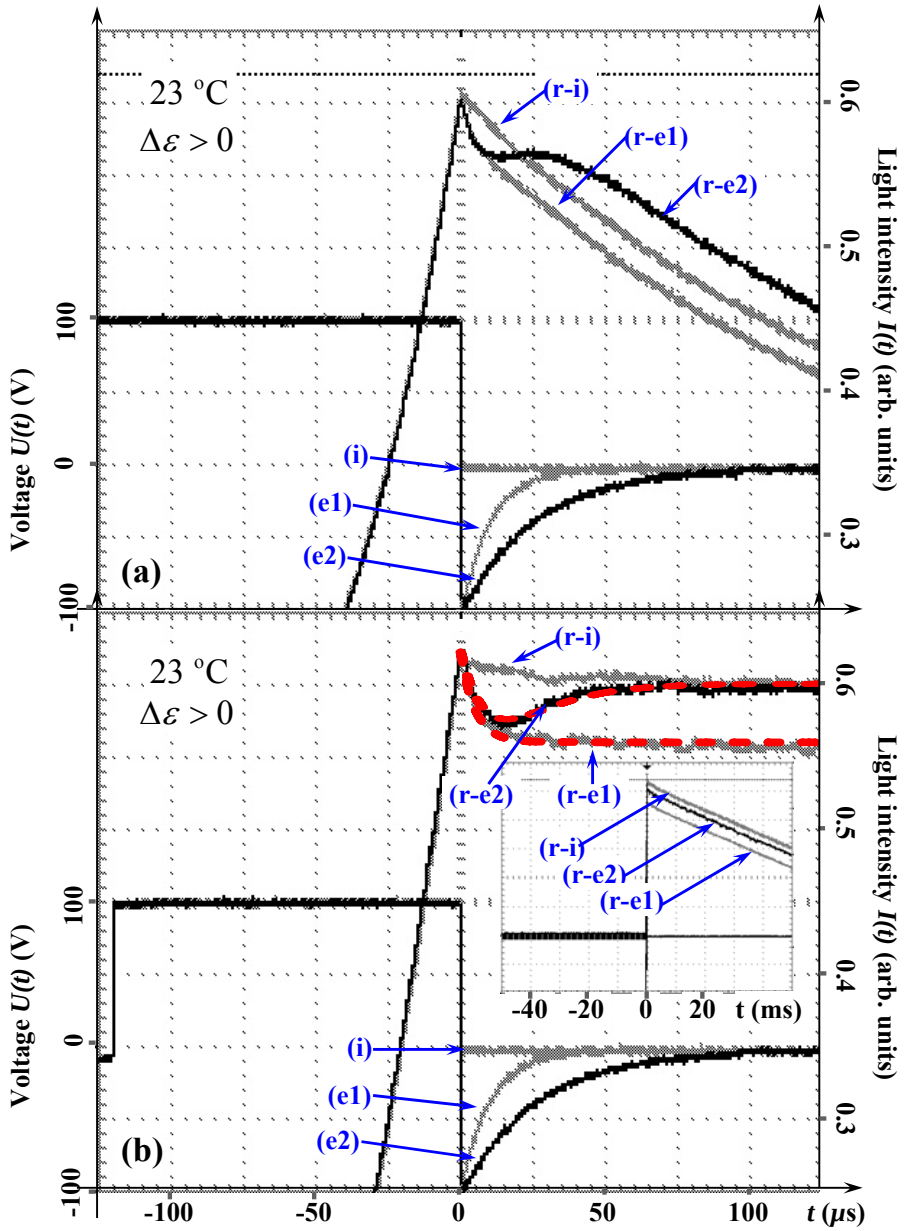

Figure 3.4. Electrooptic response $I(t)$ of a $\Delta\varepsilon > 0$ NLC in a planar cell driven by dc pulses with an instantaneous (i) and exponentially decaying back edges (e1, e2). (a) The cell is driven by a dc pulse of duration 310 μs; (b) the cell is driven by a 5 V, 1 kHz ac pulse of duration 180 ms, followed by a dc pulse of duration 120 μs; the inset shows a larger time scale. The dashed lines show $I(t)$ simulated using Eqs. (3.5) and (3.6).

We further performed control experiments with a planar cell filled with 5CB, in which $\varepsilon_{\parallel}$ experiences relaxation with $\tau \approx 50$ ns [25]. Such a short τ should not cause a DME if the typical time of voltage changes is 1 μs. Indeed, as shown in Figure 3.5, two (e)-pulses with the same amplitude $|a| = 1$ and duration $\tau / \Gamma = 10$ μs, but of *opposite* polarity, produce *the same* positive torque. This feature is observed regardless of whether the cell is addressed by a dc pulse only or is additionally pre-addressed with an ac pulses, Figure 3.5(b), or not, Figure 3.5(a). Such a behavior is consistent with the non-dispersive character of 5CB in the kHz range and with the classic instantaneous model with dielectric torque quadratic in **E**; it is clearly different from the behavior of a dispersive NLC that is sensitive to the polarity of the driving pulses, Figure 3.3.

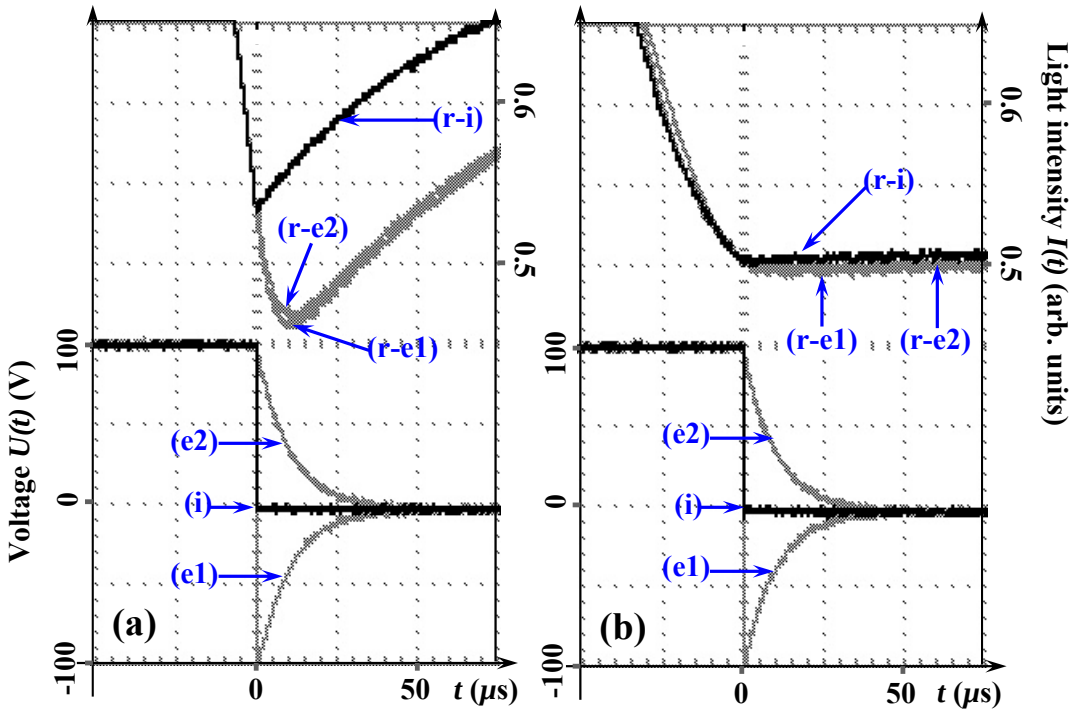

Figure 3.5. Electrooptic response $I(t)$ of 5CB in a planar cell driven by dc pulses with an instantaneous (i) and exponentially decay back edges (e1, e2) of opposite polarity. (a) The cell is driven by a dc pulse of duration 121 μs ; (b) the cell is driven by a 5 V, 1 kHz ac pulse of duration 180 ms (not shown), followed by a dc pulse of duration 80 μs .

3.3 Summary

Theory and experiments above demonstrate that dielectric response in a NLC with dielectric dispersion might be sensitive to the polarity of the applied voltage. The effect is caused by a special "memory" term in the dielectric torque $\mathbf{M}_d(t)$ that is linear in the present field $\mathbf{E}(t)$, in contrast to a regular contribution that is quadratic

in $\mathbf{E}(t)$. This feature opens new possibilities for optimization of electro-optical effects in NLCs. For example, we demonstrated that the "switch-off" phase of director reorientation can be accelerated by exponentially decaying short pulses of a proper polarity with the duration determined by τ. Linear in $\mathbf{E}(t)$ character of the "memory" dielectric torque in a dispersive NLC offers a possibility of interplay with other field effects, such as flexoelectricity, order electricity, surface polarization, etc. In other words, the observed polarization-sensitive dielectric response of the NLCs opens perspectives for both applied and basic research.

Chapter 4

DISPERSION IMPOSED SWITCHING LIMITATION AND PULSE OPTIMIZATION

As we discussed in Chapter 3, the switch-off phase can be accelerated by utilizing the polarity dependent torque, yet the switch-on phase still poses as a problem since the dielectric dispersion leads to an undesired time delay or even an opposite rotation for the director reorientation dynamics in the dielectrically positive materials. In this chapter, we develop a model to optimize the shape of voltage pulses to improve the efficiency of switching. One of the counter-intuitive results is that a faster director reorientation can be achieved with a slower rather than faster rate of voltage increase.

4.1 Theory

When the characteristic time of the voltage change τ_U is close to or smaller than the NLC's dielectric relaxation time τ, the director dynamics can no longer be explained by the standard "instantaneous" dielectric response theory [1, 3], in which the dielectric displacement $\mathbf{D}(t)$ only depends on the current electric field $\mathbf{E}(t)$ acting at the same moment of time t. Because the components of the dielectric tensor experience dispersion and change as the voltage frequency f changes, $\mathbf{D}(t)$ depends not only on the current $\mathbf{E}(t)$, but also on its prehistory $\mathbf{E}(t')$, $-\infty < t' \le t$. The dielectric torque $\mathbf{M}(t) = \mathbf{D}(t) \times \mathbf{E}(t)$ acting to reorient the director $\hat{\mathbf{n}}$ is determined by the entire frequency spectrum of the dielectric tensor rather than by the static values of its components at low f. Dielectric dispersion in many LC materials can be described by the Debye relaxation model [14]:

$$\varepsilon_{\parallel}(\omega) = \varepsilon_{h\parallel} + \frac{\varepsilon_{l\parallel} - \varepsilon_{h\parallel}}{1 - i\omega\tau_{\parallel}}, \quad \varepsilon_{\perp}(\omega) = \varepsilon_{h\perp} + \frac{\varepsilon_{l\perp} - \varepsilon_{h\perp}}{1 - i\omega\tau_{\perp}}, \tag{4.1}$$

where the subscripts l and h refer to the low and high f, $\tau_{\parallel}$ and $\tau_{\perp}$ are the dielectric relaxation times of the dielectric components $\varepsilon_{\parallel}$ and $\varepsilon_{\perp}$ measured parallel and perpendicular to $\hat{\mathbf{n}}$, respectively. Note that we use two notations for frequency, the cyclic frequency f and the angular frequency ω related in a standard way, $f = \omega / 2\pi$. Figure 4.1 shows a typical example of the Debye relaxation for the nematic mixture 2F-3333 (Rolic Technologies) at 20^{o} C, as measured in our laboratory by using the Schlumberger 1260 impedance/gain-phase Analyzer. The dielectric dispersion for $\varepsilon_{\parallel}$ can be well fitted

by Eq. (4.1), solid curve in Figure 4.1. In the observed frequency range, there is no dielectric relaxation for $\varepsilon_{\perp}$, thus $\varepsilon_{l\perp} = \varepsilon_{h\perp} = \varepsilon_{\perp}$.

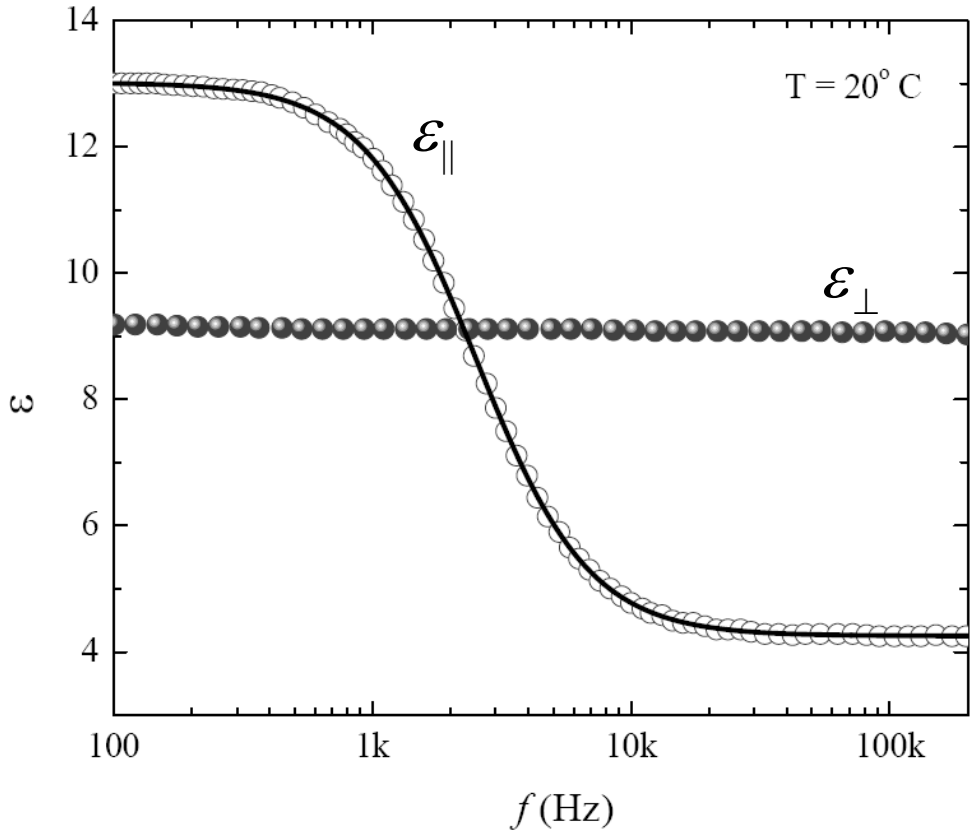

Figure 4.1. Dielectric dispersion curves of 2F-3333 at 20^{o} C. The solid curve is fitted with the Debye model, Eq. (4.1), with parameters $\varepsilon_{l\|} = 13.0$, $\varepsilon_{h\|} = 4.2$, $\varepsilon_{\perp} = 9.1$ and $\tau_{\|} = 69\ \mu s$.

When a LC material with the Deybe type relaxation, such as 2F-3333, is subject to an electric field $\mathbf{E}$, Figure 4.2, the dielectric torque acting on $\hat{\mathbf{n}}$ is given by [4]

$$M_d(z,t) = \varepsilon_0 E_0^2 e^2(t) * \sin\theta(z,t)\left[(\varepsilon_{h\|} - \varepsilon_{\perp})\cos\theta(z,t) + \frac{\varepsilon_{l\|} - \varepsilon_{h\|}}{\tau \cdot e(t)}\int_{-\infty}^{t} \exp\left(-\frac{t-t'}{\tau}\right) e(t')\cos\theta(z,t')dt'\right], \quad (4.2)$$

where E_0 denotes the maximum amplitude of $\mathbf{E} = E_0 * e(t)\hat{z}$, $e(t)$ is the normalized electric field, $e(t) \le 1$; $\theta(z,t)$ is the angle between $\hat{\mathbf{n}}$ and $\mathbf{E}$ at position z; ε_0 is the vacuum dielectric permittivity and $\tau = \tau_{||}$.

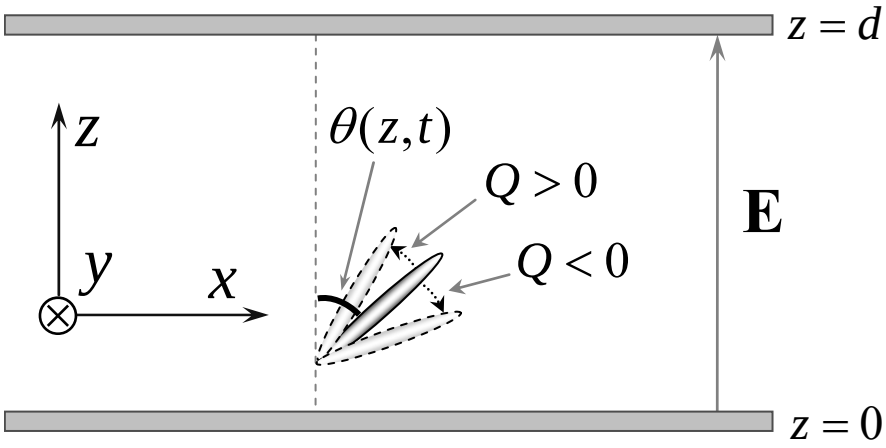

Figure 4.2. Liquid crystals confined between two electrodes at $z = 0$ and $z = d$. The direction of electric field $\mathbf{E}$ is along z axis. Q is the normalized integrated torque.

In the standard "instantaneous" model, the dielectric torque is written in a form different from Eq. (3.2), as the frequency dependence of $\varepsilon_{||}$ is neglected [1]:

$$M_i(z,t) = \varepsilon_0 E_0^2 e^2(t)(\varepsilon_{l||} - \varepsilon_\perp)\sin\theta(z,t)\cos\theta(z,t), \tag{4.3}$$

where the value of $\Delta\varepsilon = \varepsilon_{l||} - \varepsilon_\perp$ is measured at low f. The standard model predicts that M_i is always positive for all low f driving pulses. This prediction is not valid because the sharp rising front is perceived by the LC as a high-frequency excitation for which $\Delta\varepsilon < 0$. The latter effect is accounted for in Eq. (3.2). The director dynamics is determined by the competition between the first "instantaneous" term in Eq. (3.2), determined by the value of $\Delta\varepsilon$ at high f, and the second "memory" term which is

always positive. Equation (3.2) is applicable to the regular cell geometry when the electrodes at $z = 0$ and $z = d$ represent *x*-*y* plane, and also to the configuration when the electrodes are lines oriented along the *x* axis as in the case of In-Plane-Switching (IPS) mode, one of the most popular modes in the LCD industry [48].

According to the standard "instantaneous" model, Eq. (4.3), M_i is maximum when $e(t) \equiv 1$; –i.e. the square pulse is the best pulse to maximize the director rotation angle within a fixed time interval. When the dielectric dispersion is considered, M_d is not necessary maximum for the square pulse because the "instantaneous" and "memory" terms in Eq. (3.2) might be of different values and even of opposite signs. Below, we explore the optimized shape for the non-square pulse which would give a maximum value of M_d. In this work, the goal of optimization is to maximize the total director rotation angle within a fixed time interval; –i.e., the pulse duration T. Depending on practical needs, other criteria of optimization can be selected as well.

We first derive the total director rotation angle, $\Delta\theta = \theta(z, 0) - \theta(z, T)$, for a pulse shape $e(t)$ by solving Erickson-Leslie equation, then use Euler-Lagrange equation to find the best pulse shape which gives the extremum of the rotation angle within the time interval.

With Eq. (3.2), we write the Erickson-Leslie equation for the director dynamics:

$$-\gamma_1 \frac{\partial\theta(z,t)}{\partial t} = M_d(z,t) = \varepsilon_0 \sin\theta(z,t) E_0^2 e^2(t) * \left[(\varepsilon_{h\|} - \varepsilon_\perp)\cos\theta(z,t) + \frac{\varepsilon_{l\|} - \varepsilon_{h\|}}{\tau \cdot e(t)} \int_{-\infty}^{t} \exp\left(-\frac{t-t'}{\tau}\right) e(t')\cos\theta(z,t')dt' \right], \quad (4.4)$$

where γ_1 is the rotational viscosity. The solution to Eq. (4.4) which describes the total rotation angle $\Delta\theta$ of $\hat{\mathbf{n}}$ at a position z within a time interval T is

$$\Delta\theta = \theta(z,0) - \theta(z,T) = \frac{1}{2}\sin 2\theta(z,0) * \varsigma * Q\,, \tag{4.5}$$

under an assumption of a smallness of reorientation angle: $|\Delta\theta| = |\theta(z,0) - \theta(z,t)| < 10^{o}$, for any t within the interval $[0, T]$. This assumption also implies

$$\cos\theta(z,t) \cong \cos\theta(z,0)\,,\ \sin\theta(z,t) \cong \sin\theta(z,0)\,, \tag{4.6}$$

where $t = 0$ is the time moment at which the voltage pulse starts rising.

In Eq. (4.5), $\Delta\theta$ is determined by two parameters: the power factor

$$\varsigma = \frac{\tau}{\gamma_1}\varepsilon_0 E_0{}^2(\varepsilon_\perp - \varepsilon_{h\|})\,, \tag{4.7}$$

and the normalized integrated torque:

$$Q(T) = \frac{1}{\tau}\int_0^T \left[\frac{G^2+1}{\tau}e(t)\int_0^t \exp\left(-\frac{t-t'}{\tau}\right)e(t')dt' - e^2(t)\right]dt\,, \tag{4.8}$$

where $G = \sqrt{(\varepsilon_{l\|} - \varepsilon_\perp)/(\varepsilon_\perp - \varepsilon_{h\|})}$.

According to Eq. (4.5), $\Delta\theta$ is linearly proportional to ς. The power factor ς is positive for many materials with dielectric relaxation, such as pentylcyanobiphenyl (5CB) and 2F-3333 dual frequency mixture used in this work. The amplitude of ς is mainly determined by E_0 and γ_1: $\varsigma \propto E_0^2$ and $\varsigma \propto 1/\gamma_1$. To maximize the director rotation angle within a fixed time interval, a large E_0 and a small γ_1 are preferred.

The dependence of $\Delta\theta$ on the variables defining the normalized integrated torque Q, Eq. (4.8), is more complicated, and Q needs to be optimized.

If $Q=0$, then $\Delta\theta=0$; –i.e. $\theta(z,T)=\theta(z,0)$, $\hat{\mathbf{n}}$ returns to the initial orientation at the end of pulse.

For all non-zero Q, its sign describes the tilt direction of $\hat{\mathbf{n}}$ with respect to its initial orientation, and its amplitude describes how far $\hat{\mathbf{n}}$ rotates from its initial state. We select the sign of Q in such a way that $\Delta\theta>0$ corresponds to $\hat{\mathbf{n}}$ reorients towards the direction of $\mathbf{E}$, Figure 4.2. With this agreement, Q is of the same sign as $\Delta\theta$ because ς is positive for materials considered in this work. When driving $\hat{\mathbf{n}}$ towards $\mathbf{E}$, a larger positive Q is required to obtain a larger $\Delta\theta$. In general, for a specific material with fixed values of G and τ, the value of Q is determined by the pulse shape $e(t)$, Eq. (4.8). Below we demonstrate how a maximum positive value of Q can be obtained by optimizing $e(t)$. We stress that the optimization is developed within a fixed time interval $[0,T]$ to obtain the maximum reorientation of $\hat{\mathbf{n}}$.

In order to maximize Q, we apply Euler-Lagrange equation to Eq. (4.8); however, Eq. (4.8) contains a double integral, therefore it is difficult to directly use Euler-Lagrange equation. To overcome this, we introduce

$$p(t)=\int_0^t \exp\left(-\frac{t-t'}{\tau}\right)e(t')dt'. \tag{4.9}$$

Taking derivatives with respect to t on both sides, one obtains

$$e(t)=\frac{\partial p(t)}{\partial t}+\frac{1}{\tau}p(t). \tag{4.10}$$

Substituting Eq. (4.10) into Eq. (4.8) yields

$$Q=\frac{1}{\tau}\int_0^T\left\{-\left[\frac{\partial p(t)}{\partial t}\right]^2+\frac{G^2-1}{\tau}p(t)\frac{\partial p(t)}{\partial t}-\frac{G^2}{\tau^2}p^2(t)\right\}dt. \tag{4.11}$$

We now can apply Euler-Lagrange equation to Eq. (4.11):

$$\frac{\partial^2 p(t)}{\partial t^2} = -\frac{G^2}{\tau^2} p(t). \tag{4.12}$$

The solution to Eq. (4.12) is

$$p(t) = C_1 \sin\left(\frac{G}{\tau}t\right) + C_2 \cos\left(\frac{G}{\tau}t\right), \tag{4.13}$$

where C_1 and C_2 are constants of integration. Thus combining Eq. (4.10) and Eq. (4.13), the optimal pulse shape is

$$e(t) = \left[\sin\left(\frac{G}{\tau}t\right)\left(C_1 - C_2 G\right) + \cos\left(\frac{G}{\tau}t\right)\left(C_1 G + C_2\right)\right]/\tau \tag{4.14}$$

One can see from Eq. (4.8) that the optimum pulse should not have negative values for $e(t)$, and the optimal pulse shape should have only one region where $e(t) = 1$ because the solution (4.14) which starts from the value 1 cannot return to the value 1 again without being negative. A general form of the pulse which meets the conditions above is shown in Figure 4.3. The pulse is comprised of three parts: (1) a rising part $[0, t_1]$ in which $e(t)$ rises from a 0 to 1; (2) a saturation part $[t_1, T - t_2]$ in which $e(t) = 1$; (3) a decaying part $[T - t_2, T]$ in which $e(t)$ decays from 1 to 0. When $t_1 = t_2 = 0$, one obtains the square pulse. Both t_1 and t_2 are determined from the optimization scheme below.

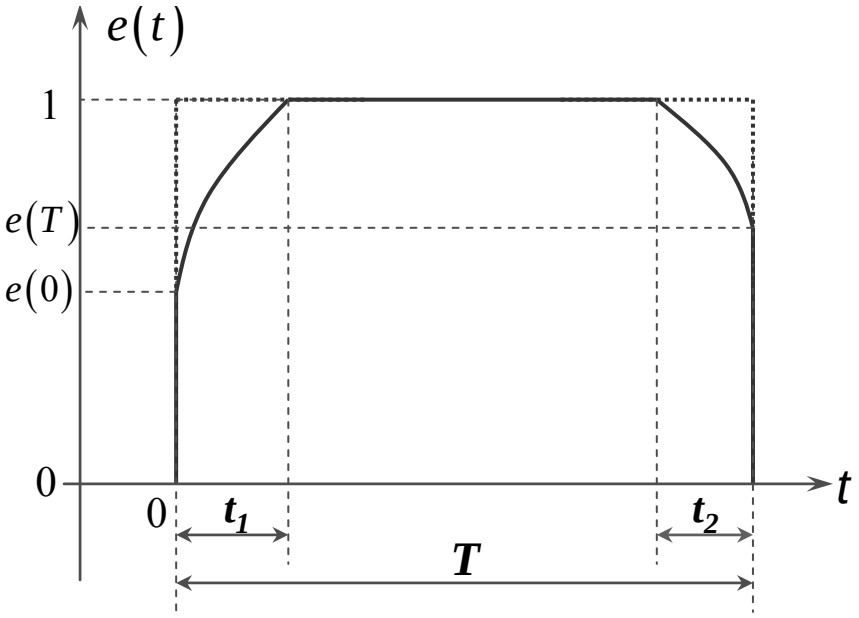

Figure 4.3. A normalized pulse $e(t)$ $(0 \le e(t) \le 1)$ is comprised of a rising part $[0, t_1]$, a saturation part $[t_1, T - t_2]$ and a decaying part $[T - t_2, T]$.

The constants C_1 and C_2 have different values for the rising and decaying parts, and needs to be determined separately.

For the rising part, the boundary conditions are: 1). $p(0) = 0$ from Eq. (4.9), thus $C_2 = 0$; 2). $e(t_1) = 1$, thus $C_1 = \tau\left[G\cos\left(\frac{G}{\tau}t_1\right) + \sin\left(\frac{G}{\tau}t_1\right)\right]^{-1}$. Therefore the pulse shape for the rising part can be written as

$$e(t) = \frac{G\cos(G * t/\tau) + \sin(G * t/\tau)}{G\cos(G * t_1/\tau) + \sin(G * t_1/\tau)}. \tag{4.15}$$

For the decaying part, the boundary conditions are: 1). $e(T - t_2) = 1$. 2). The natural boundary condition from Eq. (4.11) yields $e(T) + \tau \cdot \partial e(t)/\partial t\,|_{t=T} = 0$. Combining

the two conditions, one obtains $C_1 = \frac{\left(G^2-1\right)\cos\left(GT/\tau\right)+2G\sin\left(GT/\tau\right)}{\left(G^2+1\right)\left[G\cos\left(Gt_2/\tau\right)+\sin\left(Gt_2/\tau\right)\right]}\tau$ and $C_2 = \frac{2G\cos\left(GT/\tau\right)-\left(G^2-1\right)\sin\left(GT/\tau\right)}{\left(G^2+1\right)\left[G\cos\left(Gt_2/\tau\right)+\sin\left(Gt_2/\tau\right)\right]}\tau$. Therefore the pulse shape for the decaying part can be written as

$$e(t) = \frac{G\cos\left[G*(T-t)/\tau\right]+\sin\left[G*(T-t)/\tau\right]}{G\cos(G*t_2/\tau)+\sin(G*t_2/\tau)}. \tag{4.16}$$

We notice that Eq. (4.8) has an alternative symmetric form:

$$Q(T) = \frac{1}{\tau}\int_0^T\left[\frac{G^2+1}{2\tau}e(t)\int_0^t \exp\left(-\frac{|t-t'|}{\tau}\right)e(t')dt' - e^2(t)\right]dt, \tag{4.17}$$

which suggests that the extremum of Q is provided by a pulse with a symmetric form; – i.e. $t_1 = t_2$, here t_1 is the optimization parameter, which will be determined for specific values of T, G and τ. With Figure 4.3, Eq. (4.15) and (4.16), $t_1 = t_2$, the optimized pulse is written as

$$e(t) = \begin{cases} \dfrac{G\cos(G*t/\tau)+\sin(G*t/\tau)}{G\cos(G*t_1/\tau)+\sin(G*t_1/\tau)}, & t\in[0,\ t_1] \\ 1, & t\in[t_1,\ T-t_1] \\ \dfrac{G\cos\left[G*(T-t)/\tau\right]+\sin\left[G*(T-t)/\tau\right]}{G\cos(G*t_1/\tau)+\sin(G*t_1/\tau)}, & t\in[T-t_1,\ T] \end{cases}. \tag{4.18}$$

There are certain restrictions imposed on the value of t_1 by the shape of the pulse. In the rising part $[0,\ t_1]$, the derivative of $e(t)$ should be always positive $\left(\partial e(t)/\partial t > 0\right)$, and always negative $\left(\partial e(t)/\partial t < 0\right)$ for the decaying part $[T-t_1, T]$, because the maximum value for $e(t)$ is 1, Figure 4.3. On the other hand, the symmetry dictates that

the maximum time interval for rising and decaying is $T/2$. Combining these two conditions, one obtains the range of possible values for t_1,

$$0 < t_1 < \min\left[\tau \cdot \operatorname{arccot}(G)/G,\ T/2\right]. \tag{4.19}$$

For further discussions, we introduce the notations $x = t_1/\tau$, $x_0 = \operatorname{arccot}(G)/G$, $x_{1/2} = T/(2\tau)$ and $x_{\max} = \min(x_0, x_{1/2})$, and present T in a normalized form as T/τ.

$Q(x)$ can be obtained by substituting Eq. (4.18) into Eq. (4.8):

$$Q(x) = \frac{G^2}{\left[G\cos(Gx) + \sin(Gx)\right]^2} \cdot \left\{ \begin{array}{l} \left[\exp(2x - T/\tau)\left(1+G^2\right) + G^2\left(T/\tau - 1 - 2x\right)\right]\cos^2(Gx) + \\ \left(T/\tau - 2x\right)\sin^2(Gx) + \\ 1/2 - 3\cos(2Gx)/2 + \left[-1 + G^2\left(T/\tau - 2x\right)\right]\sin(2Gx)/G \end{array} \right\}. \tag{4.20}$$

Below, we analyze different dependences of $Q(x)$ on x for different values of G and T/τ. From Eq. (4.20), $\partial Q(x)/\partial x|_{x=0} = 0$ always holds true, i.e. $Q(0)$ is always an extremum. On the other hand, it is true $\partial Q(x)/\partial x|_{x=x_0} = 0$, thus $Q(x_0)$ is always an extremum as well.

(a) If $Q(0)$ is a maximum, thus $\partial^2 Q(x)/\partial x^2|_{x=0} < 0$. Under this condition, $\partial^2 Q(x)/\partial x^2|_{x=x_0} > 0$ is automatically valid, i.e. $Q(x_0)$ is a minimum. Calculations of Eq. (4.20) show that there is only one behavior for the dependence of $Q(x)$ on x, Figure 4.4 (a), where $Q(x)$ is positive for all x values ($x \in [0, x_0]$), and it monotonically decreases as x increases and reaches a minimum when $x = x_0$. We defines zone (a) in which all the G and T/τ values lead to the dependence of $Q(x)$ on x in Figure 4.4 (a), and the

square pulse produces the maximum rotation angle. Zone (a) is shown as the area on the right side of the dash curve which is determined by Eq. (4.21), in Figure 4.5, the diagram of G and T/τ which produces different dependences of $Q(x)$ on x.

$$\partial^2 Q(x)/\partial x^2 \,|_{x=0} = 2\left[\left(1+G^2\right)\exp\left(-T/\tau\right)+1-G^2\right]=0. \tag{4.21}$$

(b) If $Q(0)$ is the minimum, thus $\partial^2 Q(x)/\partial x^2 \,|_{x=0} > 0$. Under this condition, there are totally three different cases. When $Q(0)>0$, calculations of Eq. (4.20) show that $Q(x)$ reaches a maximum at $0 < x = x_m < x_0$, Figure 4.4 (b). We define zone (b) in which all G and T/τ values produce the dependence of $Q(x)$ on x in Figure 4.4 (b). The boundaries of this zone, which is the area between the dash and dot curves in Figure 4.5, are defined by Eq. (4.21) and (4.22). In this zone, the optimal pulse to drive $\hat{\mathbf{n}}$ towards $\mathbf{E}$ is the pulse with a maximum positive $Q(x_m)$.

$$Q(0)=\left(T/\tau-1\right)G^2+\left(G^2+1\right)\exp\left(-T/\tau\right)-1=0. \tag{4.22}$$

(c) $Q(0)<0$ and $Q(x)$ changes the sign in the range $[0, x_0]$. The extreme of this condition is that $Q(x)$ changes the sign at $x = x_0$; –i.e. $\partial^2 Q(x)/\partial x^2 \,|_{x=x_0} = 0$ which coincides with the conditions $x_0 = x_{1/2}$ and $Q(x_0)=0$, Figure 4.4 (c). We define zone (c) in which all G and T/τ values produce the dependence of $Q(x)$ on x in Figure 4.4 (c). The boundaries of this zone, which is the area between the dot and solid curves in Figure 4.5, are defined by Eq. (4.22) and (4.23). In this zone, the optimal pulse to drive $\hat{\mathbf{n}}$ towards $\mathbf{E}$ is the pulse with the largest value of $Q(x)$.

$$\partial^2 Q(x)/\partial x^2 \,|_{x=x_0} = 0 \Rightarrow \operatorname{arccot}(G)/G = T/(2\tau). \tag{4.23}$$

(d) $Q(0)<0$ and $Q(x)<0$. We define zone (d) in which all G and T/τ values produce the dependence of $Q(x)$ on x in Figure 4.4 (d). The boundary of this zone, which is the area on the left side of the solid curve in Figure 4.5, is defined by Eq. (4.23). In this zone, the optimal pulse to drive $\hat{\mathbf{n}}$ towards $\mathbf{E}$ is the pulse with $x = x_{\max} = x_{1/2}$. (We plot $Q(x)$ for the range $[x_{1/2}, x_0]$ as the dashed lines in Figure 4.4 (d) to show that $Q(x)$ reaches a maximum at $x = x_0$).

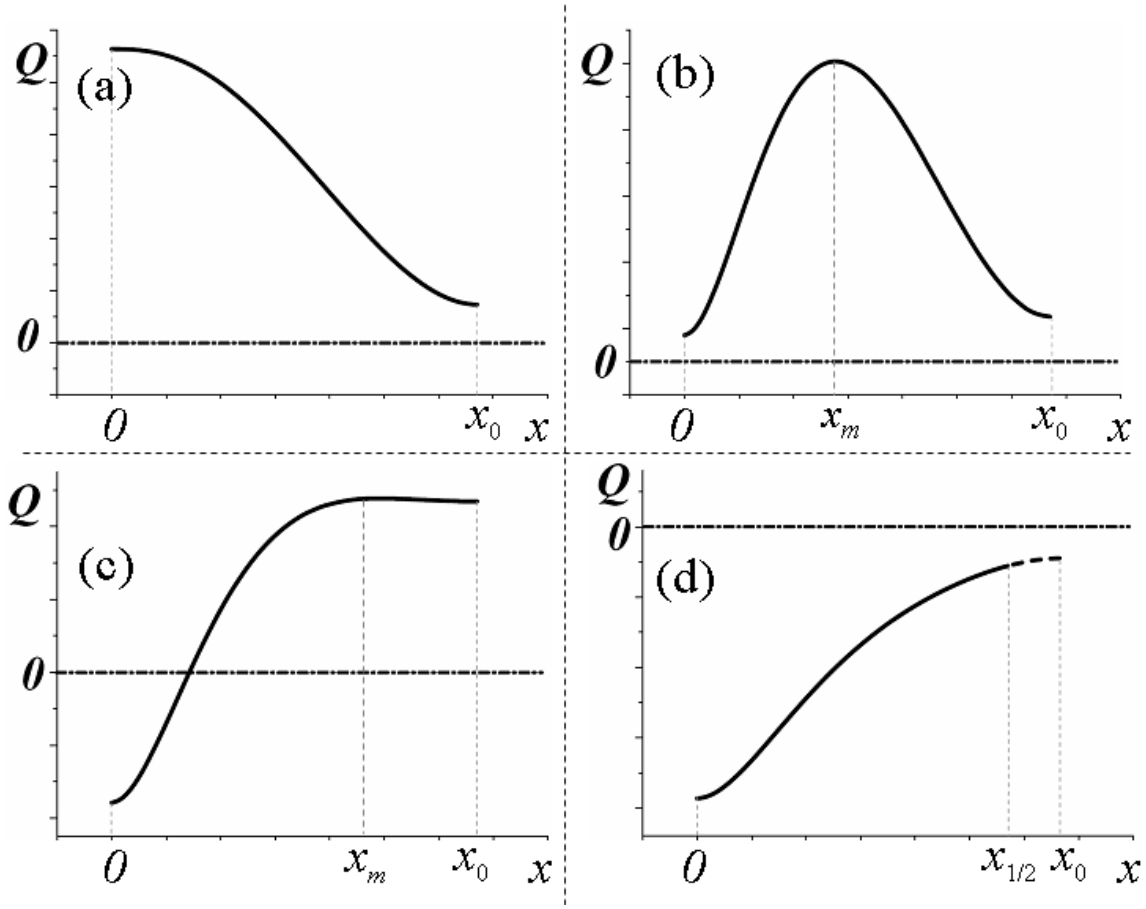

Figure 4.4. Typical behaviors of $Q(x)$ as a function of x under different G and T/τ values: (a), (b), (c) and (d).

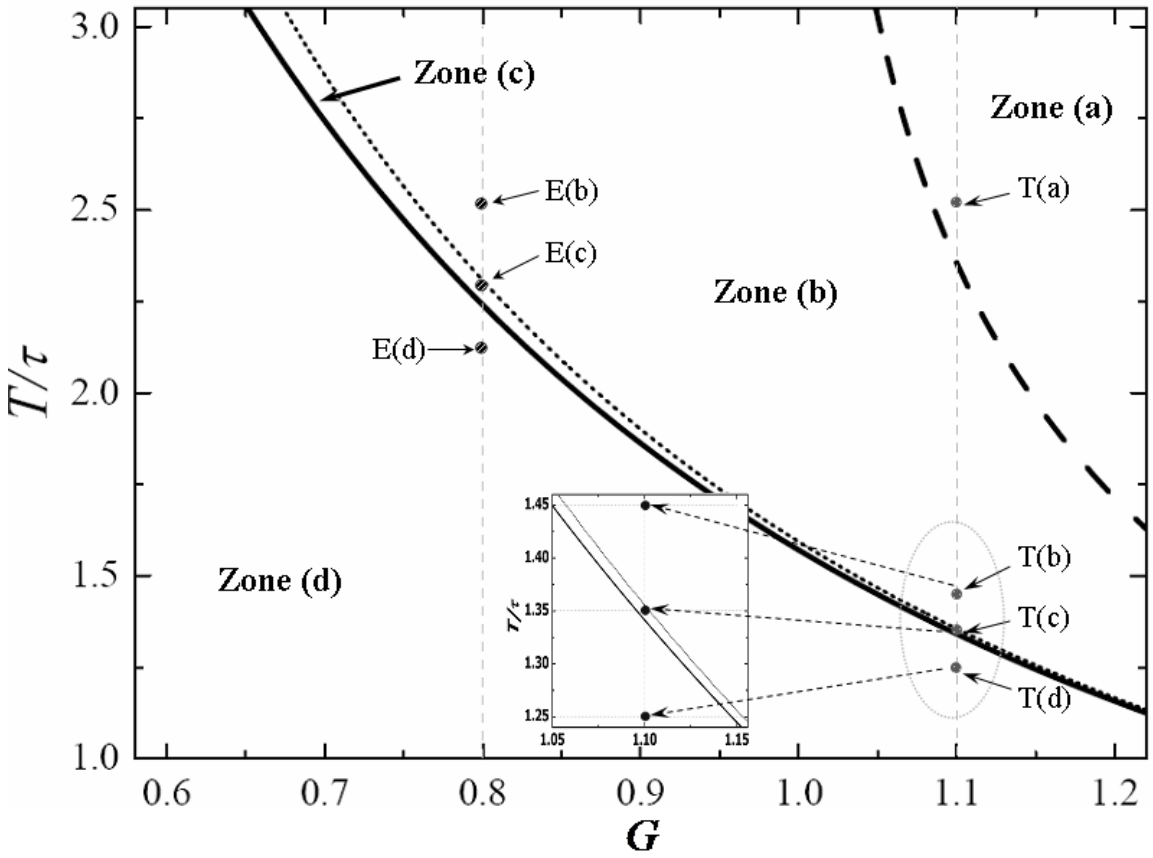

Figure 4.5. The diagram for G and T/τ which produces different dependences of $Q(x)$ on x. The dashed curve is defined by Eq. (4.21); the dot curve is defined by Eq. (4.22); and the solid curve is defined by Eq. (4.23). The fours points T(a), T(b), T(c) and T(d) represent the values for G and T/τ to obtain Figure 4.4. E(b), E(c) and E(d) represent the values for G and T/τ for the experiments, Figure. 4.8-10.

With Figure 4.5 and Eq. (4.18), optimized pulses can be designed to drive $\hat{\mathbf{n}}$ towards $\mathbf{E}$ for materials with different G and τ values. Below, we present experimental results.

4.2 Experimental results and discussions

The cell was constructed by bonding two glass substrates coated with transparent indium tin oxide (ITO) electrodes. The cell gap is $d = 19\ \mu$m, as measured by the interference method. A SiO_x layer was deposited on top of the ITO layer to obtain a uniform alignment with the optical axis along x axis, yielding $\theta = 17.6^{o}$ as measured by the retardation compensation technique. The 2F-3333 DFN mixture is chosen for the experiment, with dielectric parameters $\varepsilon_{l\|} = 13.0$, $\varepsilon_{h\|} = 4.2$, $\varepsilon_{\perp} = 9.1$, $\tau = 69\ \mu$s and $G \approx 0.8$ at 20^{o} C. The cell is thermo-stabilized at 20^{o} C in the LTS120 Analysa Peltier thermal system from Linkam Scientific Instruments, with a temperature stability and accuracy of 0.1^{o} C.

The cell was placed between two crossed polarizers with the optical axis making an angle 45^{o} with respect to the transmission axes of the polarizers. The intensity of He-Ne laser beam ($\lambda = 633$ nm) that passes through the cell is measured by a photodiode (high speed silicon detector NT54-520, Edmund Industrial Optics) with an analog amplifier AD 8067 (Analog Devices). The recorded signal is displayed on a Tektronix TDS 210 oscilloscope, which is connected to a computer via IEEE-488 cable for data storage and analysis [IEEE-488 is also commonly known as the General Purpose Interface Bus (GPIB)]. The pulses are produced by the WFG500 wave-form generator (FLC Electronics) in combination with the KH7602 wideband amplifier (Krohn-Hite), and the output pulse shape can be controlled by a computer via a RS232 connection.

The optical phase shift of the cell $\Delta\varphi(t)$ under this configuration is [11]:

$$\Delta\varphi(t) = \frac{2\pi n_o}{\lambda}\int_0^d \left[n_e / \sqrt{n_o^2 \sin^2\theta(z,\ t) + n_e^2 \cos^2\theta(z,\ t)} - 1 \right] dz\,, \qquad (4.24)$$

where n_o and n_e are the ordinary and extraordinary refractive indices of the LC, respectively. The optical phase compensator SB-10 (Optics for Research) with a controllable phase delay $\Delta\varphi'$ is inserted between the cell and the analyzer in order to adjust the normalized transmitted light intensity,

$$I(t) = \sin^2\left[\frac{\Delta\varphi(t) + \Delta\varphi'}{2}\right], \qquad (4.25)$$

in such a way that in the absence of electric field, $I(t)$ is about 1/2 of its maximum possible value. At this setting, the sensitivity of the system to the light intensity change caused by the director reorientation is maximized. We have chosen $\Delta\varphi'$ in such a way that the field-induced reorientation of $\hat{\mathbf{n}}$ *towards* $\mathbf{E}$ corresponds to the *increase* of $I(t)$.

Figure 4.6 shows the transmission curve when we apply voltages with two different frequencies, 1 kHz and 50 kHz, at which $\Delta\varepsilon$ is positive and negative, respectively. The sinusoidal pulses are used in order to avoid the rapid change of the electric field which could induce the effects of dielectric dispersion. The initial field-free state is denoted as "O". On the left half, f = 50 kHz, at which $\Delta\varepsilon < 0$ for 2F-3333, so $\hat{\mathbf{n}}$ tilts away from $\mathbf{E}$, corresponding to the light intensity decrease at the beginning of switching. On the right half, f = 1 kHz, at which $\Delta\varepsilon > 0$, so $\hat{\mathbf{n}}$ tilts towards $\mathbf{E}$, corresponding to the light intensity increase.

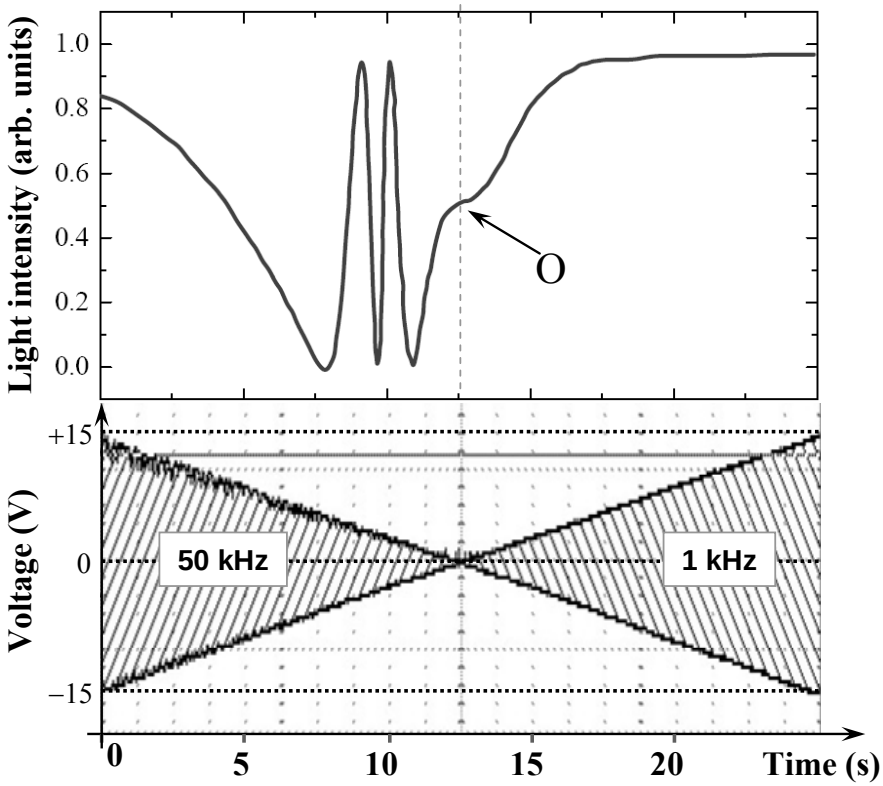

Figure 4.6. The transmitted light intensity of the cell filled with 2F-3333 between two crossed polarizers when two sinusoidal pulses with different frequencies are applied at 20° C. The left half is f = 50 kHz at which $\Delta\varepsilon < 0$; the right half corresponds to f = 1 kHz at which $\Delta\varepsilon > 0$. The point O is the initial field-free state. The maximum voltage is 15 V.

When the cell filled with 2F-3333 is subject to a fast rising pulse, the sharp rising front is perceived by the LC as a high frequency excitation for which $\Delta\varepsilon < 0$, therefore $\hat{\mathbf{n}}$ will first tilt away from **E** (from O to O'), then tilt towards **E** (from O' to O"), Figure 4.7. The purpose of using a larger pulse amplitude than the one in Figure 4.6 is to enhance the effect of dielectric dispersion. Below, we use both the optimized non-square pulses and the regular square pulses to drive $\hat{\mathbf{n}}$ towards **E**, and compare the total phase

retardation change within a fixed time interval. The measured total phase retardation change $\Delta\varphi(x)=\varphi(T)-\varphi(0)$ within the time interval T is normalized by the absolute value of the retardation change $|\Delta\varphi(0)|$ when the square pulses are used. The retardation value is positive when $\hat{\mathbf{n}}$ reorients parallel to $\mathbf{E}$, and negative when $\hat{\mathbf{n}}$ reorients perpendicularly to $\mathbf{E}$. From Figure 4.5, when G and τ are fixed, one can test the dependence of $Q(x)$ on x in different zones by choosing different values for T. In the experiments of driving the cell filled with 2F-3333, $G\approx 0.8$, we compare the $Q(x)$ behaviors in three different zones: (b), (c) and (d) by choosing three values for T, corresponding to the three points E(b), E(c) and E(d) in Figure 4.5. Zone (a) cannot be compared with zone (b), (c) and (d) directly because G is fixed at 0.8 for 2F-3333.

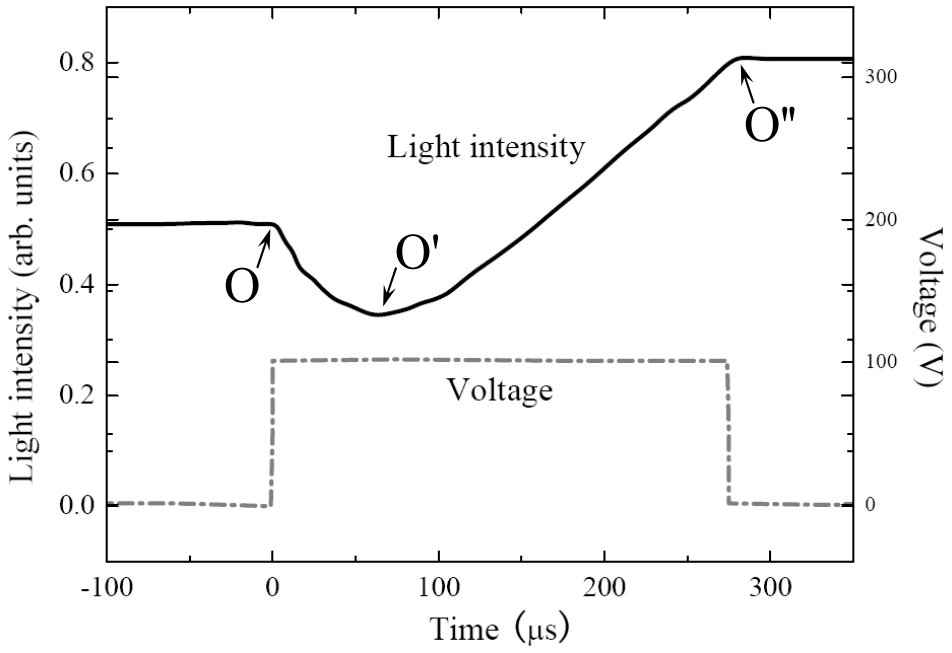

Figure 4.7. The transmitted light intensity change when a 100 V square pulse is applied on the cell filled with 2F-3333 at 20° C.

Zone (b): We chose $T_b = 175\ \mu s$, thus $T_b / \tau \sim 2.53$, corresponding to the point E(b) in Figure 4.5. Eleven pulses defined by Eq. (4.18) are used to drive the LC by choosing eleven values for x: (0, 0.1, 0.2, 0.3, 0.4, 0.5, 0.6, 0.7, 0.8, 0.9, 1.0) ($x_{\max} = \min\left[x_0, x_{1/2}\right] = 1.12$). The maximum voltage is 150 V, Figure. 4.8. All pulses drive $\hat{\mathbf{n}}$ towards $\mathbf{E}$, $\theta(T_b) < \theta(0)$, but the change of $\Delta\theta(x)$ is not monotonic, at a certain value of x, $\Delta\theta$ reaches a maximum (Q reaches a maximum positive value); further increase of x decreases $\Delta\theta$. This agrees with the model, Figure 4.4(b). The deviation of the pulse shape in experiments (the voltage rising and decaying are almost linear) from theory (nonlinear rising and decaying) is caused by the limited time step of the function generator.

Zone (c): We chose $T_c = 159\ \mu s$, thus $T_c / \tau \sim 2.30$, corresponding to the point E(c) in Figure 4.5. Eleven pulses defined by Eq. (4.18) are used to drive the LC by choosing eleven values for x: (0, 0.1, 0.2, 0.3, 0.4, 0.5, 0.6, 0.7, 0.8, 0.9, 1.0) ($x_{\max} = \min\left[x_0, x_{1/2}\right] = 1.12$). The maximum voltage is 200 V, Figure. 4.9. As x increases, the final orientation of $\hat{\mathbf{n}}$ becomes less perpendicular to $\mathbf{E}$ with respect to the initial orientation, which indicates negative Q with decreasing absolute values; when $x \sim 0.4$, $\hat{\mathbf{n}}$ returns to the initial orientation ($\Delta\theta = 0$); pulses with larger values of x drives $\hat{\mathbf{n}}$ towards $\mathbf{E}$, which implies a positive Q with increasing values, which agrees with the model, Figure 4.4(c).

Zone (d): We chose $T_d = 145\ \mu s$, thus $T_d / \tau \sim 2.10$, corresponding to the point E(d) in Figure 4.5. Eleven pulses defined by Eq. (4.18) are used to drive the LC by choosing eleven values for x: (0, 0.1, 0.2, 0.3, 0.4, 0.5, 0.6, 0.7, 0.8, 0.9, 1.0)

($x_{\max} = \min\left[x_0, x_{1/2}\right] = 1.05$). The maximum voltage is 150 V, Figure. 4.10. Under all pulses, the final orientation of $\hat{\mathbf{n}}$ is more away from $\mathbf{E}$ than the initial orientation, $\theta(T_d) > \theta(0)$, but $|\Delta\theta|$ becomes smaller as x increases. This indicates Q is negative for all x values and $|Q|$ decreases as x increases, which is in agreement with the model, Figure 4.4(d).

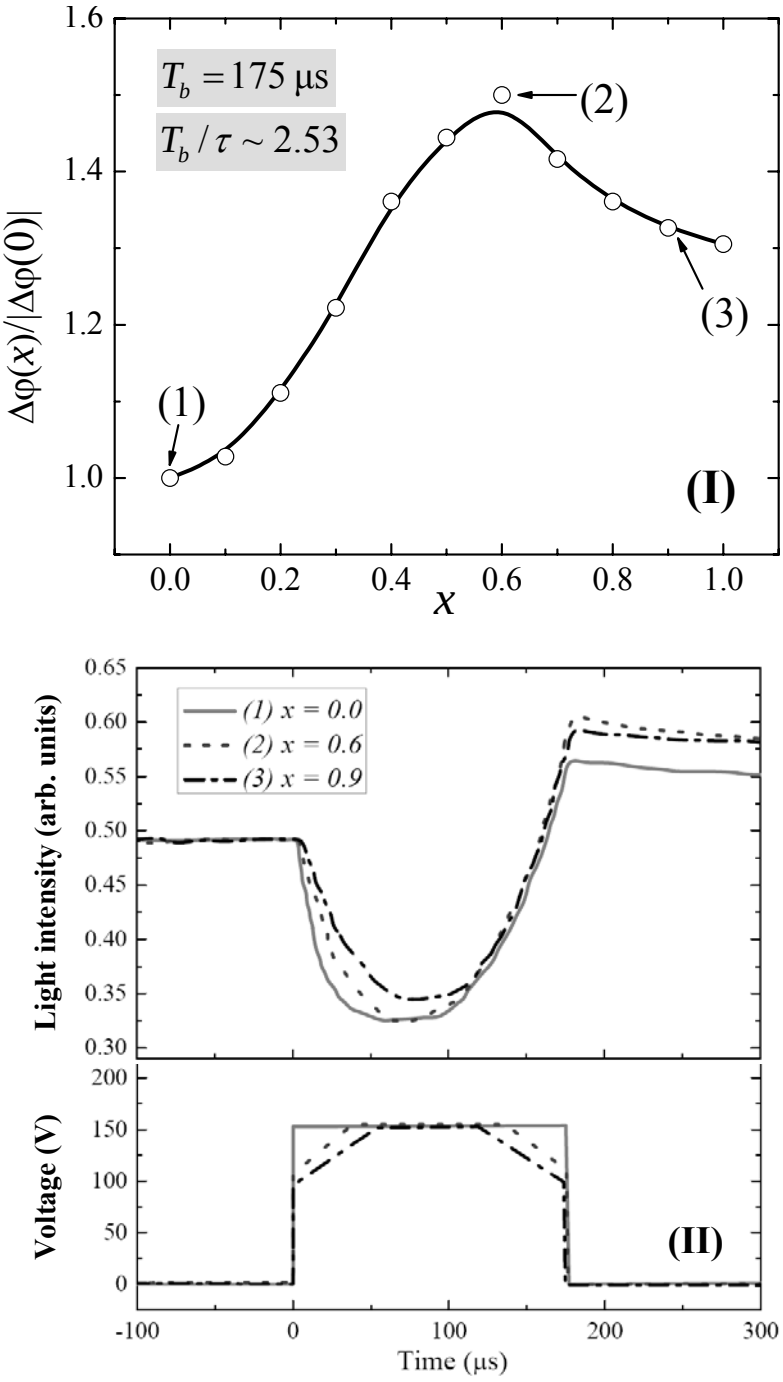

Figure. 4.8. (I) The normalized retardations under different driving pulses with different x values in zone (b) at 20° C. (II) The light intensity change under three corresponding driving pulses, specified as (1), (2) and (3) in (I).

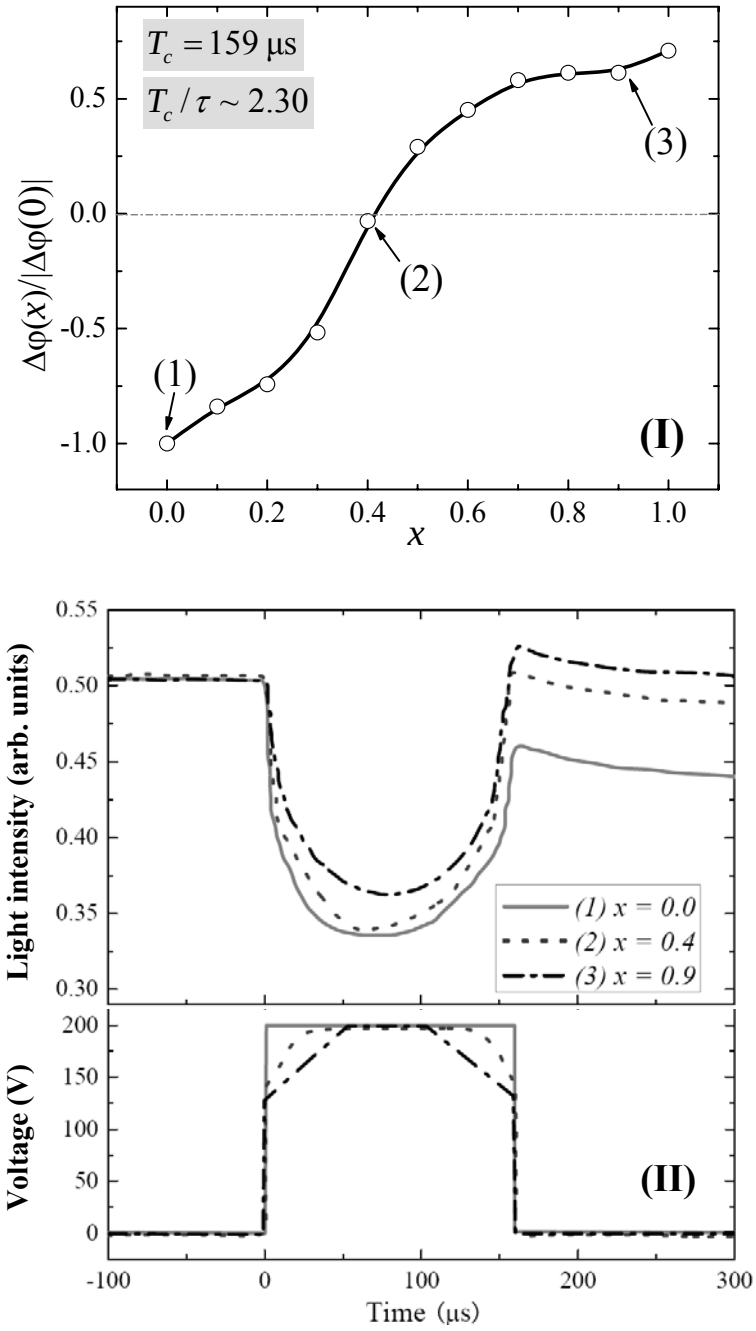

Figure. 4.9. (I) The normalized retardations under different driving pulses with different x values in zone (c) at 20° C. (II) The light intensity change under three corresponding driving pulses, specified as (1), (2) and (3) in (I).

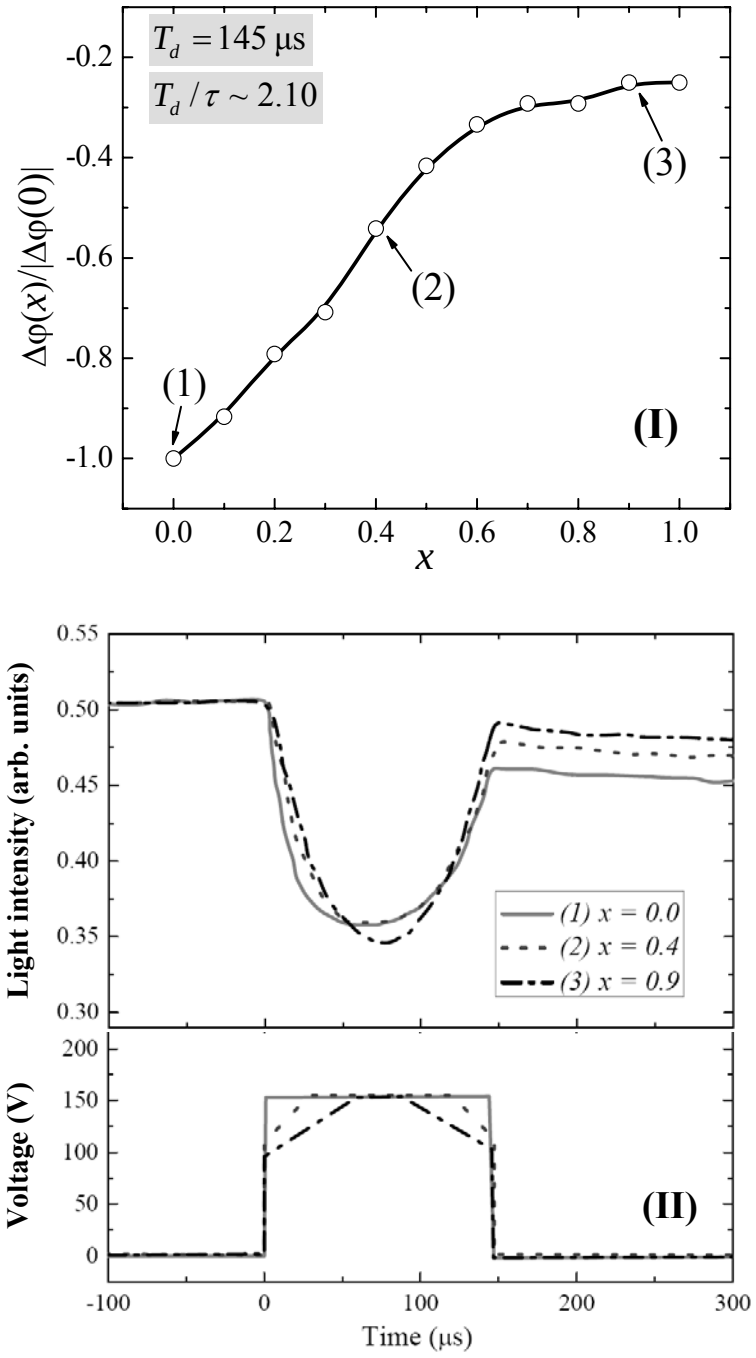

Figure. 4.10. (I) The normalized retardations under different driving pulses with different x values in zone (d) at 20° C. (II) The light intensity change under three corresponding driving pulses, specified as (1), (2) and (3) in (I).

4.3 Summary

We report a model to describe the effect of pulse shape on the director orientation dynamics; and optimized pulses based on this model are able to efficiently drive the director towards the electric field. The optimized pulses are mainly determined by dielectric relaxation time τ, material constant G, optimization parameter x and pulse duration T. The obtained pulses are tested in the experiment of switching a DFN material, and the results agree well with the model. The model proposed here should be of interest in the development of fast-switching LC devices. In practical implementations of this model when designing LC devices, one shall first characterize the dielectric dispersion of the LC materials, through which the components of the dielectric tensor (thus to obtain G) and relaxation time τ can be known. With known values of G and τ, optimized values for T and t_1 can be found from Figure 4.5, thus to design the optimum driving pulses.

In principle, the model is valid not only for the cell geometry described above where the director rotates in the plane perpendicular to the substrate, but also valid for the configuration where the director rotates in the plane of substrate, such as the IPS LCD mode. In the case where the LCs are dielectrically negative ($\Delta\varepsilon < 0$), which are widely used in the vertical alignment mode LCD [21], the effect of dielectric dispersion is preferred because it speeds up the switching [5].

Chapter 5

POLAR AND NON-POLAR ORDERINGS IN THE ELECTRICALLY INDUCED ISOTROPIC-NEMATIC PHASE TRANSITION

Dynamics of phase transitions is a fundamental problem of statistical physics. It is usually described by the Landau-Khalatnikov (LK) theory in which the order parameter evolution is determined by the corresponding free energy that is a function of external parameters such as temperature, field, etc. In many cases, however, the external parameters influence the order parameter indirectly. A good example is the establishment of orientational nematic (N) order by an electric field **E**. The N order is described by the Landau – de Gennes expansion with a non-polar scalar order parameter S [1]:

$$f = f_0 + \frac{1}{2}a\left(T - T^*\right)S^2 - \frac{1}{3}bS^3 + \frac{1}{4}cS^4 + \ldots - \frac{\varepsilon_0 \Delta\varepsilon_m}{3}E^2 S\,, \qquad (5.1)$$

where f_0 is the free energy density of an isotropic (I) phase with $S = 0$; a, b and c are the expansion coefficients, T and T^* are the actual and supercooling temperatures respectively; $\Delta\varepsilon_m$ is the maximum dielectric anisotropy for $S = 1$. However, the prime effect of **E** is an establishment of the *polar* order in the material, through a

macroscopic electric polarization $\mathbf{P}$. This polarization $\mathbf{P}$ depends on the dielectric tensor and therefore on the order parameter S; as a result, the standard dielectric term $\frac{1}{2}\mathbf{P}\cdot\mathbf{E}$ leads to the last term in Eq. (5.1). The relationship between this term and dielectric anisotropy and their temperature dependence has been discussed in Ref. [49]. In this work, we discuss the role of $\mathbf{P}$ in the dynamics of the field-induced isotropic-nematic phase transition. The relevant LK equation for the dynamics of phase transition is described by Eq. (1.33) [18], which considers the interaction between $\mathbf{E}$ and S as a direct and instantaneous one; the evolution of $\mathbf{P}$ that is ultimately responsible for the link between $\mathbf{E}$ and S, is completely ignored. The goal of this work is to determine the dynamics of *both* $\mathbf{P}$ and S during the field-induced I-N phase transition. Theoretically, the problem boils down to the derivation of dynamical equations for $\mathbf{P}(t)$ and $S(t)$ using the Langevin approach, while experimentally, we measure $\mathbf{P}(t)$ and $S(t)$ in response to a polarity reversal of a strong electric field that establishes a N phase with both polar ($\mathbf{P}$) and nonpolar (S) order.

5.1 Theory

Consider a uniaxial nematic LC with a director $\hat{\mathbf{n}}$ parallel to an applied electric field $\mathbf{E}$. Using the Maier-Saupe model, the orientational potential $V(\theta)$ of a given molecule with a permanent dipole $\boldsymbol{\mu}$ along the long axis can be expressed as the sum of Legendre polynomials $P_n(\cos\theta)$ [50]:

$$V(\theta) = -\mu E P_1(\cos\theta) - \left[\left(\alpha_{\|} - \alpha_{\perp}\right)E^2(t) + B\overline{P_2}(t)\right]P_2(\cos\theta) \qquad (5.2)$$

where θ is the angle between $\boldsymbol{\mu}$ and $\hat{\mathbf{n}}$, $\alpha_{\|}$ and $\alpha_{\perp}$ are the molecular polarizabilities parallel and perpendicular to the long molecular axis, the bar in $\overline{P}_2(t)$ and in what follows implies an ensemble average, and B is a parameter of the Maier-Saupe potential [51]. The Langevin equations for the dynamics of $\overline{P}_n(t)$ for this potential are [52]:

$$\tau_n \frac{\partial \overline{P}_n(t)}{\partial t} = -\left(1 - \frac{3}{(2n-1)(2n+3)}u(t)\right)\overline{P}_n(t) + \frac{e(t)}{2n+1}\left(\overline{P}_{n-1}(t) - \overline{P}_{n+1}(t)\right) + \\ + \frac{3u(t)}{2n+1}\left[\frac{n-1}{2n-1}\overline{P}_{n-2}(t) - \frac{n}{2n+3}\overline{P}_{n+2}(t)\right] \qquad (5.3)$$

where $\tau_n = 2\tau/n(n+1)$ is a rotational relaxation time for $\overline{P}_n(t)$ in the I state, τ is the Debye relaxation time in the I phase, $u(t) = \left(\xi e^2(t) + b\overline{P_2}(t)\right)/k_B T$, $\xi = k_B T\left(\alpha_{\|} - \alpha_{\perp}\right)/3v\mu^2$, and $e(t) = \mu E(t)/k_B T$ is a normalized electric field, k_B is the Boltzmann constant, and v is the volume per molecule. Note that the parity of n defines the parity of $\overline{P}_n(t)$ with respect to $e(t)$.

In Eq. (5.3), the slowest relaxation should be observed for $\overline{P}_1(t)$ and $\overline{P}_2(t)$ since $\tau_n \propto n^{-2}$ and since the relaxation of these quantities is hindered by specific slow-down effects such as an energetic barrier for flip-flop of permanent dipoles and the proximity of the N-I phase transition, respectively. Thus we can assume that the higher order polynomials with $n \geq 3$ reach the equilibrium state instantaneously. Their equilibrium values can be found as stationary solutions of Eq. (5.3) for $n \geq 3$

controlled by the current values of $\bar{P}_1(t)$ and $\bar{P}_2(t)$. Using these solutions for $\bar{P}_3(t)$ and $\bar{P}_4(t)$, we obtain the close set of dynamic equations for $\bar{P}_1(t)$ and $\bar{P}_2(t)$:

$$\tau \frac{\partial \bar{P}_1(t)}{\partial t} = \frac{e(t)}{3} - M_{11}(t)\bar{P}_1(t) + M_{12}(t)e(t)\bar{P}_2(t), \tag{5.4}$$

$$\tau \frac{\partial \bar{P}_2(t)}{\partial t} = \frac{3u(t)}{5} + M_{21}(t)e(t)\bar{P}_1(t) - M_{22}(t)\bar{P}_2(t), \tag{5.5}$$

where $M_{jk}(t) > 0$ are functions of $\overline{P_2}(t)$ and $e^2(t)$. Equations (5.4) and (5.5) describe the dynamics of the polarization $\bar{P}_1(t) = vP(t)/\mu$ and the order parameter $S = \bar{P}_2(t)$ of the uniaxial N system under an external electric field $e(t)$.

Considering $e(t)$ as an independent function, we obtain a general solution for Eq. (5.4):

$$\bar{P}_1(t) = \left[\frac{1+3M_{12}(t)\bar{P}_2(t)}{3M_{11}(t)}e(t)\right] + \left\{\begin{array}{l} \bar{P}_{10}F(t) - \dfrac{1+3M_{12}(t)\bar{P}_2(t)}{3M_{11}(t)}e(t) + \\ \dfrac{F(t)}{\tau}\displaystyle\int_0^t \frac{e(t')}{F(t')}\left[\frac{1}{3} + M_{12}(t')\bar{P}_2(t')\right]dt' \end{array}\right\}, \tag{5.6}$$

where the first term $\bar{P}_1^{ins}(t)$ is the instantaneous response (equivalent to the one used in the LK model), and the second term $\bar{P}_1^{mem}(t)$ is a memory term that is caused by the finite relaxation of the polarization; here $F(t) = \exp\left[-\frac{1}{\tau}\int_0^t M_{11}(t')dt'\right]$. $\bar{P}_1^{mem}(t)$ disappears when $\tau \to 0$. Substituting the solution (5.6) into (5.5), we obtain the dynamical equation for $\bar{P}_2(t)$:

$$\tau \frac{\partial \bar{P}_2(t)}{\partial t} = \frac{3u(t)}{5} - M_{22}(t)\bar{P}_2(t) + \frac{1+3M_{12}(t)\bar{P}_2(t)}{3M_{11}(t)}M_{21}(t)e^2(t) + M_{21}(t)e(t)\bar{P}_1^{mem}(t), \tag{5.7}$$

where the first three terms on the right hand side are equivalent to the LK model whereas the last term represents the effect of the finite rate of polarization relaxation. We turn now to the experimental determination of $\bar{P}_1(t) = vP(t)/\mu$ and $\bar{P}_2(t) = S(t)$.

5.2 Experimental results and discussions

The cell of a classic sandwich type was constructed with a reduced area of the indium tin oxide (ITO) electrodes, $A = 5\ \text{mm}^2$, separated by a gap $d = 3.8\ \mu\text{m}$. The purpose of using a small active area is to reduce the RC load, thus to reduce the delay of the electric field applied to the LCs [22]. No polyimide alignment layer is used to avoid the drop of potential across such a layer [53]. The cell is stabilized in the LTS120 hot stage (Linkam Scientific Instruments), with an accuracy of 0.1 ^{o}C. We use a pulse generator HV1000 (Direct Energy) capable of changing the voltage within a few tens of nanoseconds. We chose *p*-cyanophenyl *p*-n-heptylbenzoate (7CPB), $T_C = 330\ \text{K}$, $v = 2.86 \times 10^{-28}\ \text{m}^3$, as the N LC, because of its large longitudinal moment ($\mu = 5.6\ \text{D}$ [54]) and relatively long dielectric relaxation time (tens of ns in the I phase). The dielectric dispersion of 7CPB in the isotropic phase is shown

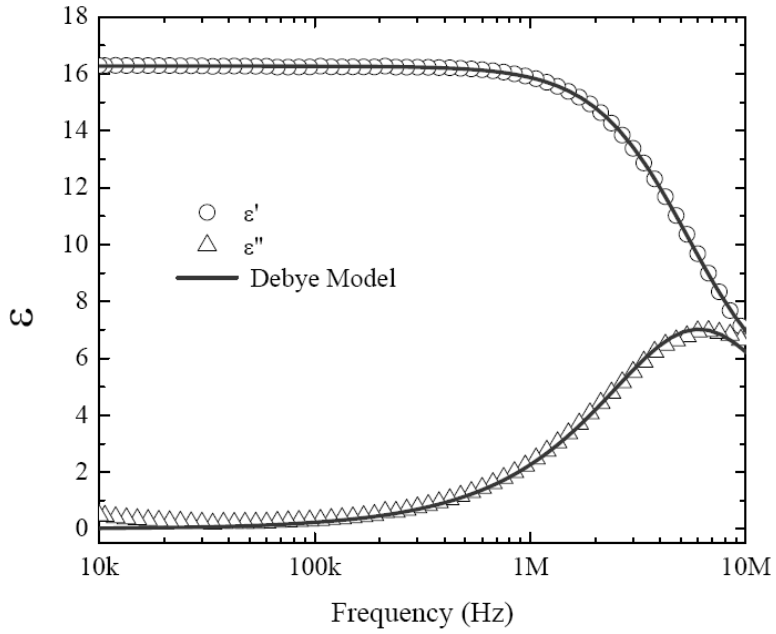

Figure 5.1. The dielectric dispersion of 7CPB at $T_C + 1.0\,\mathrm{K}$. The data is fitted with the Debye model, $\varepsilon^* = \varepsilon_h + \dfrac{\varepsilon_l - \varepsilon_h}{1 - i2\pi f\tau}$, with the parameters: $\varepsilon_l = 16.3$, $\varepsilon_h = 4.8$, $\tau = 30$ ns.

The LC, kept at $T > T_C$, was subject to a strong electric voltage that abruptly changed its polarity. We first applied $U_0 = 100$ V to establish the field-induced polar $\bar{P}_{10}(T, U_0)$ and nonpolar $\bar{P}_{20}(T, U_0)$ order parameters. The time duration of the pulse was 1.5 ms, long enough to saturate both $\bar{P}_{10}$ and $\bar{P}_{20}$, as evidenced by the decrease of electric current down to 0 and by saturated light transmittance through the cell. Note that the applied voltage is well above the typical "anchoring breaking" threshold [55], so that the ordered state can be considered uniformly homeotropic throughout the cell.

At time $t = 0$, the polarity of the field was reversed abruptly, within ~100 ns. The sharp voltage reversal was essential to trace the dynamics of both $\bar{P}_1(t)$ and $\bar{P}_2(t)$. The sharp polarity reversal should flip the direction of **P**. If $\bar{P}_1(t)$ adjusts instantaneously to the field reversal, then $\bar{P}_2(t) = \text{const}$ during the instantaneous polarity reversal, as it depends on $e^2(t)$. Our experiments below demonstrate that $\bar{P}_2(t)$ does change; these changes can be attributed not only to the finite rate of voltage change but also to the finite rate of $\bar{P}_1(t)$ adjustment caused by the finite rate of Debye dielectric relaxation.

There are two thermal effects associated with the applied voltage. First, as established by Lelidis and Durand, the field-induced orientational order is accompanied by an adiabatic temperature increase (< 0.5 ^{o}C) within the first 1 μs which then relaxes over the period of time ~100 μs. Since the voltage reversal in our experiments was performed 1.5 ms after the voltage switch-on, this adiabatic temperature variation has decayed significantly ($\sim 2\times 10^{-3} K/\mu s$ [19]) within the time interval ~1 μs of $\bar{P}_1(t)$ and $\bar{P}_2(t)$ changes (see below). Furthermore, our experiment was designed to eliminate the very cause for the Lelidis-Durand thermal effect: since the voltage amplitude remains the same, the stationary values of the field-induced $\bar{P}_2(t)$ before and after the voltage reversal should be the same ($=\bar{P}_{20}$). The second thermal effect comes from the dielectric heating caused by reorientation of $\bar{P}_1(t)$. The temperature change can be estimated as $\sim T\bar{P}_{10}^2$ which is ~1 ^{o}C. The latter estimate is

an upper limit; as shown below, this heating leads to small changes in the stationary value of $\overline{P}_2(t)$ established after the voltage reversal.

To determine the polarization $P(t)$, we used the Martinot-Lagarde method [56] by serially connecting the cell with a resistor R and the generator, Figure 5.2. Under this measurement scheme,

$$P(t) = P_0 - \frac{1}{A}\int_0^t \frac{U_R(t')}{R}dt' - \varepsilon_0 \varepsilon_{\square}^h(T, e_0)\frac{U_{LC}(t) - U_0}{d}, \tag{5.8}$$

where $P_0 = \varepsilon_0\left[\varepsilon_{\parallel}^l(T, e_0) - \varepsilon_{\parallel}^h(T, e_0)\right]U_0 / d$, $U_R(t)$ is the voltage drop at R, $U_{LC}(t) = U(t) - U_R(t)(1 + R_{ITO} / R)$ is the voltage across the LC; $U_{LC}(t \le 0) = U_0$; $\varepsilon_{\parallel}^l(T, e_0)$ and $\varepsilon_{\parallel}^h(T, e_0)$ are the values of the parallel component of the dielectric tensor at low and high frequencies. To trace $P(t)$, one needs to know all the parameters on the right hand side of Eq. (5.8). $U(t)$ and $U_R(t)$ are measured directly, Figure 5.3(a, b). Their dynamics is temperature dependent. The small temperature dependence of $U(t)$ is related to the changes in the load caused by temperature-sensitive behavior of the LC cell. The temperature dependence of $U_R(t)$ is much more pronounced because it is related directly to the temperature sensitivity of the field-induced polar order dynamics.

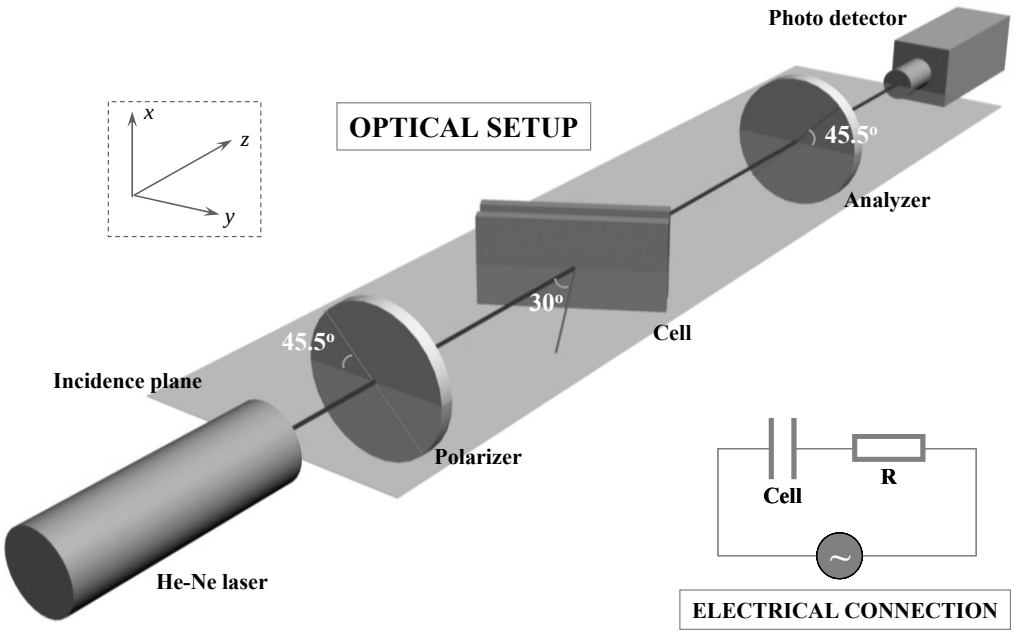

Figure 5.2. Optical setup and electric connection for the experiment.

The rest of the parameters in Eq. (5.8) were evaluated as follows. We have found that $\varepsilon_{\|}^{h}\left(T,e_0\right)$ can be considered as a constant for 7CPB in the range of the interest. At zero field and $T=T_C-7\ \mathrm{K}$, $\varepsilon_{\|}^{h}\left(T,0\right)$ was determined to be 4.0 by fitting the dielectric relaxation spectrum with the Debye model. In the I phase, $T=T_C+1\ \mathrm{K}$, the Debye fit yields $\varepsilon_{iso}^{h}\left(T,0\right)=4.2$. Since the two values are close, we consider $\varepsilon_{\|}^{h}\left(T,e_0\right)=4.1$ as independent of the temperature and of the field-induced order parameter (within the range of the existence of the field-induced N phase).

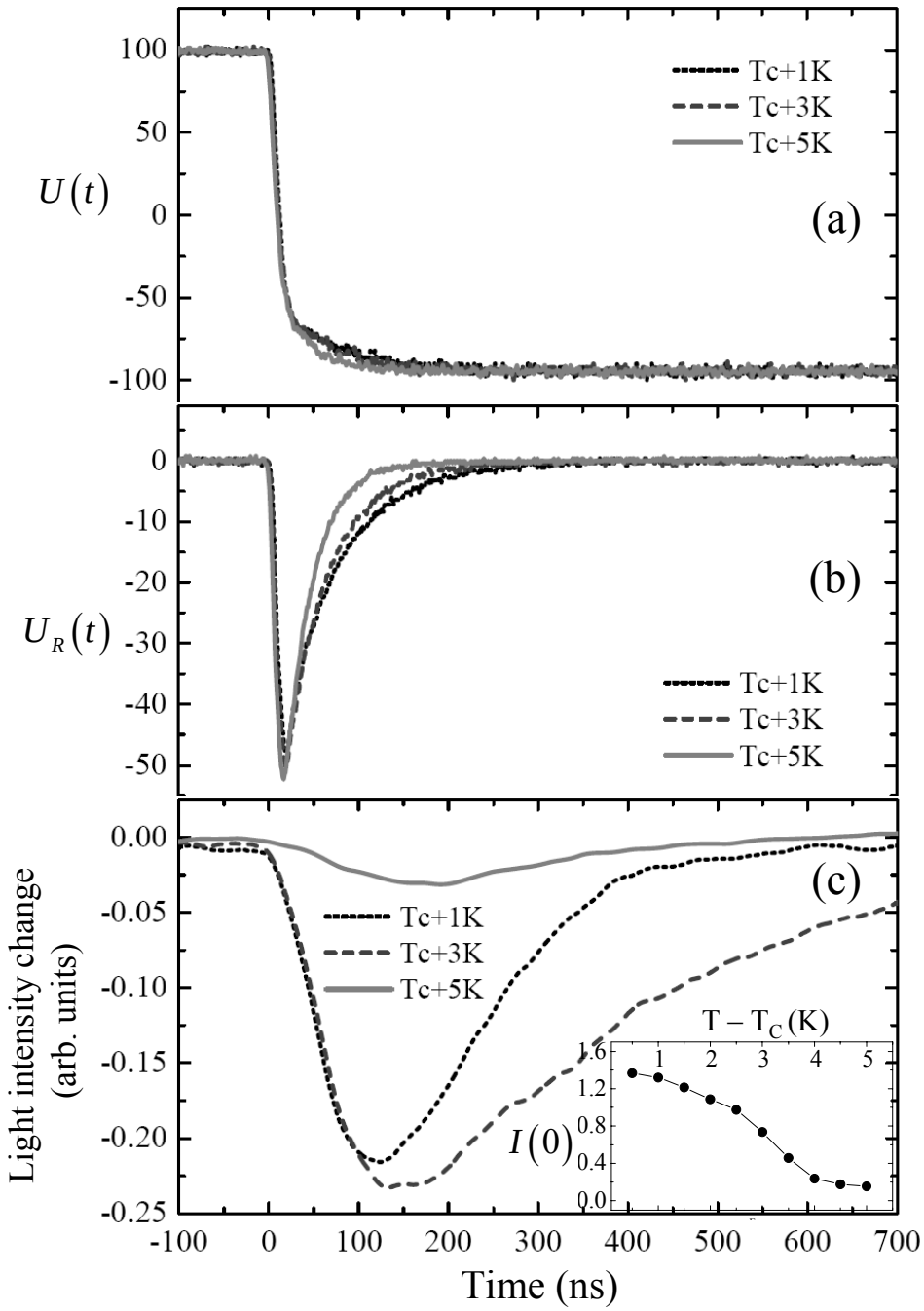

Figure 5.3. Experimental data of (a) total voltage $U(t)$, (b) voltage drop $U_R(t)$ on the resistor R, (c) transmitted light intensity change $I(t)-I(0)$ with respect to the stationary value $I(0)$ [inset of (c)] at different temperatures.

To determine $\varepsilon_{\parallel}^{l}(T,e_0)$ in the induced N phase, we use the experimental data on birefringence $\Delta n(T,e_0)$, as both quantities are related to the field-induced nonpolar order. Both $\Delta n(T,e_0)$ and $\varepsilon_{\parallel}^{l}(T,e_0)$ depend linearly on $S(T,e_0)$ [2] and are therefore linearly related, $\varepsilon_{\parallel}^{l}(T,e_0)=\varepsilon_{iso}^{l}+\eta\Delta n(T,e_0)$; here ε_{iso}^{l} is the low-frequency dielectric constant in the I phase, measured by us to be 16, and η is a fitting coefficient. We first measure $\varepsilon_{\parallel}^{l}(T,0)$ and $\Delta n(T,0)$ at zero field in the N phase and fit the measured data to obtain $\eta=64\pm3$, Figure 5.4. This value allows us to calculate $\varepsilon_{\parallel}^{l}(T,e_0)$ in the induced N phase from $\Delta n(T,e_0)$.

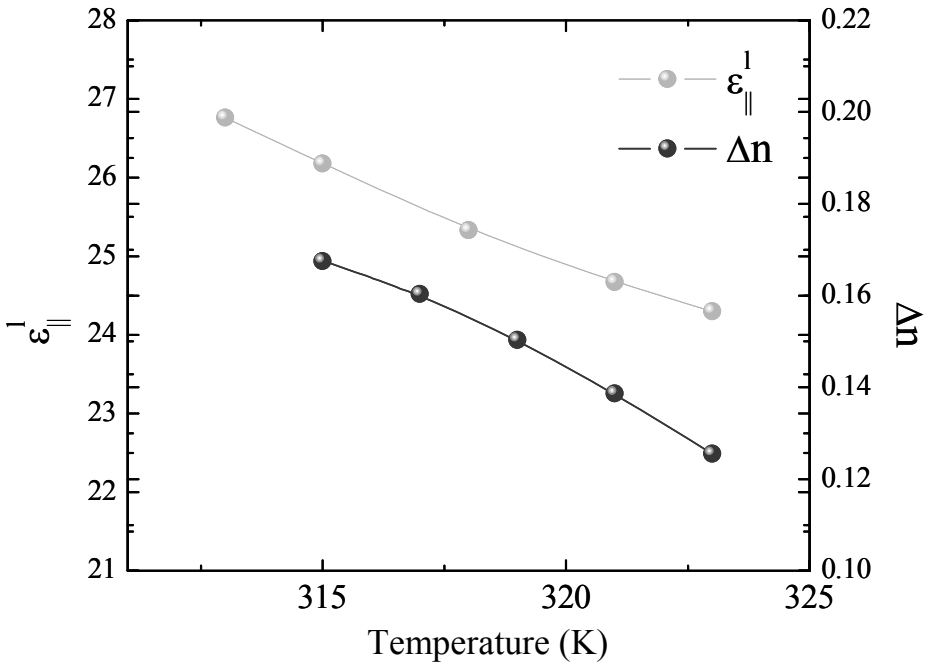

Figure 5.4. Temperature dependence of $\varepsilon_{\parallel}^{l}(T,0)$ and $\Delta n(T,0)$ in the nematic phase when there is no external electric field.

Both $\Delta n(T,e_0)$ and $S(t)=\bar{P}_2(t)$ are determined in the same birefringence experiment proposed by Lelidis *et al*. [5, 17, 57]. We measure the transmission of He-Ne laser beam through the cell of a known thickness and a pair of linear polarizers. We use oblique beam incidence and adjust the angle between the incident plane and the transmission axis of the polarizers to be 45.5^{o} instead of 45^{o}, to compensate the reflectivity difference for *s* and *p* polarizations, Figure 5.2. $\Delta n(T,e_0)$ was obtained from the stationary transmitted intensity while $\bar{P}_2(t)$ was determined from the dynamics of the optical signal in response to the polarity reversal, Figure 5.3(c).

Figure 5.5 shows the dynamics of the voltage $U_{LC}(t)$ acting on the LC layer (a), polar $\bar{P}_1(t)=vP(t)/\mu$ (b) and nonpolar $\bar{P}_2(t)$ (c) order parameters caused by the polarity reversal. The voltage change $U_{LC}(t)$ is determined by the rate of the generators voltage reversal and by the transient effects in the LC "capacitor" that involve the high-frequency dielectric constant $\varepsilon_{\|}^{h}$ and the dynamics of polarization $P(t)$. In our experiment, $U_{LC}(t)$ is fitted well with an exponential function,

$$U_{LC}(t)=U_0\left(2e^{-t/\tau_U}-1\right), \tag{5.9}$$

where the characteristic time τ_U is in the range of (60-30) ns, decreasing with temperature as shown in the inset in Figure 5.5(a). The polar order dynamics can also be fitted with the same functional dependence $\bar{P}_1(t)=\bar{P}_{10}\left(2e^{-t/\tau_P}-1\right)$, $\bar{P}_{10}=vP_0/\mu$, although the time constant τ_P is generally larger than τ_U, Figure 5.5(a) inset. One would observe $\tau_P=\tau_U$ if $\bar{P}_1(t)$ follows the changing electric field instantaneously;

this regime is approached only at high temperatures $T > T_C + 3\,\mathrm{K}$. At lower temperatures $T \le T_C + 3\,\mathrm{K}$, one clearly observes that $\tau_P > \tau_U$, reflecting the finite rate of dielectric relaxation. Note that the field reversal preserves the absolute value of the field induced polar order $\bar{P}_{10}$, as evidenced by our experiments for ten temperature points, see inset in Figure 5.5(b); this observation justifies our calculations based on Eq. (5.8).

With the approximations above, using the exponential fit of $U_{LC}(t)$, Eq. (5.9), we find the solution of Eq. (5.6) as

$$\bar{P}_1(t) = \bar{P}_{10}\left[\left(2e^{-t/\tau_U} - 1\right) + \frac{2}{\tau_U/\tau_{nem} - 1}\left(e^{-t/\tau_U} - e^{-t/\tau_{nem}}\right)\right]. \qquad (5.10)$$

The first term on the right hand side of Eq. (5.10) describes an instantaneous contribution to $\bar{P}_1(t)$ (see above), while the second term is related to the finite rate of dielectric relaxation with the characteristic time $\tau_{nem} = \tau / M_{11}$. The solution (5.10) with τ_{nem} in the range (10 – 30 ns) fits the experimental $\bar{P}_1(t)$ closely, somewhat better than the model based on an instantaneous dielectric response.

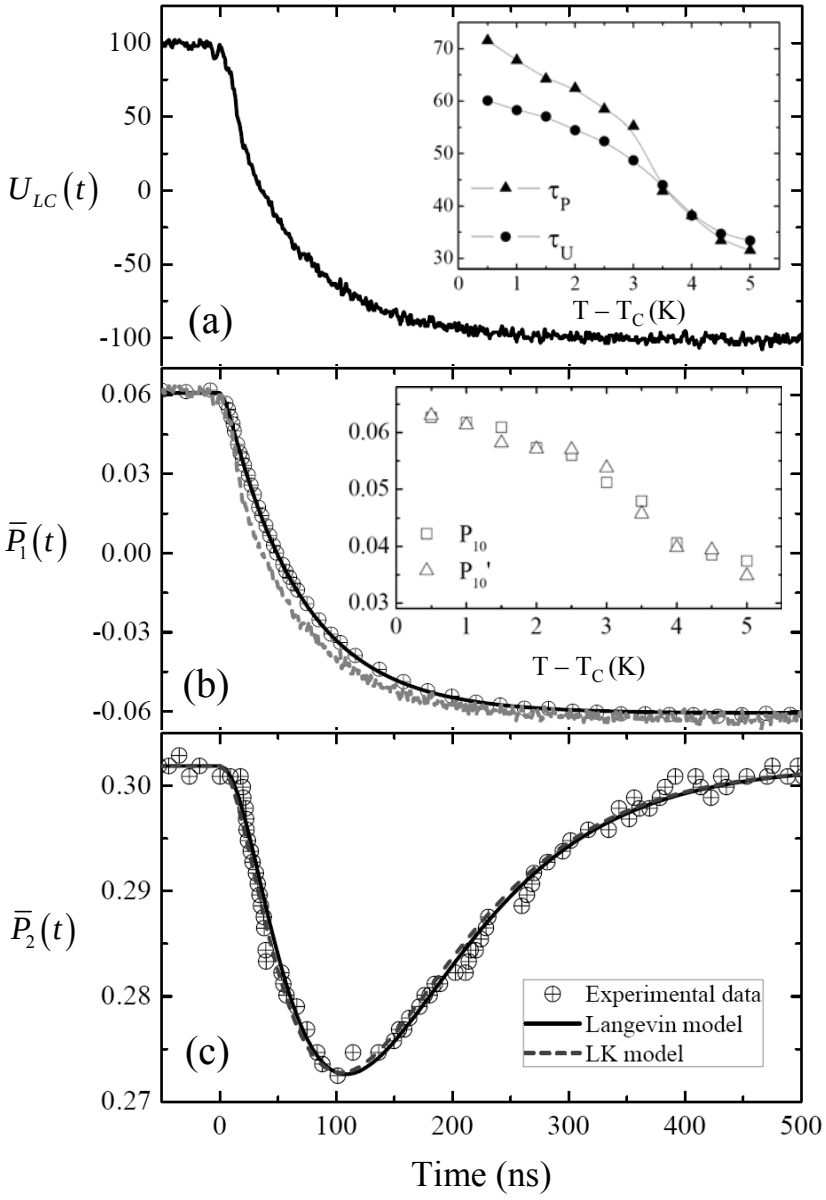

Figure 5.5. Dynamics of (b) $\bar{P}_1(t)$ and (c) $\bar{P}_2(t)$ under (a) voltage polarity reversal ($t=0$) at $T=T_C+1\,\mathrm{K}$. In (b) and (c), the circles are experimental data, the solid and dashed curves are simulations. The insets in (a) and (b) are: comparison between τ_U and τ_P, between $\bar{P}_1(t)$ values before ($\bar{P}_{10}$) and after ($\bar{P}_{10}'$) polarity reversal at different temperatures. The dashed curve in (b) is the instantaneous response of $\bar{P}_1(t)$ under the polarity reversal.

To analyze $\bar{P}_2(t)$, we linearize Eq. (5.7) with respect to $\Delta\bar{P}_2(t)=\bar{P}_2(t)-\bar{P}_{20}$ and $\left[e^2(t)-e_0^2\right]$ (note that the time interval during which $e^2(t)\neq e_0^2$ is rather short, ~150 ns), use solution (5.10) for $\bar{P}_1(t)$ and $e(t)=e_0\left(2e^{-t/\tau_U}-1\right)$, to arrive at the analytical solution for $\Delta\bar{P}_2(t)$:

$$\Delta\bar{P}_2(t)=\frac{h}{\tau_S}\exp\left(-\frac{t}{\tau_S}\right)\int_0^t H(t')\exp\left(\frac{t'}{\tau_S}\right)dt', \qquad (5.11)$$

where τ_S is the characteristic time for $\Delta\bar{P}_2(t)$ and h is the measure of the $\Delta\bar{P}_2(t)$ amplitude; the last term in $H(t)=\left(2e^{-t/\tau_U}-1\right)^2-1+2\left(e^{-t/\tau_U}-e^{-t/\tau_{nem}}\right)\left(2e^{-t/\tau_U}-1\right)\Big/\left(\tau_U/\tau_{nem}-1\right)$ represents the dielectric memory contribution. The integral (5.11) is analytical but the final expression is too cumbersome to be presented explicitly. Eq. (5.11) provides a good fit of the experimental data in Figure 5.5(c) with $\tau_S=95$ ns and $h=6.1\times10^5$ s^{-1}. The same experiment can be also fit with the LK model, neglecting the last term in Eq. (5.11), and using $\tau_S=95$ ns, $h=6.3\times10^5$ s^{-1}. In the LK approach, as seen by comparing Eq. (5.11) to Eq. (5.1)(1.33), $\tau_S=\gamma\Big/\left[\partial f/\partial S\right]_{e=e_0}$ and $h=\frac{\varepsilon_0\Delta\varepsilon_m}{3}\frac{\tau_s U_0^2}{\gamma d^2}$; note that in our experiment, the order parameters change within time interval that is much shorter than the characteristic time of thermal relaxation, so that $\partial f/\partial S$ should be evaluated for an adiabatic regime. The fact that both models fit the data well with the same $\tau_S=95$ ns can be explained by the fact that after $U_{LC}(t)$ and $\bar{P}_1(t)$ relaxed to

their new equilibrium values at $t \geq 250$ ns, $H(t)$ in Eq. (5.11) becomes close to zero and the corresponding integral approaches a constant value. In other words, $\Delta\bar{P}_2(t) \propto \exp(-t/\tau_S)$ at $t \geq 250$ ns. Since $\tau_S = \gamma \Big/ [\partial f / \partial S]_{e=e_0}$, this feature explains why the dynamics of $\bar{P}_2(t)$ observed at different temperatures is characterized by very different relaxation times, Figure 5.3(c).

5.3 Summary

We have determined experimentally and theoretically the dynamics of both the polar and the non-polar order parameters during the electric field-induced I-N phase transition. In materials with polar molecules, the electric field induces the nematic non-polar order indirectly, through its coupling to the polar order parameter. Note that in this work we consider the simplest possible geometry, with the molecular dipoles being parallel to the long axis of rod like molecules and thus parallel to the field induced director. In more complex geometries, for example, when the molecular dipoles are perpendicular to the long molecular axis, the coupling of polar and non-polar order parameters should lead to a much broader variety of the induced order, including a possible formation of biaxial phases and phases with a negative $S = \bar{P}_2(t)$.

Chapter 6

CONCLUSIONS

Director reorientation dynamics is essential to most of today's liquid crystal technologies. Advances in research have allowed one to reduce the response times from millisecond to microsecond and even to nanoseconds. For these small time scales, the description of the director dynamics requires a proper account of the dielectric dispersion effects. However, the first analysis of the role of dielectric dispersion in the director dynamics has been performed only very recently [4] [15]. Previous investigations were limited to dual frequency NLCs, and considered only a single dielectric relaxation process. In this thesis, we lift these limitations and propose a model that accounts for multiple processes of dielectric relaxations in both parallel and perpendicular dielectric permittivities. The model yields a number of counterintuitive predictions such as the polar contribution to the dielectric coupling between the field and the nematic liquid crystal. The most important results are summarized below:

First, we developed a general model to describe the director orientation dynamics of NLCs under an applied electric field that accounts for multiple dielectric

relaxations in both parallel and perpendicular dielectric permittivities. This model presents the contribution of dielectric relaxation as a "memory" effect; the director dynamics depends not only on the present electric and director fields, but also on their pre-histories. The model has been experimentally verified for three different types of NLCs. In dielectrically positive NLCs (positive dielectric anisotropy), this memory effect leads to a time delay of the desired director reorientation after the application of the electric field in the switch-on phase. In dielectrically negative NLCs, this memory effect leads to a larger dielectric torque, thus an acceleration of the director reorientation in the switch-on phase. In the case of dual frequency NLCs whose dielectric anisotropy changes sign as a function of the electric field frequency, the memory effect in the switch-on phase results in director rotation opposite to the desired orientation. Note that all three experimental situations can be described by the same approach developed in this work; the classic model of "instantaneous" response and the model with one dielectric relaxation cannot provide an accurate description of these experiments.

Second, we discovered an unusual contribution to the dielectric torque as a result of dielectric memory effect. This torque is linear in the present applied electric field and is thus sensitive to its polarity. The phenomenon is accompanied by a spectacular but counter-intuitive effect: the director relaxation during the "switch-off" stage can be accelerated if instead of an abrupt vertical back edge of the voltage pulse, we apply a pulse with a non-instantaneously vanishing back edge. The duration of the optimum edge is comparable to the time of NLCs' dielectric relaxation time and its

polarity depends on the polarity created in the nematic bulk by the voltage applied during the switch-on stage.

Third, we demonstrate the director dynamics under different "shapes" of the front edge of the voltage pulses, taking into account the dielectric relaxation. Our model allows us to optimize the front edge of the pulse to improve switching efficiency of DFNs. From the studies of Chapter 2, the director experiences an opposite rotation at the beginning of the switch-on stage when the DFNs are subject to a voltage with a sharply increasing front edge. This vertical front edge is perceived by the NLCs as a high frequency excitation that corresponds to the effectively negative dielectric anisotropy and thus to "wrong" direction of director reorientation.

Finally, we studied the dynamics of electrically induced isotropic-nematic (I-N) phase transition by accounting for the finite rate of the polarization dynamics, which has previously been considered an instantaneous process in the classic theory. Consequently the electrically induced nematic order parameter does not interact directly with the applied electric field, but is mediated by the dynamics of polarization. We present a model based on the Langevin equation that describes the dynamics of two crucial parameters: the polar and non-polar order parameters during the electrically induced I-N phase transition. This model can be reduced to the classic Landau-Khalatnikov theory, which considers the non-polar order parameter as an instantaneous function of the field and ignores the polar order dynamics if the characteristic polarization relaxation time is negligibly small. The proposed model is experimentally verified and compared with the classic model.

The accomplishments in this thesis bring a new understanding of the NLCs director dynamics, as well as the dynamics of the phase transition. From the view point of practical applications, these results are of particular interest for improving the switching speed, not only in the switch-on stage, but also fundamentally change the switch-off process from a passive to an active electrically driven process.

We close this thesis by laying out possible further problems to analyze in the area of director dynamics of NLCs subject to external fields:

(1). Explore the potential geometries for NLCs to utilize the polarity dependent dielectric torque to achieve fast switching, for example, NLCs stabilized in a polymer network.

(2). Extend the applicability of the optimization scheme from DFNs to conventional dielectrically dispersive NLCs whose dielectric anisotropy does not change sign as frequency changes.

REFERENCES

[1] P.G. de Gennes and J. Prost, *The Physics of Liquid Crystals* (Oxford University Press, New York, 1997).

[2] W.H. de Jeu, *Physical Properties of Liquid Crystalline Materials* (Gordon and Breach, New York, 1980).

[3] L.M. Blinov and V.G. Chigrinov, *Electrooptic Effects in Liquid Crystal Materials* (Springer-Verlag, New York, 1994).

[4] Y. Yin, S.V. Shiyanovskii, A.B. Golovin, and O.D. Lavrentovich, Phys. Rev. Lett. **95**, 087801 (2005).

[5] M. Gu, Y. Yin, S.V. Shiyanovskii, and O.D. Lavrentovich, Phys. Rev. E **76**, 061702 (2007).

[6] M. Gu, S. V. Shiyanovskii, and O. D. Lavrentovich, Phys. Rev. Lett. **100**, 237801 (2008).

[7] M. Gu, S. V. Shiyanovskii, and O. D. Lavrentovich, Phys. Rev. E **78**, 040702(R) (2008).

[8] F. C. Frank, Discuss Faraday **25**, 19 (1958).

[9] J.L. Ericksen, Trans. Soc. Rheol. **5**, 23 (1961).

[10] F.M. Leslie, Arch. Ration. Mech. Anal. **28**, 265 (1968).

[11] M. Kleman and O.D. Lavrentovich, *Soft Matter Physics: An Introduction* (Springer-Verlag, New York, 2003).

[12] J. D. Jackson, *Classical Electrodynamics* (Wiley, New York, 1962).

[13] W. Haase and S. Wróbel, *Relaxation Phenomena: Liquid Crystals, Magnetic Systems, Polymers, High-Tc Superconductors, Metallic Glasses* (Springer, New York, 2003).

[14] P. Debye, *Polar Molecules* (Dover, New York, 1929).

[15] N.J. Mottram and C.V. Brown, Phys. Rev. E **74**, 031703 (2006).

[16] P.G. de Gennes, Mol. Cryst. Liq. Cryst. **12**, 193 (1971).

[17] I. Lelidis and G. Durand, Phys. Rev. E **48**, 3822 (1993).

[18] I. Lelidis and G. Durand, Phys. Rev. Lett. **73**, 672 (1994).

[19] I. Lelidis and G. Durand, Phys. Rev. Lett. **76**, 1868 (1996).

[20] S.T. Wu and D.-K. Yang, *Fundamentals of Liquid Crystal Devices* (John Wiley, New York, 2006).

[21] D.-K. Yang and S.T. Wu, *Fundamentals of Liquid Crystal Devices* (John Wiley, New York, 2006).

[22] H. Takanashi, J.E. Maclennan, and N.A. Clark, Jpn. J. Appl. Phys., Part 1 **37**, 2587 (1998).

[23] A.B. Golovin, S.V. Shiyanovskii, and O.D. Lavrentovich, Appl. Phys. Lett. **83**, 3864 (2003).

[24] B.A. Belyaev, N.A. Drokin, V.F. Shabanov, and V.A. Baranova, Phys. Solid State **46**, 554 (2004).

[25] H. –G. Kreul, S. Urban, and A. Würflinger, Phys. Rev. A **45**, 8624 (1992).

[26] B.O. Gestblom and S. Wróbel, Liq. Cryst. **18**, 31 (1995).

[27] T.K. Bose, B. Campbell, S. Yagihara, and J. Thoen, Phys. Rev. A **36**, 5767 (1987).

[28] J.L. Erickson, Trans. Soc. Rheol. **5**, 23 (1961).

[29] F.M. Lesile, Arch. Ration. Mech. Anal. **28**, 265 (1968).

[30] D.W. Berreman, J. Appl. Phys. **46**, 3746 (1975).

[31] N.J. Smith, M.D. Tillin and J.R. Sambles, Phys. Rev. Lett. **88**, 088301 (2002).

[32] Y. Yin, M. Gu, A.B. Golovin, S.V. Shiyanovskii, and O.D. Lavrentovich, Mol. Cryst. Liq. Cryst. **421**, 133 (2004).

[33] B.A. Belyaev, N.A. Drokin, V.F. Shabanov, V.N. Shepov, Mol. Cryst. Liq. Cryst. **366**, 305 (2001).

[34] P.G. Cummins, D.A. Dunmur, and D.A. Laidler, Mol. Cryst. Liq. Cryst. **30**, 109 (1975).

[35] B.R. Ratna and R. Shashidhar, Mol. Cryst. Liq. Cryst. **42**, 185 (1977).

[36] S.A. Rozanski, R. Stannarius, H. Groothues, and F. Kremer, Liq. Cryst. **20**, 59 (1996).

[37] S.A. Rozanski, G.P. Sinha, and J. Thoen, Liq. Cryst. **33**, 833 (2006).

[38] Yu. A. Nastishin, R.D. Polak, S.V. Shiyanovskii, V.H. Bodnar and O.D. Lavrentovich, J. Appl. Phys. **86**, 4199 (1999).

[39] Z. Zou, H. Takanashi, G.M. Danner, J. MacLennan, and N.A. Clark, Bull. APS **41**, A17.01 (1996).

[40] S.T. Wu and C.S. Wu, Phys. Rev. A **42**, 2219 (1990).

[41] M. Gu, Y. Yin, S.V. Shiyanovskii and O.D. Lavrentovich, In preparation (2007).

[42] J.K. Song, K.E. Lee, H.S. Chang, S.M. Hong, M.B. Jun, B.Y. Park, S.S. Seomun, K.H. Kim, and S.S. Kim, SID Int. Symp. Digest Tech. Papers **48**, 1344 (2004).

[43] M. Gu, I.I. Smalykuh, and O.D. Lavrentovich, Appl. Phys. Lett. **88**, 061110 (2006).

[44] Y. Yin, S.V. Shiyanovskii, and O.D. Lavrentovich, J. Appl. Phys. **100**, 024906 (2006).

[45] A. Rapini, J. Phys. (Paris) **34**, 629 (1973).

[46] I.I. Smalyukh, S.V. Shiyanovskii, and O.D. Lavrentovich, Chem. Phys. Lett. **336**, 88 (2001).

[47] O.P. Pishnyak, S. Tang, J.R. Kelly, S.V. Shiyanovskii, and O.D. Lavrentovich, Phys. Rev. Lett. **99**, 127802 (2007).

[48] M. Oh-e and K. Kondo, Appl. Phys. Lett. **67**, 3895 (1995).

[49] G. Basappa and N.V. Madhusudana, Eur. Phys. J. B **1**, 179 (1998).

[50] W. Maier and A. Saupe, Z. Naturforsch. A **13**, 564 (1958).

[51] W. Maier and A. Saupe, Z. Naturforsch. A **14**, 882 (1959).

[52] W.T. Coffey, Yu.P. Kalmykov and J.T. Waldron, *The Langevin Equation, 2nd Ed.* (World Scientific, Singapore, 2004).

[53] R.N. Thurston, J. Appl. Phys. **55**, 3846 (1984).

[54] G. W. Gray and S. M. Kelly, J. Mater. Chem. **9**, 2037 (1999).

[55] I. Dozov and Ph. Martinot-Lagarde, Phys. Rev. E **58**, 7442 (1998).

[56] Ph. Martinot-Lagarde, J. Phys. (France) Lett. **38**, L-17 (1977).

[57] I. Lelidis, M. Nobili, and G. Durand, Phys. Rev. E **48**, 3818 (1993).